UNIVERSITY OF CALIFORNIA, SAN DIEGO

Detection of degree-scale B-mode polarization and studying cosmic polarization rotation with the BICEP1 and BICEP2 telescopes

A dissertation submitted in partial satisfaction of the
requirements for the degree
Doctor of Philosophy

in

Physics

by

Jonathan Philip Kaufman

Committee in charge:

Professor Brian Keating, Chair
Professor Kim Griest
Professor Hans Paar
Professor Gabriel Rebeiz
Professor Mark Thiemens

2014

The dissertation of Jonathan Philip Kaufman is approved, and it is acceptable in quality and form for publication on microfilm and electronically:

_____

_____

_____

_____

_____
Chair

University of California, San Diego

2014

DEDICATION

To my niece, Lauren Lee, the culmination of 13.8 billion years of cosmic evolution.

EPIGRAPH

$$G_{\mu\nu} + \Lambda g_{\mu\nu} = \frac{8\pi G}{c^4} T_{\mu\nu}$$

—Albert Einstein

TABLE OF CONTENTS

Signature Page iii

Dedication iv

Epigraph v

Table of Contents vi

List of Figures x

List of Tables xiii

Acknowledgements xiv

Vita xvi

Abstract of the Dissertation xvii

Chapter 1 Introduction 1
1.1 A brief history of the Universe 1
1.2 The Cosmic Microwave Background 2
1.3 Anisotropies 2
1.4 Polarization 4
1.5 Problems with the Big Bang model 6
1.5.1 Horizon problem 6
1.5.2 Flatness problem 6
1.5.3 Magnetic monopole problem 7
1.6 Cosmic Inflation 7

Chapter 2 Studying the CMB 9
2.1 From maps to power spectra 9
2.2 Correlations 11
2.2.1 Large-scales 11
2.2.2 Small-scales 12
2.2.3 Cosmological parameters 12
2.3 Polarization power spectra 13
2.3.1 E-modes 15
2.3.2 B-modes 16
2.3.3 Cross-correlations 17
2.4 Tensor-to-scalar ratio 18
2.5 The hunt for r 18

Chapter 3 Polarization Rotation . . . 21
3.1 Astrophysical probes of Cosmic Polarization Rotation . . 21
3.2 Polarization Rotation from the CMB . . . 22
3.3 Birefringence . . . 26

Chapter 4 The BICEP1 and BICEP2 telescopes . . . 30
4.1 Observations, strategy, and design . . . 31
4.1.1 South Pole observatory . . . 31
4.1.2 Telescope mount . . . 34
4.1.3 Scan strategy . . . 35
4.1.4 Ground shield and baffling . . . 36
4.1.5 Optics . . . 37
4.1.6 Control software . . . 38
4.2 Primary differences . . . 38
4.2.1 Cryogenic cooling system . . . 39
4.2.2 Sub-Kelvin design and thermal control . . . 40
4.2.3 Detectors and readout . . . 42
4.2.4 Analysis techniques . . . 46

Chapter 5 Thermal Stability of BICEP2 . . . 51
5.1 Motivation . . . 51
5.1.1 Detectors . . . 51
5.1.2 Telescope scan . . . 52
5.2 Thermal design . . . 52
5.3 Thermal stability . . . 54
5.3.1 Passive thermal control . . . 55
5.3.2 Active thermal control . . . 56
5.3.3 Thermal stability benchmark . . . 58
5.3.4 Achieved Thermal Stability . . . 58

Chapter 6 Self-Calibration of BICEP1 Three-Year Data and Constraints on Astrophysical Polarization Rotation . . . 62
6.1 Introduction . . . 63
6.2 Polarization Rotation of the CMB Power Spectra . . . 65
6.3 Data and Analysis Methodology . . . 66
6.3.1 Data Sets . . . 68
6.3.2 Likelihood Analysis . . . 68
6.4 Rotation Angle Results . . . 71
6.4.1 Consistency Between Analysis Methods . . . 71
6.4.2 Consistency Between Frequencies . . . 73
6.4.3 Consistency with Planck Temperature Maps . . . 76
6.5 Impact of Instrumental Systematic Effects . . . 76
6.5.1 Polarization Angle Calibration . . . 76

6.5.2 Differential Beam Effects . . . 79
6.5.3 Experimental Consistency Checks . . . 81
6.6 Constraints on Frequency Dependent Cosmological Birefringence . . . 83
6.6.1 Contaldi Dowker Philpott Model . . . 84
6.6.2 Faraday Rotation of Galactic Magnetic Field . . . 85
6.7 Self-Calibrated Upper Limit on Tensor to Scalar Ratio . 85
6.8 Conclusion . . . 86

Chapter 7 Detection of degree-scale B-mode polarization with BICEP2 . 88
7.1 Data set . . . 89
7.2 Maps . . . 93
7.3 Power spectra . . . 95
7.4 Consistency tests . . . 98
7.5 Instrumental contamination . . . 101
7.5.1 Beam sources . . . 103
7.5.2 Other sources . . . 105
7.6 Foreground contamination . . . 106
7.6.1 Polarized point sources . . . 107
7.6.2 Synchrotron radiation . . . 107
7.6.3 Polarized dust . . . 107
7.7 Comparison with BICEP1 and Keck array . . . 109
7.8 Cosmological interpretation . . . 110

Chapter 8 Path forward . . . 113
8.1 B-modes . . . 113
8.2 Cosmic polarization rotation . . . 115

Appendix A Spectral bandpass of the BICEP2 telescope . . . 118
A.1 What is an FTS? . . . 118
A.2 Measurements at Pole . . . 119
A.3 The pipeline . . . 120
A.3.1 Getting an interferogram . . . 122
A.3.2 Filtering . . . 122
A.3.3 Centering around WLF . . . 123
A.3.4 Windowing the data . . . 123
A.3.5 Getting the spectra . . . 123
A.3.6 Correcting for the spectrum of the source . . . 123
A.3.7 Shifting the frequency axis . . . 125
A.4 Results . . . 125
A.4.1 Band center . . . 125
A.4.2 Bandwidth . . . 126
A.5 Spectral gain mismatch . . . 126

Appendix B Algorithm for determining snowfall on the BICEP2 window . . 129
B.1 Cosmology at the South Pole 129
B.2 Snow in July? 130
B.3 Classifying LFB IR camera images 130
B.3.1 Algorithm 131
B.3.2 Limitations 132
B.4 HTML browser 133
B.5 Intersection with machine learning 134

Bibliography 139

LIST OF FIGURES

Figure 1.1: The blackbody spectrum of the CMB. 3
Figure 1.2: Full sky map of the CMB temperature anisotropy. 4
Figure 1.3: E- and B-mode patterns. 5

Figure 2.1: CMB temperature anisotropy power spectrum. 12
Figure 2.2: Plots of the Stokes parameters. 14
Figure 2.3: Measured E-mode and B-mode power spectra. 16
Figure 2.4: The search for B-modes. 19

Figure 3.1: TB and EB correlations due to polarization rotation. 24
Figure 3.2: Image of the Crab Nebula in multiple wavelengths. 25
Figure 3.3: Taurus A polarization intensity map with polarization vectors at 90 GHz. 26

Figure 4.1: CMB observing patch for BICEP1 and BICEP2. 32
Figure 4.2: Dark sector laboratory (DSL) at the South Pole. 33
Figure 4.3: The BICEP mount. 34
Figure 4.4: Optical and microwave spectrum photos of a microwave source above the MAPO building. 37
Figure 4.5: Optical design of BICEP2. 39
Figure 4.6: Schematic of the IC and UC stages. 41
Figure 4.7: The BICEP1 and BICEP2 focal planes. 43
Figure 4.8: BICEP1 polarization sensitive bolometer (PSB). 44
Figure 4.9: A sample BICEP2 antenna array and transition edge sensor (TES) bolometer. 45
Figure 4.10: Residual beam-shapes of differenced gaussian beams for each of the BICEP2 six-parameter differential beam mismatches. 48

Figure 5.1: Schematic model of the thermal architecture of BICEP2. 54
Figure 5.2: Thermal architecture of the Ultra-Cooled stage. 55
Figure 5.3: PSDs of timestreams of NTDs on clean and dirty sides of the thermal filter to square wave at 5 mHz. 56
Figure 5.4: Passive Thermal Filter transfer function. 57
Figure 5.5: Angular power spectrum of second season coadded map of NTD thermometer on one of the four detector tiles for each of the four boresite angles observed. 59
Figure 5.6: Temperature maps for thermal fluctuations coadded over the second season of observation. 61

Figure 6.1: TB and EB power spectra after applying polarization rotation of -3° (blue) to +3° (red), in 0.5° steps. 67

Figure 6.2: TB and EB power spectra for all frequency combinations from BICEP1. 69
Figure 6.3: A two-color plot showing the elements of the bandpower covariance matrix used in the all-spectra HL likelihood calculation. . 72
Figure 6.4: The peak-normalized Hamimeche-Lewis likelihood for the all-spectra "TEB" rotation angle. 73
Figure 6.5: Frequency-combined three-year BICEP1 spectra shown with the theoretical rotated spectra from the best fit all-spectra rotation angle. 74
Figure 6.6: Comparison of the two likelihood methods employed for the rotation angle calculation for the frequency combined data. . . 75
Figure 6.7: Comparison of integral-normalized Hamimeche-Lewis method likelihoods of all-spectra (TEB) rotation angles for all BICEP1 data sets. 75
Figure 6.8: A plot of the effects of differential ellipticity and differential pointing on the TB and EB power spectra 82
Figure 6.9: A histogram of the probability to exceed values for the measurement of $\Delta\alpha$ in each of the jackknife spectra. 83
Figure 6.10: Best fit μ and χ values for the CDP model for 100 GHz and 150 GHz from the all-spectra estimator, along with their 68% confidence interval contours. 85

Figure 7.1: The Dark Sector Laboratory (DSL). 89
Figure 7.2: Live time of BICEP2 and the fraction of data used for the final analysis. 90
Figure 7.3: Three-year temperature and Stokes Q and U maps with their temporal jackknife maps. 96
Figure 7.4: E and B maps from three-years of BICEP2 data compared to simulation. 97
Figure 7.5: TT, TE, EE, BB, TB, and EB power spectra plots. 98
Figure 7.6: Histograms of PTE values for the χ^2 and χ metrics for all fourteen jackknife tests. 103
Figure 7.7: Expected contamination to the B-mode power spectrum from instrumental contamination. 106
Figure 7.8: Predicted level of B-mode contamination due to galactic dust from several models. 108
Figure 7.9: BICEP2 E-mode and B-mode auto-spectra plotted with cross-spectra between BICEP2 and BICEP1 100 GHz, and between BICEP2 and BICEP1 150 GHz. 110
Figure 7.10: BICEP2 auto-spectra plotted with cross spectra between BICEP2 and the frequency-combined BICEP1 data, and between BICEP2 and the Keck array (at 150 GHz). 111

Figure 7.11: BICEP2 BB bandpowers with the best-fit lensed-ΛCDM + r = 0.2 and the respective Likelihood curve for r. 111

Figure 8.1: The search for B-mode polarization. 114
Figure 8.2: Derived rotation angles from galaxy sources from Table 3.1 and the CMB from Table 3.2 with the BICEP1 and BICEP2 results. . 116
Figure 8.3: Light reflects and refracts off of ice crystals in the upper atmosphere to create a 22° halo, sun dogs (bright spots), upper tangent arc, and a parhelic circle. 117

Figure A.1: The FTS used at Pole for BICEP2 calibrations. 119
Figure A.2: The FTS coupled directly to the BICEP2 cryostat prior to decommissioning at the South Pole in December 2012. 121
Figure A.3: Comparison plot of the Radiance for a Blackbody using Planck's Law and for the Rayleigh-Jeans Law. 124
Figure A.4: Array-averaged bandpass for RGL detectors plotted with the atmospheric transmission and the CMB anisotropy. 126
Figure A.5: Calculated band centers for the BICEP2 focal plane. 127

Figure B.1: Picture of the membrane which covers the BICEP2 window. . . 131
Figure B.2: Lower Forebaffle (LFB) IR camera picture showing no snow contamination. 133
Figure B.3: Lower Forebaffle (LFB) IR camera pictures showing a light dusting of snow and larger clumps of snow. 136
Figure B.4: Lower Forebaffle (LFB) IR camera pictures demonstrating the limitations of the snow finding algorithm. 137
Figure B.5: A sample algorithm HTML display page. 138

LIST OF TABLES

Table 3.1: Polarization rotation angles derived from radio-wave and ultraviolet observations of galaxies. 22
Table 3.2: Polarization rotation angles derived from the CMB. 23

Table 5.1: Thermal conductances along the cooling path. 53

Table 6.1: Previous rotation angle constraints from CMB experiments. . . . 64
Table 6.2: Maximum likelihood value and 1σ error for α. 73
Table 6.3: Polarization rotation angles derived using different detector polarization angle calibrations. 79
Table 6.4: Maximum likelihood values for the damping parameter, μ, and the rotation angle, χ, along with their 1σ error bars for the CDP model. 84

Table 7.1: BICEP2 data cuts. 91
Table 7.2: PTE values from the χ^2 and χ metrics for all fourteen jackknife tests. 102
Table 7.3: Measured differential beam parameters. 105

ACKNOWLEDGEMENTS

There are so many people who made this dissertation possible. First, I want to acknowledge the entire BICEP team. It has been an honor to work with such incredible scientists. I especially want to thank my fellow graduate students: Justus, Randol, Chris, Sarah, Grant, Jamie, Chin Lin, and Kirit.

I want to acknowledge all the graduate students in my cohort at UCSD, especially Casey, Joe, and Carrie, for all the "war stories" we've traded over hot food and cold beer.

To my amazing fellow graduate students: Evan, Nate, Stephanie, Dave, Chang, Darcy, Fred, Praween, Marty, and Tucker; the wonderful postdocs and undergrads: Meir, Angiola, Nate, Amit, Brandon, Matt, Priscilla, Chris, James, Daniel, Luis, Kenneth, Jen, Steve, Jason, Lisa, and Minyoung; and, of course, the brilliant Hans and Kam: it has been so wonderful to work alongside you all.

Of course, I owe this dissertation to Brian Keating. Brian, you've been a wonderful advisor, a cherished friend, and you are a member of the family, as far as I'm concerned. I could not have done this without your unwavering support and belief that I could accomplish anything. I am thrilled that we get to continue to work together this coming year and hopefully beyond!

Finally, and most importantly, I want to thank my family for their love and support. My parents, Renée and Bob; my sister Liana and brother-in-law Matt, and my wonderful niece, Lauren Lee; and, of course, my amazing Lauren who kept me sane, fed, and snuggled throughout this whole process. To properly thank you would fill the entirety of this dissertation so to put it succinctly, I love you very much. You all mean the world to me.

I wish I could show this to my grandma Rose and grandpa Al to show them just how inspired I was by all those trips to the Baltimore Science Center and the National Air and Space Museum!

Chapter 6, in part, is a reprint of material as it appears in Physical Review D 89, 062006, 2014. J. P. Kaufman, N. J. Miller, M. Shimon, D. Barkats, C. Bischoff, I. Buder, B. G. Keating, J. M. Kovac, P. A. R. Ade, R. Aikin, J. O. Battle, E. M. Bierman, J. J. Bock, H. C. Chiang, C. D. Dowell, L. Duband, J. Filippini, E. F. Hivon, W. L. Holzapfel, V. V. Hristov, W. C. Jones, S. S. Kernasovskiy, C. L. Kuo, E. M. Leitch, P. V. Mason, T. Matsumura, H. T. Nguyen, N. Ponthieu, C. Pryke, S. Richter, G. Rocha, C. Sheehy, M. Su, Y. D. Takahashi, J. E. Tolan, and K. W. Yoon. American Physical Society, 2014.

VITA

2007	B. S. in Physics with a concentration in Astrophysics, Carnegie Mellon University
2007 - 2008	Graduate Teaching Assistant, University of California, San Diego
2009	M. S. in Physics, University of California, San Diego
2009 - 2014	Graduate Student Researcher, University of California, San Diego
2011	C. Phil. in Physics, University of California, San Diego
2014	Ph. D. in Physics, University of California, San Diego

PUBLICATIONS

BICEP2 Collaboration, "BICEP2 I: Detection Of B-mode Polarization at Degree Angular Scales," 2014

BICEP2 Collaboration, "BICEP2 II: Experiment and Three-Year Data Set," 2014

Kaufman et al., "Self-Calibration of BICEP1 Three-Year Data and Constraints on Astrophysical Polarization Rotation," 2013

BICEP1 Collaboration, "Degree-Scale CMB Polarization Measurements from Three Years of BICEP1 Data," 2013

Moyerman et al., "Scientific Verification of Faraday Rotation Modulators: Detection of Diffuse Polarized Galactic Emission," 2013

Bierman et al., "A Millimeter-Wave Galactic Plane Survey with the BICEP Polarimeter," 2011

Ogburn et al., "BICEP2 and Keck Array Operational Overview and Status of Observations," 2010

Sheehy et al., "The Keck Array: A Pulse Tube Cooled CMB Polarimeter," 2010

Brevik et al., "Initial Performance of the BICEP2 Antenna-Coupled Superconducting Bolometers at the South Pole," 2010

Aiken et al., "Optical Performance of the BICEP2 Telescope at the South Pole," 2010

Nguyen et al., "BICEP2/SPUD: Searching for Inflation with Degree Scale Polarimetry from the South Pole," 2008

ABSTRACT OF THE DISSERTATION

Detection of degree-scale B-mode polarization and studying cosmic polarization rotation with the BICEP1 and BICEP2 telescopes

by

Jonathan Philip Kaufman

Doctor of Philosophy in Physics

University of California, San Diego, 2014

Professor Brian Keating, Chair

The BICEP1 and BICEP2 telescopes studied the temperature and polarization of the Cosmic Microwave Background (CMB) from 2006 - 2008 and 2010 - 2012, respectively, producing the deepest maps of polarization created to date. From BICEP2 three-year data, we detect B-mode polarization at the degree-scale above the expectation from lensed-ΛCDM to greater than 5σ significance, consistent with that expected from gravitational waves created during Inflation. Instrumental systematic effects have been characterized and ruled out, and galactic foreground contamination is disfavored by the data.

Additionally, correlations between temperature and B-mode polarization and between E-mode and B-mode polarization show evidence of polarization ro-

tation of -1° to 5σ significance; however, adding systematic uncertainty reduces this significance to $\sim 2\sigma$. These measurements, combined with other CMB and astrophysical measurements, point to possible parity violating physics like cosmic birefringence, but more precise calibration techniques are required to break the degeneracy between cosmic polarization rotation and systematic effects. Improved calibration is possible with current generation technology and may be achieved within the next few years.

In this work, I present experimental and analysis techniques employed for BICEP1 and BICEP2 to measure B-mode polarization and temperature and polarization correlations, as well as the scientific motivation, results, and a path forward for future measurements.

Chapter 1

Introduction

There is a theory which states that if ever anyone discovers exactly what the Universe is for and why it is here, it will instantly disappear and be replaced by something even more bizarre and inexplicable.

Douglas Adams
The Restaurant at the End of the Universe

1.1 A brief history of the Universe

In the mid 1920s, Edwin Hubble made an astounding discovery. As he observed distant galaxies, he noticed that they all seemed to be receding from us, and their recession velocity was correlated with their distance. Our Universe, it appeared, was expanding. Georges Lemaître ran the clock backwards and posited that there must have been a time far in the past when all the matter in the Universe would have been co-located – there must have been a beginning. In the 1930s and 40s, George Gamow, Ralph Alpher, and Robert Herman worked out the nuclear reactions which would have occurred in an early hot dense Universe, like the one theorized by Lemaître. This is known as Big Bang Nucleosynthesis (BBN). A core prediction of BBN was that a background radiation should be detectable throughout the Universe.

1.2 The Cosmic Microwave Background

Gazing up at the night's sky with microwave vision would reveal a radiant glow. This faint glow comes from the oldest light in the Universe, the cosmic microwave background (CMB). The CMB is the remnant of the Big Bang, the beginning of our expanding Universe. Energetic photons created from annihilations of matter and anti-matter in the very early Universe scattered off of free particles, immediately ionizing any neutral atoms. As time progressed, the Universe expanded and cooled. Eventually, 380,000 years after the Big Bang, the Universe became cool enough for matter to form without being immediately ionized. This epoch is known as "recombination." At the end of recombination, photons which were once tightly coupled to the baryons were scattered for the last time and free-streamed throughout the Universe. This is known as the "surface of last scattering." As these scattered photons streamed through our 13.8 billion year old expanding Universe, they redshifted so that we now observe them in the microwave spectrum. This microwave radiation is the CMB.

At this transition, where the photons were no longer tightly-coupled to the baryons, the Universe became transparent. Since the Universe was dominated by hot photons until this point, we cannot observe epochs before the CMB, 380,000 years after the Big Bang, using conventional methods. However, we can infer what happened before this time by studying the temperature and polarization of the CMB photons across the sky.

The CMB is the smoothest blackbody in existence. It adheres to a blackbody spectrum with a peak at 2.73 K (as shown in Figure 1.1) with deviations at a few parts per 10,000. Studying these deviations tells us a significant amount about our early Universe, from its age and curvature, to large scale structure formation like galaxy clusters.

1.3 Anisotropies

If we subtract 2.73 K from the CMB, we are left with a dipole pattern due to our relative motion with respect to the CMB. Subtracting this dipole, we see

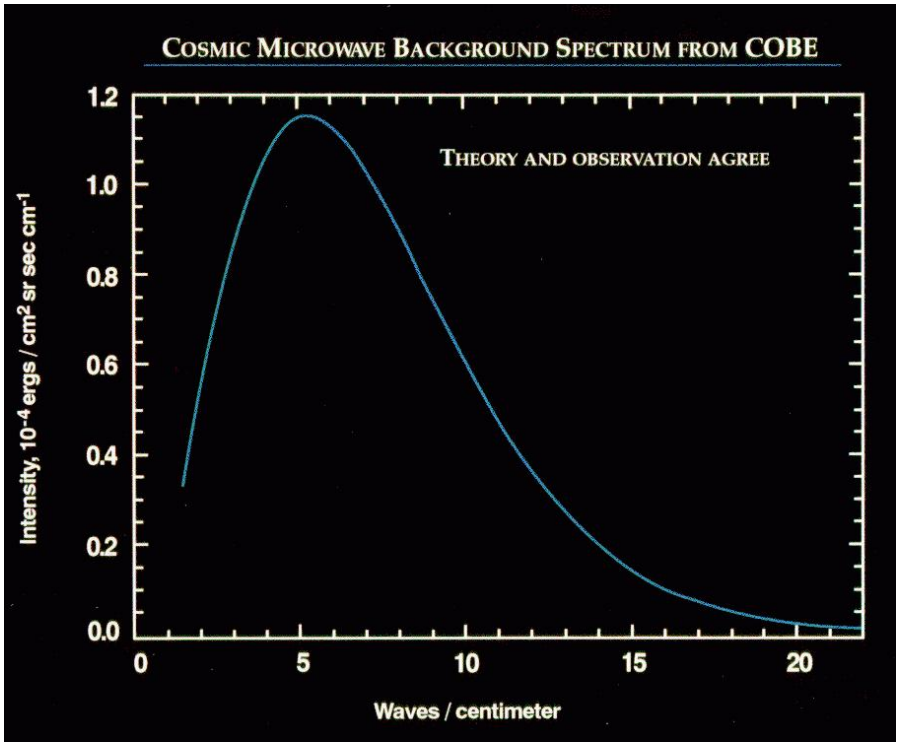

Figure 1.1: The spectrum of the CMB compared to a blackbody, as measured by the FIRAS instrument on the COBE satellite[1]. The CMB is described by a blackbody so well that the data points are indistinguishable from the theory curve.

that the CMB is a rough surface with fluctuations between $\pm 100\mu$K, as shown in Figure 1.2. These anisotropies in the temperature are due to inhomogeneities in the gravitational potential at the time of recombination. A photon scattered from a deeper potential well (i.e. more density) has to climb out, causing it to redshift leading to a "cold spot." These dense cold spots will eventually cause matter to gravitationally collapse, increasing its gravitational potential which then traps more matter. This process continues until you get stars, galaxies, clusters, and eventually the large-scale structure we observe today.

The mechanisms behind these anisotropies are quantum in nature but the discussion of these will have to wait until I introduce Inflation.

[1] http://lambda.gsfc.nasa.gov/product/cobe/firas_image.cfm

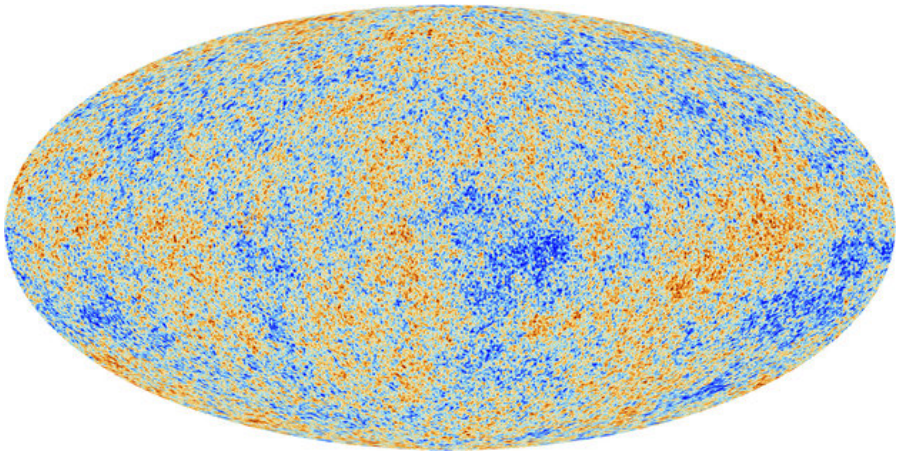

Figure 1.2: A full-sky map of the CMB anisotropy from the Planck satellite [59]. The scale is from -150 to +150 μK.

1.4 Polarization

In addition to the temperature, around $1 \sim 3\%$ of the CMB anisotropy is polarized, giving us another dimension to study the early Universe. This polarization is expected due to Thomson scattering of CMB photons off of free electrons at the surface of last scattering. For a CMB photon to pick up a net polarization, the scattered photons must have come from a quadrupole anisotropy. Isotropic radiation will not pick up a net polarization since the radiation scattering has equal intensity in each direction seen by the electron. Similar to dipole radiation, the incoming radiation will scatter with an averaged intensity thus there will be no net polarization scattered. We require a quadrupole anisotropy in radiation intensity for the scattered photons to pick up a net polarization.

The natural question is what creates these quadrupole anisotropies? Density fluctuations in the plasma would create a quadrupole anisotropy. In addition to this, currents in the plasma would create a vorticity contribution to the quadrupole. These vorticity anisotropies are expected to be negligible. Finally, and arguably most interestingly, gravitational waves create a quadrupole pattern. These quadrupole anisotropies are known as Scalar, Vector, and Tensor perturbations, respectively, for these density, vorticity, and gravitational wave perturbations.

To study the polarization of the CMB, we decompose the polarization pattern into E-modes and B-modes, where E-modes are curl-free, gradient-like patterns and B-modes are curl-like patterns. This naturally breaks the polarization into parity even (E-mode) and parity odd (B-mode) patterns. This decomposition is crucial as E-modes and B-modes are created from different processes. At the surface of last scattering, E-modes are caused by scalar perturbations (and tensor perturbations, though subdominant) whereas B-modes are only created by tensor perturbations, i.e. gravitational waves. Figure 1.3 shows the characteristic curl-free and curl-like patterns of E- and B-mode "hot" and "cold" spots, where their behavior under a parity transformation can be easily seen. E-mode polarization was first detected by the DASI experiment in 2002 [48] and B-mode polarization was first detected by the BICEP2 and POLARBEAR telescopes [10, 69], as will be described in greater detail below.

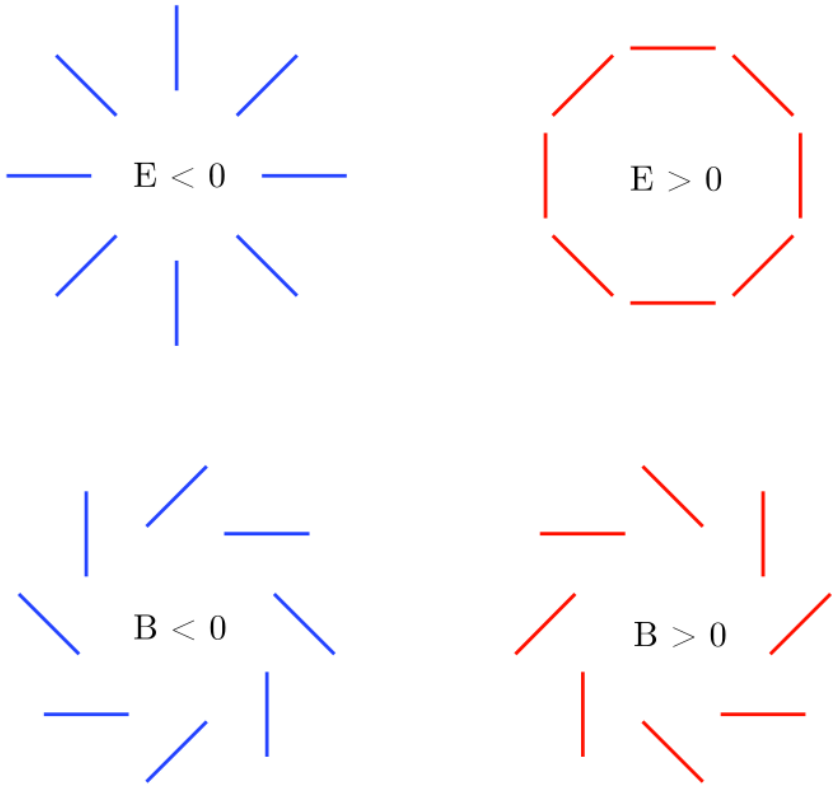

Figure 1.3: Hot and cold E- and B-mode polarization patterns [49]. This highlights the parity differences between E- and B-modes as E-modes are indistinguishable after a parity transformation but B-modes are not the same if mirrored.

1.5 Problems with the Big Bang model

Though the detection of the CMB in 1965 was hailed as definitive proof of the Big Bang, there were some phenomena in the Universe which the Big Bang theory could not explain without invoking specific specific conditions, known as the "fine-tuning" problem. The fine-tuning problem can be broken into the following specific concerns: the horizon, flatness, and magnetic monopoles problems.

1.5.1 Horizon problem

What is so astounding about the CMB is that all points in the sky have the same temperature a few parts in 10,000. Accounting for the size of our observable Universe (horizon), and running back the clock, assuming space-time expands causally (i.e. points that are in causal contact would always have been in causal contact), we find that points on the sky separated by greater than $\sim 1^\circ$ (in our flat Universe) could never have been in causal contact! Why then would the CMB have such a uniform temperature across the sky if points separated by greater than 1° could never equilibrate with other points?!

1.5.2 Flatness problem

We have observed that our Universe is spatially flat – that is our matter-energy density deviates from the critical density by less than one percent[2]. Deviations from critical density would mean the Universe would either gravitationally collapse (if matter-heavy) or expand into nothingness (if energy-heavy). The Universe has had nearly 14 billion years for these deviations from critical density to evolve but we're still flat to within one percent. For our Universe to be this flat today, then the Universe would have to have been flat to one part in 10^{62} at the Big Bang! Deviations from critical density so astronomically small seem extremely unlikely.

[2]Critical density is defined as the density required for a flat Universe.

1.5.3 Magnetic monopole problem

Though we are very familiar with electric monopoles, we have yet to experimentally determine the existence of magnetic monopoles, despite them being perfectly valid within electromagnetism. Grand Unification Theory (GUT) predicts the creation of numerous magnetic monopoles at the high temperatures of the early Universe, which should be easily detectable today. That we have yet to unambiguously detect one magnetic monopole, much less with the density predicted from GUT physics is a significant problem with the standard Big Bang theory. Though this is one specific example, it is indicative of what is known generally as the "exotic-relics problem."

It is possible that the solution to these three specific problems is that this is just the way our Universe came to be – that we are just "lucky" that our Universe exists with these peculiar initial conditions. This is a phenomenally boring answer and stands in the face of centuries (if not millennia) of scientific inquiry. 'Why' has always been the driving question, and so a solution was posited.

1.6 Cosmic Inflation

Inflation, independently proposed by Alexei Starobinsky[3] and Alan Guth in 1979 - 80, is the exponential expansion of the very early Universe around 10^{-36} seconds after the Big Bang, bringing causally connected regions out of causal contact. Within $\sim 10^{-32}$ seconds, the Universe went through around 60 e-foldings, i.e. it expanded by a factor of e^{60}.

This naturally solves the horizon problem as all parts of our horizon were in causal contact before this epoch and thus could equilibrate. Similarly, the flatness issue is resolved. Any curvature would be 'washed-out' by this exponential expansion. A two dimensional example would be the inflating of a balloon. If we have a partially inflated balloon and we look at a one inch circle on its surface, it is clearly very curved. If we now blow up that balloon by many times its original size

[3]As was so often the case during the Cold War, the east and west developed these theories independently. The influence of the Landau way of learning physics during this epoch is unmistakeable and awe-inspiring.

and look at a one inch circle on the new surface, it is much flatter. Similarly, in three dimensions, any initial curvature will be diluted so that our Universe would appear flat today. The magnetic monopole problem is also solved by Inflation. The process which creates magnetic monopoles occurs at energy scales before Inflation starts thus their density is driven down by the expansion to nearly unobservable numbers.

More important than solving the fine-tuning problem, inflation created the anisotropies in the CMB, setting the seeds for structure formation. Inflation took quantum fluctuations in the scalar field and metric of the very early Universe and magnified them to macroscopic scales. In addition to creating anisotropies, this explosive expansion of space-time created gravitational waves that ripple through the Universe and imprint the B-mode signature in the polarization of the CMB.

Though the solution to the fine-tuning problem and the creation of the CMB anisotropies provide evidence for Cosmic Inflation, to prove its existence we need a prediction which we can test. This comes about in these B-modes in the polarization of the CMB. Only gravitational waves can produce B-mode polarization which is correlated over super-horizon scales at the CMB, and only Inflation creates these gravitational waves. A large part of my graduate work has been designing, testing, and analyzing the BICEP2 telescope and data which just recently detected B-mode polarization on the same scales as expected from Inflation. I will discuss the telescope and this result in greater detail later.

Chapter 2

Studying the CMB

Up until now, I have provided a description of the CMB from a qualitative standpoint, stating what we know and why. In this chapter I will discuss how we study the CMB, allowing us to learn so much about our Universe. I will describe how we determine correlations on a temperature map of the CMB and the creation of patterns in these correlations that we observe. I will then describe how we study the polarization of the CMB and conclude with a description of the E-modes and B-modes, as well as cross-correlations between and within temperature and polarization.

2.1 From maps to power spectra

When we study the CMB, we are looking at light from the entire Universe, projected onto the 2-D sky. This gives us a map similar to Figure 1.2. Though this gives us information about the CMB at every point on the sky, we are interested in correlations between points on the sky as a function of their angular separation. Since the anisotropies in the CMB are gaussian, we can characterize them by their two-point correlation function[1]. The temperature field on the sky as observed

[1]We can construct higher order correlation functions to study non-gaussian cosmological phenomena like gravitational lensing but for the science goals of BICEP1 and BICEP2, the two-point correlation function is sufficient.

today is

$$T(\hat{n}) = T_0 \left[1 + \Theta(\hat{n})\right], \tag{2.1}$$

where $\hat{n}$ is the (θ, ϕ) position on the spherical sky, Θ is the temperature fluctuations divided by the CMB monopole temperature ($\frac{\Delta T}{T_0}$), and T_0 is the CMB monopole temperature, 2.73 K.

To study these fluctuations, Θ, over the sky, we need to first choose a basis. It is convenient to work in spherical harmonics, thus we can expand these fluctuations in this basis as

$$\Theta(\hat{n}) = \sum_{\ell=1}^{\infty} \sum_{m=-\ell}^{\ell} a^T_{\ell m} Y_{\ell m}(\hat{n}), \tag{2.2}$$

where the $Y_{\ell m}(\hat{n})$ are the complete set of eigenfunctions on the surface of a sphere. Using the orthogonality of these spherical harmonics, we can relate the a^T_{lm} to the temperature fluctuations by

$$a^T_{\ell m} = \int d\hat{n} Y^*_{\ell m}(\hat{n}) \Theta(\hat{n}). \tag{2.3}$$

Now we can construct the mean and variance of the fluctuations,

$$\langle a^T_{\ell m} \rangle = 0 \tag{2.4}$$

and

$$\langle a^T_{\ell m} a^{*T}_{\ell' m'} \rangle = \delta_{\ell \ell'} \delta_{m m'} C^{TT}_{\ell}. \tag{2.5}$$

Here, ℓ is the multipole moment, which represents the angular separation on the sky. Points separated by one degree map to $\sim \ell = 100$. Larger ℓ implies smaller angular separations, and smaller ℓ implies greater angular separations. Since $-\ell \leq m \leq \ell$, as you get to larger angular separations you have fewer modes on the sky. E.g., for the dipole, $\ell = 2 \rightarrow m = [-2, 1, 0, 1, 2]$, so 5 modes. Thus there is a fundamental limit on the sample variance. This limit is known as "cosmic variance" which states that the uncertainty on C_ℓ scales as

$$\Delta C_\ell = \sqrt{\frac{2}{2\ell + 1}} C_\ell, \tag{2.6}$$

as a minimum.

Since these temperature anisotropies are dominated by the density waves at the surface of last scattering, we can re-write this angular power spectrum in terms of a k-space integral of the power spectrum, $P(k)$, of these density waves following the construction in [26, 7].

$$C_\ell^{TT} = \frac{2}{\pi}\int_0^\infty dk\ k^2 P(k)|\Delta_{T,\ell}(k)|^2, \tag{2.7}$$

where $\Delta_{T,\ell}(k)$ is the transfer function of these temperature fluctuations with respect to the scalar density perturbations. Though the advantage of writing C_ℓ^{TT} in this way this may not be immediately apparent, we will see below that the power spectrum of these scalar modes will be important for measuring the amplitude of the inflationary B-modes.

2.2 Correlations

With Equation 2.5, we can now study correlations across the CMB temperature anisotropy via its angular power spectrum. The most recent temperature power spectrum is from the Planck satellite, shown in Figure 2.1. We can see from this angular power spectrum that there are correlations between temperature fluctuations on all scales across the sky! We divide these correlations into two regimes based on their causality. Correlations on scales separated by greater than about one degree on the sky are non-causal in the standard Big Bang model. Correlations on scales smaller than this occur between points in causal contact and are caused by acoustic wave oscillations in the photon-baryon plasma.

2.2.1 Large-scales

On the super-horizon scales, the CMB is still correlated. These large scales were not affected by evolution of the Universe within the horizon, thus we are seeing the initial conditions of the Universe. We can see that there is a non-uniformity in this regime. This is due to photons getting redshifted due to gravitational wells and is known as the Sachs-Wolfe effect. In the very largest scales, we see a slight upwards tilt. This is due to gravitational potentials from when the Universe was

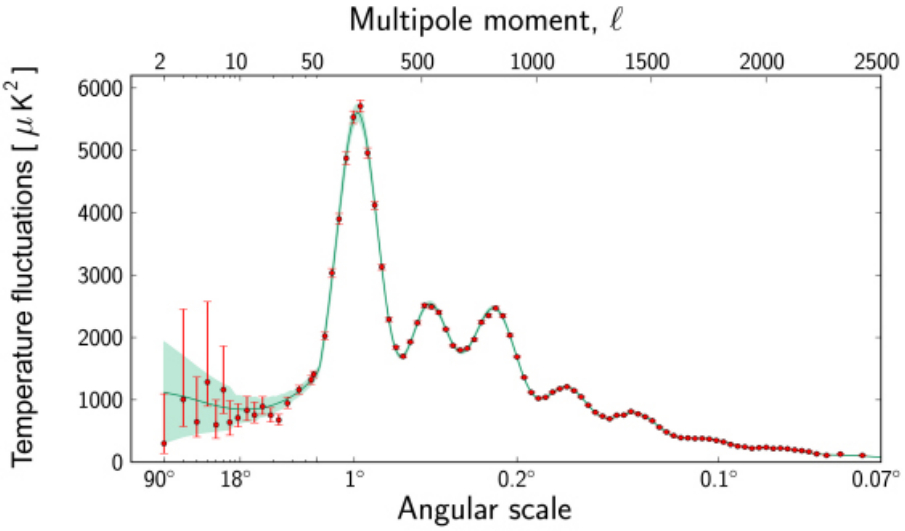

Figure 2.1: The temperature power spectrum as measured by the Planck satellite [59]. The angular separation is shown on the x-axis and the corresponding multipole moments are shown above. The full moon subtends about half a degree on the sky, for reference. In the large angular separation regime, we can see the effects of cosmic variance which increases the error bars. The green line is the best-fit to the ΛCDM cosmological picture.

not matter dominated, e.g. when it was still radiation dominated shortly after recombination, and from more recent times as we became dark-energy dominated.

2.2.2 Small-scales

Within the horizons during recombination, the photon-baryon fluid was compressing and expanding. Just as in any Newtonian fluid, these waves oscillated, as displayed by the peak structure in Figure 2.1. As the pressure waves oscillated through the fluid, they become damped, thus we see the peaks damping out as the scales get smaller.

2.2.3 Cosmological parameters

These correlations are very sensitive to the makeup of our Universe. For example, the location of the first peak is dependent on the curvature of the Universe. In addition, the baryon density will change the height of the peaks as well

as the locations of the higher-ℓ peaks. From the shape of the power spectrum, we can make measurements of the cosmological parameters which define our Universe. From the Planck satellite's measurements of the temperature anisotropies, we now know that the Universe is 13.8 billion years old and it is filled with 68.3% dark energy, 26.8% dark matter, and only 4.9% regular matter [1].

2.3 Polarization power spectra

As discussed in Chapter 1, in addition to the temperature, the CMB is slightly polarized. Studying this polarization signal is slightly more complicated than the temperature; whereas before we only needed the unit vector normal to the CMB sky (i.e. our line-of-sight), we now need the unit vectors perpendicular to this, $\hat{\mathbf{e}}_1$ and $\hat{\mathbf{e}}_2$, to define the polarization. Intuitively, if we look at the polarization of photons on one spot in the sky and then rotate our telescope, the polarization angle will change relative to our detectors though the temperature won't. Of course the photon's polarization doesn't actually change so we need a basis which is sensitive to these rotations.

The natural choice is the Stokes parameter basis from vector calculus. For a photon streaming towards us (which we will define as the $+\hat{z}$ direction), we can write down its electric field as

$$E_x = A_x(t)\cos\left[\omega_0 t - \theta_x(t)\right] \tag{2.8}$$

$$E_y = A_y(t)\cos\left[\omega_0 t - \theta_y(t)\right]. \tag{2.9}$$

If these two components of the electric field are correlated, then the photon is polarized. We define the Stokes parameters as the time averages of combinations of the electric field:

$$I = \langle A_x^2\rangle + \langle A_y^2\rangle \tag{2.10}$$

$$Q = \langle A_x^2\rangle - \langle A_y^2\rangle \tag{2.11}$$

$$U = \langle 2A_xA_y\cos\left(\theta_x - \theta_y\right)\rangle \tag{2.12}$$

$$V = \langle 2A_xA_y\sin\left(\theta_x - \theta_y\right)\rangle \tag{2.13}$$

where Stokes Q describes polarization in a $+$ pattern and Stokes U describes polarization in a $\times$ pattern relative to us, as shown in Figure 2.2. Since the mechanisms behind the polarization at the surface of last scattering only create linear polarizations, we can set the circularly polarized Stokes V term to zero.

If we now rotate out coordinate system by an angle α, we get

$$Q' = Q\cos(2\alpha) + U\sin(2\alpha) \tag{2.14}$$

$$U' = -Q\sin(2\alpha) + U\cos(2\alpha), \tag{2.15}$$

which transforms under rotations as a spin-2 tensor. We can then write these Stokes parameters in terms of spin-2 spherical harmonics, similar to Equation 2.2:

$$(Q \pm iU)(\hat{n}) = \sum_{\ell=1}^{\infty} \sum_{m=-\ell}^{\ell} a_{\pm 2,\ell m}\, {}_{\pm 2}Y_{\ell m}(\hat{n}), \tag{2.16}$$

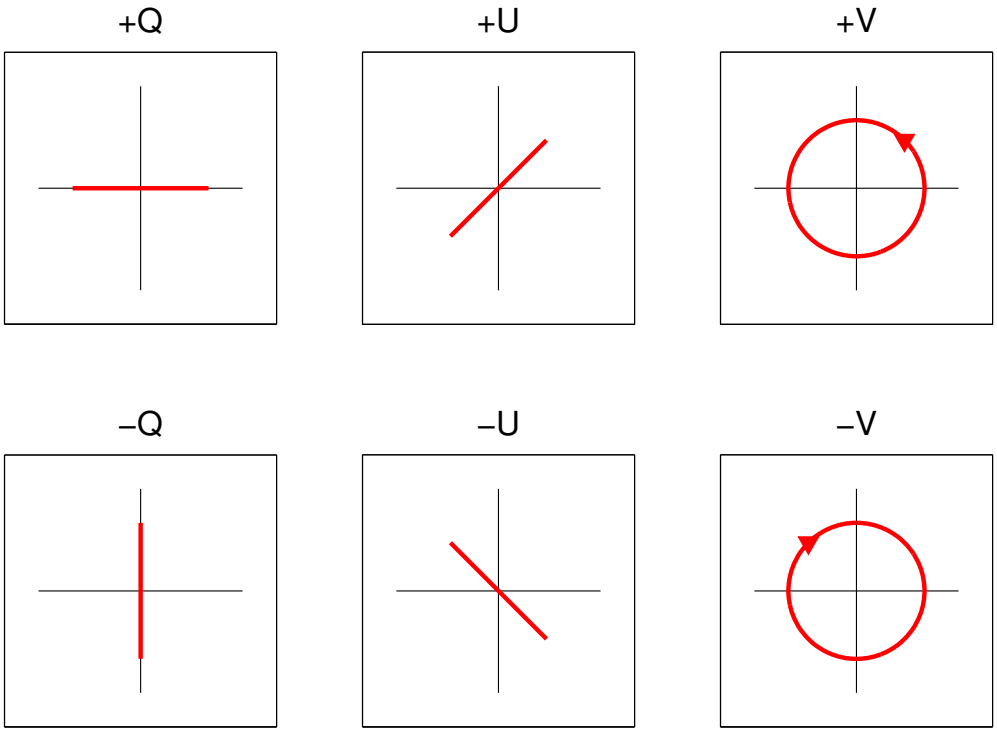

Figure 2.2: The Stokes parameters for describing polarization. $\pm Q$ polarization has a characteristic $+$ pattern and $\pm U$ has a characteristic $\times$ pattern. Since the CMB polarization is linear, we set $V = 0$.

It is important to remember the goal of this exercise: to create a basis for polarization into parity-even and parity-odd modes which does not depend on the orientation of the observer. We can construct these modes via linear combinations of these local Q and U spin-2 spherical harmonic decompositions:

$$a^E_{\ell m} \equiv -\frac{1}{2}\left(a_{2,\ell m} + a_{-2,\ell m}\right) \tag{2.17}$$

$$a^B_{\ell m} \equiv -\frac{1}{2i}\left(a_{2,\ell m} - a_{-2,\ell m}\right), \tag{2.18}$$

which allows us to create scalar quantities for E and B polarization so that we can project them onto spherical harmonics just like the temperature anisotropy

$$E(\hat{n}) = \sum_{\ell=1}^{\infty}\sum_{m=-\ell}^{\ell} a^E_{\ell m} Y_{\ell m}(\hat{n}) \tag{2.19}$$

$$B(\hat{n}) = \sum_{\ell=1}^{\infty}\sum_{m=-\ell}^{\ell} a^B_{\ell m} Y_{\ell m}(\hat{n}). \tag{2.20}$$

We now have the machinery to study the correlations of these modes across the sky:

$$\langle a^E_{\ell m} a^{*E}_{\ell' m'}\rangle = \delta_{\ell\ell'}\delta_{mm'} C^{EE}_\ell \tag{2.21}$$

$$\langle a^B_{\ell m} a^{*B}_{\ell' m'}\rangle = \delta_{\ell\ell'}\delta_{mm'} C^{BB}_\ell. \tag{2.22}$$

2.3.1 E-modes

The parity-even E-mode polarization is dominated by the scalar perturbations during recombination. As with the temperature angular power spectrum, this allows us to study the power spectrum of these scalar fluctuations by rewriting C^{EE}_ℓ as the integral of the scalar power spectrum times the E-mode transfer function, similar to Equation 2.7:

$$C^{EE}_\ell \approx \frac{2}{\pi}\int_0^\infty dk\ k^2 P(k) |\Delta_{E,\ell}(k)|^2. \tag{2.23}$$

Note that this is not exact as tensor modes also generate E-mode polarization but at a level subdominant to those generated by the scalar perturbations.

Figure 2.3 shows measurements of the E-mode angular power spectrum.

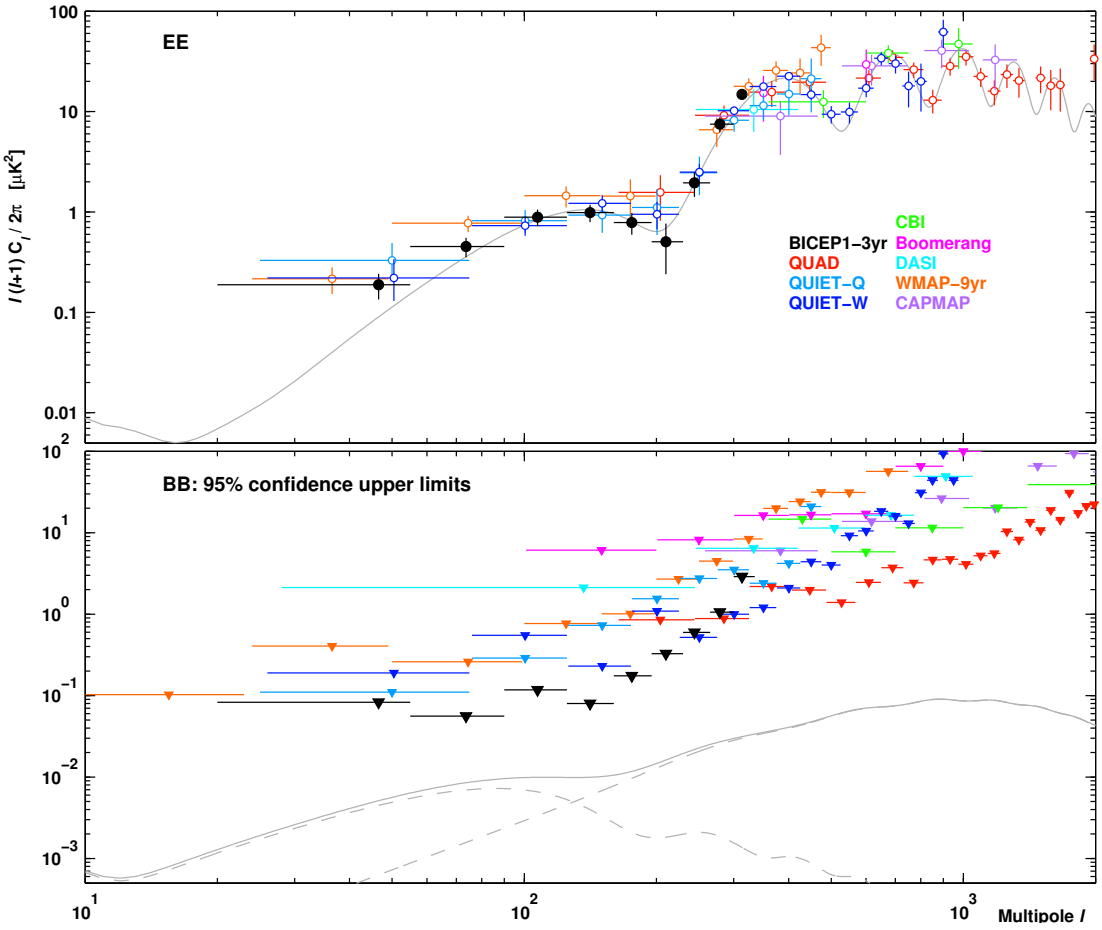

Figure 2.3: E-mode and B-mode power spectra as of March 2014. The dashed gray lines in the B-mode plot are theoretical Inflationary and lensed B-modes for large and small angular scales, respectively. The solid gray line is their combined spectrum. [6]

2.3.2 B-modes

Parity-odd B-modes are generated by the tensor perturbations due to gravitational waves created during Inflation. If we rewrite C_ℓ^{BB} as the integral of the tensor power spectrum times the B-mode transfer function, we get

$$C_\ell^{BB} = \frac{2}{\pi}\int_0^\infty dk\ k^2 P_h(k)|\Delta_{B,\ell}(k)|^2. \tag{2.24}$$

Thus if we can measure the C_ℓ^{BB} angular power spectrum, we can calculate the power spectrum of tensor perturbations from Inflation.

2.3.3 Cross-correlations

So far, I have only discussed C_ℓ^{TT}, C_ℓ^{EE}, and C_ℓ^{BB} which are the auto-spectra of the CMB anisotropies. We can also cross-correlate the temperature and polarizations, generalizing C_ℓ as

$$C_\ell^{XY} \sim \langle a_{\ell m}^X a_{\ell m}^{*Y} \rangle, \tag{2.25}$$

where $X, Y \in \{T, E, B\}$. These cross-correlations give us another dimension to constrain our model of the Universe.

In particular, temperature and E-modes are correlated as the acoustic oscillations are 90° out of phase with the velocity gradients which created the E-modes. Thus we expect a non-zero "TE" angular power spectrum.

"Forbidden" modes

Though one could naively expect correlations between temperature and B-modes or between E-modes and B-modes, however these correlations are expected to vanish as the physics behind their creation is parity invariant. These "forbidden" correlations can occur if there is rotation of the TE or EE spectra whether cosmological, astrophysical, or systematic thus studying these modes can provide very sensitive probes of departures from the standard cosmological picture, unusual astrophysical sources, and instrument performance characterization.

Reionization 'bump'

On very large scales in the polarization power spectra, we see a small peak, as shown in Figure 2.3. This peak is a late-time effect occurring during reionization, somewhere between one hundred million and one billion years after the Big Bang. Reionization is the epoch in which the radiation from the first stars re-ionized the neutral hydrogen in the Universe. This created free electrons which could polarized CMB photons via Thomson scattering, just like at the surface of last scattering. Because this happened so much later in the Universe's history, these correlations appear at large angular scales. Though this reionization 'bump' is not

of interest to Inflationary physics, as is usually the case, one scientist's noise is another scientist's signal.

2.4 Tensor-to-scalar ratio

The culmination of this chapter is one number: r. r is the tensor-to-scalar ratio, which sets the amplitude of the Inflationary B-mode polarization. We define r as

$$r \equiv \left.\frac{\Delta_t^2}{\Delta_s^2}\right|_{k_*} \tag{2.26}$$

where Δ_t^2 is the amplitude of tensor modes and Δ_s^2 is the amplitude of scalar modes for a chosen "pivot scale," k^*.

From Equation 2.7 we can define the amplitude of the scalar modes as

$$\Delta_s^2(k) = \frac{k^3}{2\pi^2}P(k) = A_s(k_*)\left(\frac{k}{k_*}\right)^{n_s(k_*)-1} \tag{2.27}$$

and similarly from Equation 2.24 we define the tensor modes as

$$\Delta_t^2(k) = \frac{k^3}{2\pi^2}P_h(k) = A_t(k_*)\left(\frac{k}{k_*}\right)^{n_t(k_*)}. \tag{2.28}$$

Here, n_s and n_t define the spectral indexes of the scalar and tensor power spectra, respectively. Note that we have just kept to first term of the spectral index. There may be higher order modes such as a "running" term e.g. $dn_s/d\ln k$, or higher derivatives. The pivot scale, k_* is traditionally set to 0.05 Mpc^{-1}, though sometimes set to 0.002 Mpc^{-1} for scalar constraints on r.

As described in [7], a measurement of r probes the energy scale of Inflation, as

$$E_{\text{Inflation}} \sim \left(\frac{r}{0.01}\right)^{1/4} 10^{16}\ \text{GeV}. \tag{2.29}$$

Thus for $r > 0.01$, Inflation would have occurred around the GUT energy scale [7].

2.5 The hunt for r

Once technology improved to the point that the polarized detectors were sensitive enough to detect the tens of nK signal of the B-mode polarization, the

hunt for the primordial B-modes was on. Many experiments operating from the ground, balloons, and space have set upper limits on the B-mode spectrum. As of March 16, 2014, the field looked like Figure 2.4. BICEP1 had set the tightest bounds with $r < 0.65$ to 95% confidence from direct measurements of the B-mode spectrum.

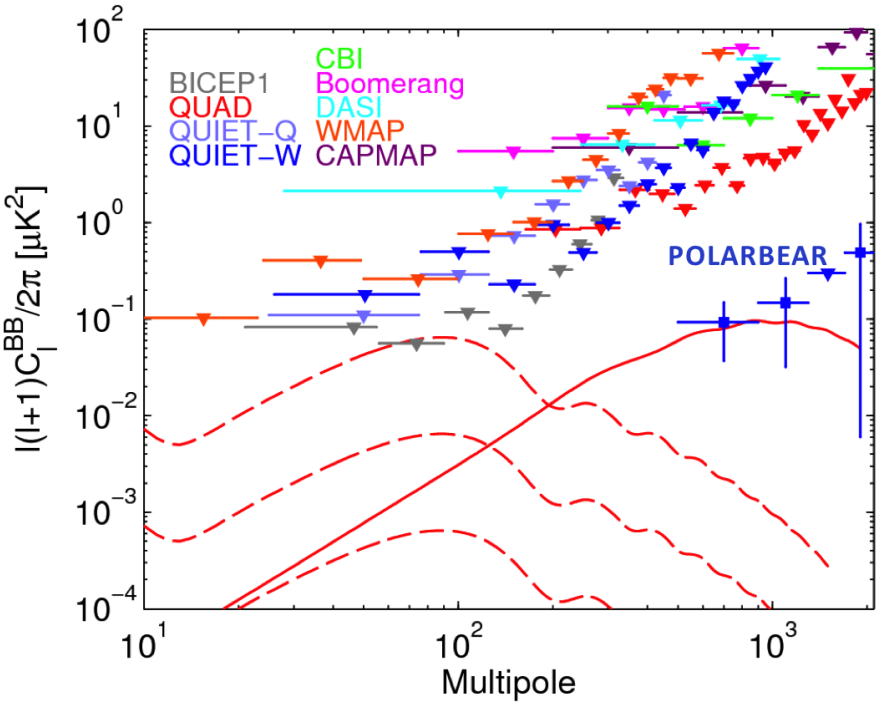

Figure 2.4: The B-mode search prior to BICEP2. Many instruments have placed upper limits on the primordial B-mode spectrum. BICEP1 had the best upper limit with $r < 0.65$. The light blue points at large ℓ are the recent POLARBEAR lensing detection. The solid red line is the lensed B-mode power spectrum, and the dashed red lines are $r = 0.01,\ 0.1,$ and 1 [69].

Constraints from scalar power spectrum

Experiments which precisely measure C_ℓ^{TT} can constrain Δ_s^2 via Equations 2.7 and 2.27[2]. From this scalar amplitude, they can use the definition of r in

[2]Measurements of C_ℓ^{TE} and C_ℓ^{EE} can also constrain the scalar power spectrum. Since they have different transfer functions from the TT power spectrum, they are complementary.

Equation 2.26 combined with the slow-roll consistency equation [20, 45].

$$n_t = -r/8 \tag{2.30}$$

to rewrite Equation 2.26 so that it is only a function of n_s and Δ_s^2.

Though the upper limit on r from studying scalar modes is that $r < 0.11$ with 95% confidence, this number is relaxed if we allow running of the scalar spectral index to $r < 0.26$. [1].

Chapter 3

Polarization Rotation

Observations of the polarizations of radio galaxies and quasars have hinted that there may be an inherent polarization rotation in our Universe [24]. This means that a polarized photon will accrue a phase lag as it propagates through the Universe. Cosmic Microwave Background (CMB) polarization experiments have also found this hint of polarization rotation [47, 58, 73, 42, 35]. Though these methods seem to agree, the constraints are very weak. In this chapter, I'll summarize the constraints from astrophysical sources and from CMB polarization data, as well as mechanisms which could produce polarization rotation such as cosmic birefringence.

3.1 Astrophysical probes of Cosmic Polarization Rotation

In the 1990s, a very specious claim was made that the Universe was birefringent by [56] by studying the polarization of galaxies in the radio frequency band. However, this was quickly and definitively refuted by [29] and [14]. Although they ruled out the very large rotation angle claimed by [56], the re-analysis showed that the polarization observed was still consistent with a small amount of polarization rotation. Several studies since have looked at the polarization of galaxies in the radio and UV bands [14, 71, 25, 40] and have found rotation angles that are very

weakly consistent with a small negative overall rotation, as shown in Table 3.1.

Radio galaxies and quasars will emit due to synchrotron emission, thus if we know the alignment of the magnetic fields, we can infer the polarization alignment. This method however must be corrected for Faraday rotation from magnetic fields in the direction of propagation.

Separate from the radio-band polarization, the polarization of the ultraviolet emission can be used to constrain polarization rotation. In this method, the polarization of a distant galaxy is perpendicular to the elongated axis, thus overall deviations from this polarization orientation can be measured.

Table 3.1: Rotation Angles derived from radio-wave and ultraviolet observations of galaxy polarizations, as shown in [24].

Method	Distance	α (degrees)
Radio	$\langle z \rangle < 0.78$	-0.6 ± 1.5 [14]
UV	$z = 0.811$	-1.4 ± 1.1 [71]
UV	$\langle z \rangle < 2.80$	-0.8 ± 2.2 [25]

3.2 Polarization Rotation from the CMB

The polarization of the CMB is an extremely sensitive probe of cosmic polarization rotation [50]. Any non-zero polarization rotation, whether astrophysical or systematic, mixes the parity-even E-mode polarization and the parity-odd B-mode polarization, inducing correlations between temperature and B-mode polarization, as well as between E-mode and B-mode polarizations with a specific signature [77]. These "TB" and "EB" correlations are expected to vanish in the standard cosmological model due to symmetry, thus these correlations can be a powerful probe of polarization rotating systematics or departures from the standard model, if they are of cosmological origin.

Specifically, polarization rotation leaks C_ℓ^{TE} to C_ℓ^{TB} and C_ℓ^{EE} to C_ℓ^{BB} as

$$\begin{aligned} C_\ell'^{TT} &= C_\ell^{TT} \\ C_\ell'^{TE} &= C_\ell^{TE}\cos(2\alpha) \\ C_\ell'^{EE} &= C_\ell^{EE}\cos^2(2\alpha) + C_\ell^{BB}\sin^2(2\alpha) \\ C_\ell'^{BB} &= C_\ell^{EE}\sin^2(2\alpha) + C_\ell^{BB}\cos^2(2\alpha) \\ C_\ell'^{TB} &= C_\ell^{TE}\sin(2\alpha) \\ C_\ell'^{EB} &= \frac{1}{2}\left(C_\ell^{EE} - C_\ell^{BB}\right)\sin(4\alpha) \end{aligned} \tag{3.1}$$

where C_ℓ' represents the observed angular power spectrum and C_ℓ represents the "true" primordial angular power spectrum. Here, α is the overall rotation angle[1]. Rotated TB and EB spectra for different angles are shown in Figure 3.1. It is important to note that polarization rotation creates both TB and EB correlations with a common angle. This is useful for distinguishing from other mechanisms for polarization leakage, such as systematic contamination.

Several CMB experiments have been analyzed for TB and EB correlations consistent with polarization rotation. The results are shown in Table 3.2. All but one see correlations consistent with a small negative overall rotation.

Table 3.2: Rotation angles derived from the polarization of the CMB along with their statistical and systematic (in parenthesis where available) uncertainties.

Experiment	Frequency (GHz)	ℓ range	α (degrees)
WMAP7 [47]	41+61+94	2 - 800	-1.1 ± 1.4 (± 1.5)
BOOM03 [58]	143	150 - 1000	-4.3 ± 4.1
QUaD [73]	100	200 - 2000	-1.89 ± 2.24 (± 0.5)
QUaD [73]	150	200 - 2000	$+0.83 \pm 0.94$ (± 0.5)
POLARBEAR[69]	150	500 - 2100	-1.08 ± 0.20 (± 0.5)

Measurements of Taurus A

The Crab Nebula, also known as Taurus A, is the remnant of a supernova which occurred in the year 1054 C.E. at right ascension $5^{\mathrm{h}}34^{\mathrm{m}}32^{\mathrm{s}}$ and declination

[1]Though in some texts it is occasionally called $\Delta\alpha$ or $\Delta\chi$.

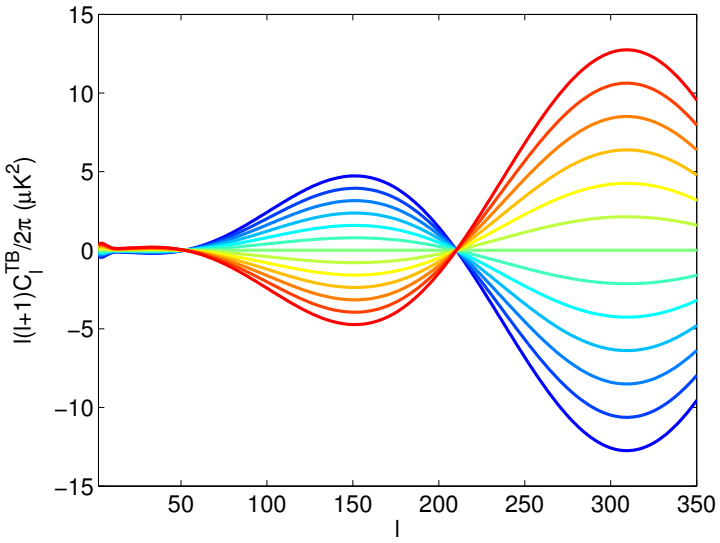

(a) TB

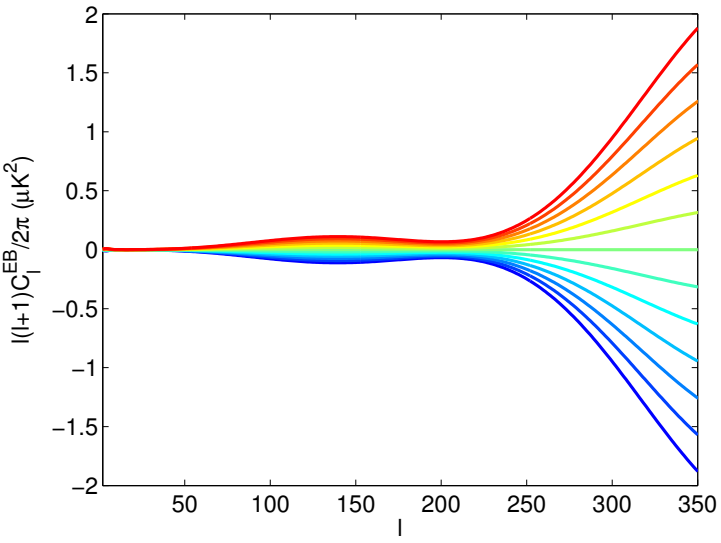

(b) EB

Figure 3.1: Standard ΛCDM power spectra after applying polarization rotation of -3° (blue) to +3° (red), in 0.5° steps, for TB (left) and EB (right).

22°0'52". This supernova was nearly as bright as the moon at its peak and was visible in the day-time sky for three weeks at night for almost two years [37]. It was viewed all over the world by early civilizations; Chinese astronomers kept very detailed records which survive today, and some American Indian petroglyphs which were dated to the era show a bright object near a moon that is believed to be SN1054. I was fortunate enough to see one of these petroglyphs during a hike several years ago in Arizona.

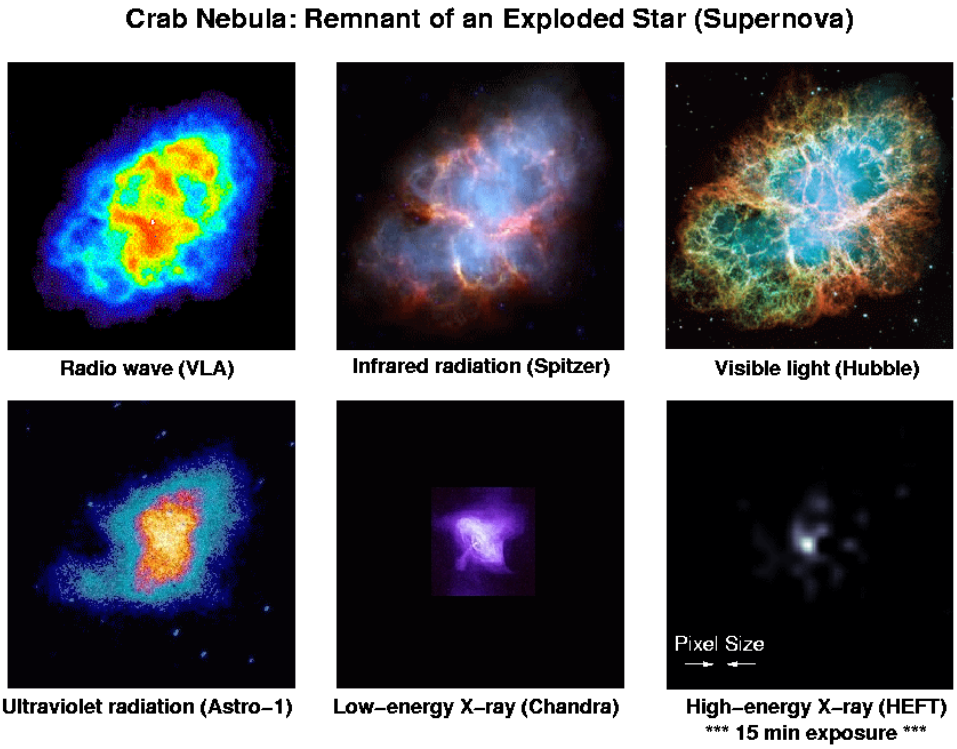

Figure 3.2: Images of Taurus A (Crab Nebula) in radio wave, IR, visible, UV, low energy X-ray, and high energy X-ray. Images courtesy of Nasa

Taurus A (hereafter "Tau A") is an intersection between astronomical sources and the CMB for polarization rotation measurements. Unlike the radio galaxies, Tau A is a polarized nebula around a pulsar. The polarization is due in part to synchrotron emission from the pulsar as well as the interaction of this with the surrounding gas. The polarization angle of Tau A, defined as

$$\alpha_{\rm sky} = 0.5 \arctan\left(\frac{U}{Q}\right) \tag{3.2}$$

has been measured to be 149.9° as observed by a CMB experiment with a 5' gaussian beam[5]. A plot of the polarization map of Tau A can be found in Figure 3.3.

Since Tau A is too close to have accumulated appreciable polarization rotation, it is often used as an astronomical calibration source for CMB experiments. This allows for a check of man-made calibration devices when measuring the polarization of the CMB.

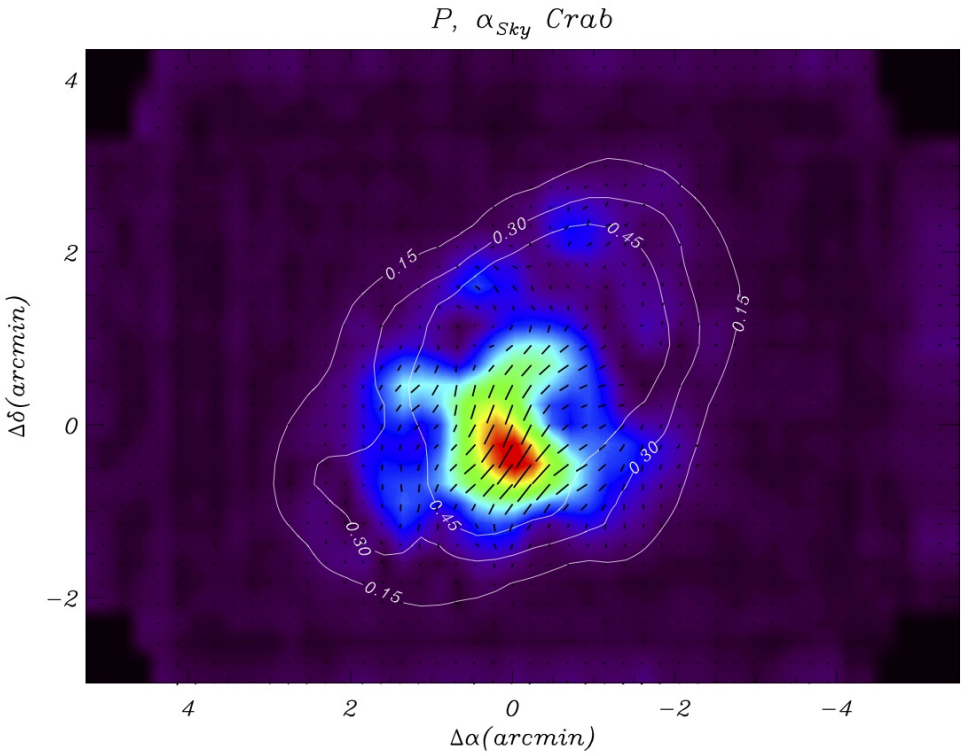

Figure 3.3: Taurus A polarization intensity map $\left(\sqrt{Q^2+U^2}\right)$ with polarization vectors at 90 GHz from [5]. The color scale is 0 to 0.25 K. White contours are of the total Intensity in units of Kelvin.

3.3 Birefringence

For a given wave with linear polarization angle θ, $|\psi(\theta)\rangle$, we can decompose the linear polarization into its right-handed and left-handed circular polarized

components:

$$|\psi(\theta)\rangle = |\psi_R\rangle + e^{i2\theta}|\psi_L\rangle. \tag{3.3}$$

If this wave propagates in a birefringent medium, i.e. one with a different index of refraction for right-handed and left-handed circularly polarized light, n_R and n_L, respectively, then the two polarizations will effectively have different propagating speeds, and thus one will lag behind the other. This will induce a rotation of the polarization $|\psi(\theta)\rangle \rightarrow |\psi(\theta + \alpha)\rangle$. This rotation is dependent on the difference between the indexes and the propagation length:

$$\alpha = \frac{kL}{2}(n_R - n_L) \tag{3.4}$$

or in terms of the propagation velocities,

$$\alpha = \frac{kLc}{2}(v_R^{-1} - v_L^{-1}). \tag{3.5}$$

Thus if we detect a polarization rotation as in Equation 3.1, this would imply the Universe may be birefringent. In other words, the speed of light may depend on its chirality.

To explore how this birefringence might arise in the Universe, we can look at modifications to the standard electromagnetic Lagrangian as laid out in [16],

$$\mathcal{L}_{\text{EM}} = -\frac{1}{4}F_{\nu\lambda}F^{\nu\lambda}, \tag{3.6}$$

where $F_{\mu\nu} = \partial_\mu A_\nu - \partial_\nu A_\mu$. A_μ is the electromagnetic four-potential: $A^\mu = (\phi, \vec{A})$. If we add an interaction term, e.g. the Chern-Simons Lagrangian, $\mathcal{L} = \mathcal{L}_{\text{EM}} + \mathcal{L}_{\text{CS}}$,

$$\mathcal{L}_{\text{CS}} = -\frac{1}{2}p_\alpha A_\beta \tilde{F}^{\alpha\beta} \tag{3.7}$$

where p_α is a four-vector coupling constant and $\tilde{F}^{\alpha\beta}$ is the Hodge dual of the electromagnetic tensor:

$$\tilde{F}^{\alpha\beta} = \frac{1}{2}\epsilon^{\alpha\beta\mu\nu}F_{\mu\nu}. \tag{3.8}$$

$\epsilon^{\alpha\beta\mu\nu}$ is the four-dimensional Levi-Civita symbol.

Physically, the four-vector coupling constant implies a preferred direction in space-time [16]. Writing the four-vector in terms of its space-time components,

$p^\alpha = (p^0, \vec{p})$, we see that the spatial-component, $\vec{p}$, violates any rotation invariance, and the time-component, p^0, prevents invariance under Lorentz boosts. From this four-vector, we can construct an "effective mass" of the photon, where $m^2 \equiv p_\alpha p^\alpha$.

This addition of a Chern-Simons term is equivalent to modifying the current four-vector $J^\nu \to J^\nu + p_\mu \tilde{F}^{\mu\nu}/4\pi$, which modifies the standard tensorial Maxwell's equations

$$\partial_\nu F^{\mu\nu} = 4\pi J^\nu + p_\mu \tilde{F}^{\mu\nu}. \tag{3.9}$$

Thus the Field equations become:

$$\begin{aligned} \vec{\nabla} \cdot \vec{E} &= 4\pi\rho - \vec{p} \cdot \vec{B} \\ -\partial_t \vec{E} + \vec{\nabla} \times \vec{B} &= 4\pi J - p_0 \vec{B} + p \times \vec{E} \\ \vec{\nabla} \cdot \vec{B} &= 0 \\ \partial_t \vec{B} + \vec{\nabla} \times \vec{E} &= 0. \end{aligned} \tag{3.10}$$

To find a solution to these equations (for $\vec{J} = 0, \rho = 0$), [16] proposes the following ansatz for $\vec{E}$:

$$\omega^2 \vec{E} - k^2 \vec{E} + (\vec{k} \cdot \vec{E})\vec{k} = i\left(-p_0 \vec{k} \times \vec{E} + \omega \vec{p} \times \vec{E}\right), \tag{3.11}$$

where ω is the frequency and $\vec{k}$ is the wave vector, or $k^\alpha = (\omega, \vec{k})$ in four-space. $k = |\vec{k}|$. From this, we can get the dispersion relation

$$\omega^2 - k^2 = \pm\left(p_0 k - \omega p \cos\theta\right)\left[1 - \frac{p^2 \sin^2\theta}{\omega^2 - k^2}\right]^{-1/2}, \tag{3.12}$$

where θ is the angle between $\vec{p}$ and $\vec{k}$, $p = |\vec{p}|$, and $+$ or $-$ is for right-handed or left-handed circularly polarized modes, respectively. From Equation 3.12, we see that adding the term p_α splits the waves into two classes with different group velocities:

$$\frac{\partial\omega}{\partial k} = 1 \pm \mathcal{O}(p_\alpha^2) \tag{3.13}$$

hence different propagation speeds.

If we Taylor expand Equation 3.12, we get (to first order)

$$k = \omega \mp \frac{1}{2}\left(p_0 - p\cos\theta\right). \tag{3.14}$$

We can calculate the change in phase, ϕ, of a circularly polarized mode traveling over a distance L as $\phi = kL$. Thus we can calculate the phase difference between right-handed and left-handed circularly polarized modes or, in other words, the rotation of linearly polarized light:

$$\alpha \equiv \Delta\phi = \frac{1}{2}(\phi_L - \phi_R) = -\frac{1}{2}(p_0 - p\cos\theta)L. \tag{3.15}$$

Chapter 4

The BICEP1 and BICEP2 telescopes

The BICEP1 and BICEP2 telescopes are part of a suite of CMB polarimeters designed to study the B-mode signature from inflation. The trailblazing telescope was the Background Imaging of Cosmic Extragalactic Polarization (BICEP, later renamed BICEP1) telescope [43] which observed at the South Pole from 2006 to 2008 [68]. Though the most powerful CMB polarimeter built at the time, its sensitivity after three years of observations only allowed an upper limit on B-modes that $r < 0.70$ at 95% confidence [6]. This was later lowered to $r < 0.65$ using the "self-calibration" technique which I implemented for the first time, and will be described later in this work [42].

The successor to BICEP1 was BICEP2, which observed from 2010 to 2012 [9]; a similar telescope employing significant technological advances that allowed BICEP2 to achieve a mapping speed ten times that of BICEP1. This order of magnitude increase in mapping speed allowed BICEP2 to make a $> 5\sigma$ detection of the inflationary B-modes at the $r = 0.2$ level (and with $r = 0$ disfavored at 7σ) [10].

The Keck array compacted the BICEP2 telescope design to pack five similar telescopes, arranged in a star pattern, on the former DASI mount [64]. Along with BICEP1, this array was instrumental in BICEP2's detection via cross correlations of BICEP2 three-year data set and Keck array two-year data [10]. Soon to be

deployed, BICEP3 will also pack five times the mapping speed of BICEP2 but all in one telescope and at 95 GHz.

My research has focused on the BICEP1 and BICEP2 instruments and data analysis so I will highlight some of their similarities and differences here. A complete description of both telescopes can be found in [68, 9]

4.1 Observations, strategy, and design

Both BICEP1 and BICEP2 employed the same strategy: small aperture on-axis refractor to target the degree-scale peak of the Inflationary B-modes and deep integration of the "Southern Hole." This patch of sky is $\sim$1000 square-degrees, centered at RA = 0 hr, dec = -57.5°, which is known to have minimal contamination from the Milky Way's galactic emission. The telescopes were located in the same observatory at the South Pole to reduce atmospheric contamination. Both telescopes employed cryogenically cooled detectors and were testbeds for the latest detector technology: polarization selecting bolometers (PSBs) and transition edge sensors (TESs) for BICEP1 and BICEP2, respectively.

4.1.1 South Pole observatory

BICEP1 and BICEP2 were located at the Dark Sector Laboratory (DSL), (-89.99° S 44.65° W), at the Amundsen-Scott South Pole station, at the geographic South Pole. This observatory was built for several reasons:

- *Altitude* - The DSL is located at an elevation of nearly 10,000 feet. Due to the low pressure at this altitude, contamination from turbulence is reduced.

- *Low precipitable water vapor* - The South Pole is a frozen desert. Due to the extremely low temperatures (-100° F during the winter), there is very little precipitable water vapor in the air [17]. As demonstrated by the effectiveness of a microwave oven, liquid water is very good at absorbing and re-emitting microwave radiation, particularly near our observing band. Thus observing from the dry Antarctic plateau reduces contamination due to atmospheric water vapor.

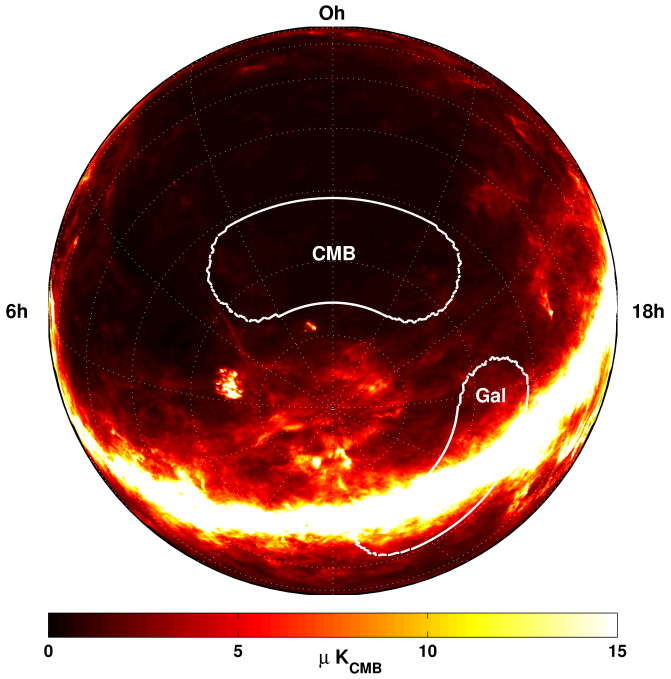

Figure 4.1: CMB observing patch for BICEP1 and BICEP2.

- *Stable weather* - Due to the extreme latitude, there is only one day-night cycle at the South Pole per year. This reduces the frequency of weather events due to the diurnal heating and cooling of air significantly. Clear weather reduces atmospheric noise and thus loading on the detectors.

- *Sky rotation* - Due to the sky's rotation about the pole, the southern hole patch does not rise or set. This allows 24-hour per day observations for deeper, higher signal-to-noise CMB maps.

- *Logistics* - Perhaps the most important advantage to observing at the South Pole is the logistical support. The South Pole has been host to scientific research continuously since 1958, thus the infrastructure has been very well developed. Although transportation (including cargo) is only possible for 3 months out of the year, during this time there are regular flights on C-17 (to McMurdo) and LC-130 cargo planes operated by the U.S. Air Force and Air National Guard. Science support staff are co-deployed to provide everything from fresh water to carpentry. The South Pole offers modern dormitories with four meals a day, a gym, music room, movie room, and fresh baked cookies. It's truly a wonderful place to do science!

Figure 4.2: The Dark Sector of the Amundsen-Scott South Pole station, where the CMB experiments are located. In the foreground is an LC-130 cargo plane used to transport personnel, food, fuel, scientific equipment, etc. to and from the station. LC-130s are outfitted with skis (visible just below the plane) to enable them to land on the snow-pack at the pole. In the center of the picture stands the South Pole Telescope, with the building which housed BICEP1 and BICEP2 directly to the right. To the right of these is the Martin A. Pomerantz observatory (MAPO) which currently houses the Keck array. The small red dots towards the bottom of the picture are researchers walking towards the Dark Sector wearing the "Big Red" extreme cold weather (ECW) jacket.

We were able to build the mount for BICEP1 and BICEP2 inside DSL, with an opening at the roof to allow for observations. This was a significant improvement over previous polar telescopes as personnel could now operate the telescope in the climate controlled lab. Since there are and were several other CMB telescopes which operated at the pole, there has been a buildup of extremely useful tools, equipment, and (extremely important) spare parts. For BICEP2 we installed an HVAC clean room, necessary for in situ installation of the advanced detectors into the cryostat focal plane. In the neighboring Martin A. Pomerantz observatory (MAPO), where the Keck array is located, there is even a dedicated room for electronics and a complete machine shop with a full-time machinist on staff. The South Pole is arguably the best site for microwave observations.

4.1.2 Telescope mount

The BICEP mount, built by Vertex-RSI[1], was designed to allow movement in azimuth and elevation, as well as rotation around the telescope's boresight. The movements are driven by DC motors via belt, friction, and gears for the azimuth, elevation, and boresight axes, respectively. The mount allows for a range of motion of 90° to 50° (from horizontal) in elevation, 400° in azimuth, and 380° around boresight.

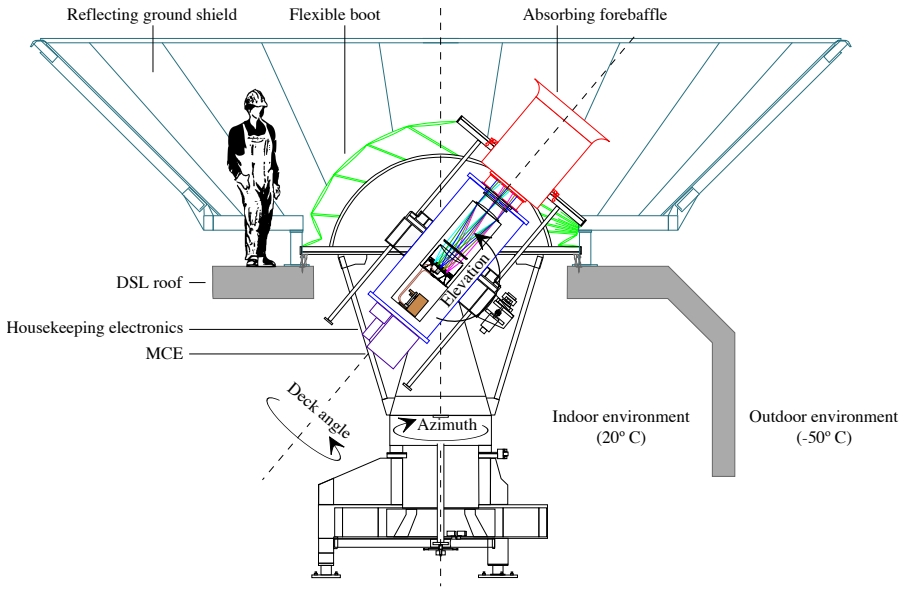

Figure 4.3: The BICEP three-axis mount was housed inside DSL, connected via a flexible boot, shown here in green, to allow observations of the sky while being protected from the elements. The telescope is shown in blue, the baffling is shown in red, and the reflecting ground shield is shown in dark blue.

The DC motors are driven by high-current power supplies which are controlled via a servo system using the programmable multi-axis control (PMAC). This allows for manual and automated scanning, the former being very useful during installation and decommissioning. This setup allowed the mount to be smoothly driven in azimuth by as many as 5° per second.

The mount control included software and physical limit switches to immediately halt motion before damaging the cabling or telescope in the case of an error.

[1]Now General Dynamics Satcom Technologies.

This also included manual "kill" switches for safety.

Attached to the mount was an optical/near-IR camera with a 2" beam designed to resolve stars [78]. During the winter, observations of 24 bright stars at three different boresight rotations are taken (weather permitting). These results are used to fit a seven-parameter pointing model, accounting for the zero points of the azimuth and elevation encoders; the tilt of the azimuth axis in two directions; the tilt of the elevation axis; and two parameters for the collimation of the optical camera relative to the telescope boresight.

4.1.3 Scan strategy

Both BICEP1 and BICEP2 targeted the Southern Hole, where Galactic dust emission is expected to be less than 1% of the sky median [31]. If 5% of the dust signal is polarized, then this would lead to a contamination of the B-mode signature at the level of $r = 0.02$ at 150 GHz [9]. In addition, synchrotron emission in the southern hole is expected to be at the level of the dust or smaller [54]. Both telescopes also observed the Galactic plane (BICEP1 results can be found in [12]). Although I designed and built instruments for BICEP1, I won't describe those measurements in detail here.

For a given elevation and boresight, the telescope slews in azimuth back and forth 64° at 2.8°/s 53 times. This scan is preceeded and followed by an elevation nod and a partial load curve to characterize the health of the telescope during the scan. It then steps up by 0.25° in elevation and scans again in azimuth. It does this for a total of ten elevation steps, then rotates about its boresight and repeats. Since the telescope slews through the same range in azimuth for each elevation step, any scan-synchronous signals can be easily subtracted away as the CMB patch rotates by 15° per hour. Thus any CMB signal moves with respect to azimuth but spurious signals attached to the ground stay fixed.

The science band is defined as the projection of the angular separations studied on the sky onto our time ordered data. This is due to the scanning of the telescope. At the scan speed of 2.8°/s, a signal in the detector time-stream with frequency f corresponds to the multipole value $\ell = 240f$. Thus the Inflationary

B-mode signal, which is located in the multipole range $20 \leq \ell \leq 200$, corresponds to a science band of $\sim$0.1 to 1 Hz.

For complete coverage of the Stokes Q and U polarization parameters, the telescope boresight rotations must be in pairs separated by 45°. Both BICEP1 and BICEP2 observed at two sets of these pairs: (0°, -45°) and (135°, 180°) for BICEP1; and (68°, 113°) and (248°, 293°) for BICEP2[2]. This created two data sets with complete polarization coverage that were used to probe systematic contamination.

The length of the scans is set by the refrigerator and liquid cryogen evaporation rate. For BICEP1, this amounted to a 48 hour cycle. This was improved to 72 hours for BICEP2. For both telescopes, this included a six hour maintenance phase where liquid cryogens were refilled, the refrigerator was cycled, and star pointings were run.

4.1.4 Ground shield and baffling

To prevent stray radiation from entering the optics or pickup due to coupling to the beam's sidelobes for BICEP1 and BICEP2, we employed a ground shield and baffling radiation blocking structure. The ground shield consisted of an eight meter diameter sheet-aluminum cone that extended from just above the roof to one meter above the telescope. This effectively blocked stray radiation from bouncing off the ground and into the telescopes as shown in Figure 4.4.

A series of baffles were attached to the telescope above the window so that any sidelobes would terminate on microwave absorber. These baffles were made from aluminum tubes which were coated with Eccosorb HR-10 absorber and a sheet of Volara[3] for weather-proofing. In addition, the baffles were heated to prevent any snow from accumulating. These baffles were attached with latches for easy removal, if necessary.

[2]For BICEP2, 0° boresight corresponded to the A detectors being sensitive to vertical polarization and the B detectors to horizontal.

[3]http://www.sekisuivoltek.com/

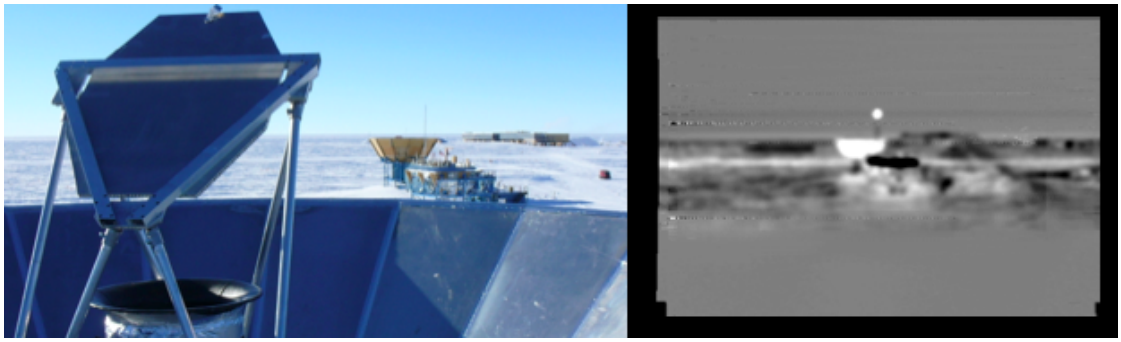

Figure 4.4: Optical and microwave spectrum photos of a microwave source above the MAPO building. The large ground shield at the bottom of the left image effectively looks like the sky, as shown in the right image. Key features are the Keck array ground shield towards the center; the microwave source, the bright dot in the center; and the station, just to the right of the MAPO building. The hexagonal structure in the optical image is the flat-mirror which allowed BICEP2 to view sources below 50°.

4.1.5 Optics

The optical design was nearly identical for BICEP1 and BICEP2. The telescopes were on-axis two-lens refractors, as shown in Figure 4.5. Light enters the telescope through the Zotefoam[4] vacuum window. It then passes through two IR blocking filters heat-sunk to 100 K (80 K for BICEP1) and 40 K to reduce optical loading. Light then passes through the objective lens and an aperture defining cold Lyot stop made from eccosorb all cooled to 4 K. It then goes through another IR filter and an 8.3 cm^{-1} metal-mesh low-pass filter. Finally, it passes through the eyepiece lens and is deposited on the 250 mK focal plane. BICEP1 employed a feedhorn structure to couple to radiation from the eyepiece lens to the detectors. This consisted of a series of three corrugated conical feedhorns: a front-facing and back-facing feedhorn heat sunk to 4 K, and a detector or "PSB" feedhorn at 250 mK. The final IR and metal-mesh filters that were housed between the objective and eyepiece lenses for BICEP2 were located between the back feedhorn and the PSB feedhorn for BICEP1. The lenses, IR, and metal-mesh filters were all coated with an anit-reflective (AR) porous polytetrafluoroethylene (PTFE) layer which was optimized for 150 GHz.

[4]http://www.zotefoams.com

We attached a thin (0.5 mil) sheet of Mylar[5] (biaxially oriented polyethylene terephthalate), held taut between two aluminum rings, to the top of the vacuum window. This membrane had two functions: 1) create a water-free area to prevent any condensation on the vacuum window and 2) sublimate any snow that falls. These were achieved by lightly pressurizing the membrane using room-temperature dry nitrogen gas in the space between the window and the membrane. The warm nitrogen gas, coupled with the room temperature air that would flow over the top of the membrane would immediately sublimate any snowfall.

Towards the end of the BICEP2 2010 summer season, this membrane was replaced with a similar one but was held more taut by the Al rings. This led to occasional common-mode pickup correlated across detector time streams due to vibrations of the membrane. The membrane was replaced in April 2011 with a 0.9 mil BOPP (biaxially oriented polypropylene) membrane and the flow of the dry nitrogen gas was reduced which prevented further membrane noise.

4.1.6 Control software

Both BICEP1 and BICEP2 used generic control program (GCP) software to control operations of the telescopes. Originally designed for the CBI experiment, GCP is now used for several CMB telescopes including the BICEP telescopes, the Keck array, POLARBEAR, and the South Pole Telescope. Set up somewhat like a Unix bash script, GCP interfaces with sub-systems, issuing commands to control motion, detector biases, and data readout.

4.2 Primary differences

Though both telescopes were designed for the same purpose, advances in technology allowed BICEP2 to reach a greater sensitivity than BICEP1. Here, I'll highlight some of the major changes between telescopes including the cryogenic cooling systems, housekeeping electronics and thermal control, detectors and read-out, and the analysis methods used.

[5]Mylar is a registered trademark of Dupont Teijin Films

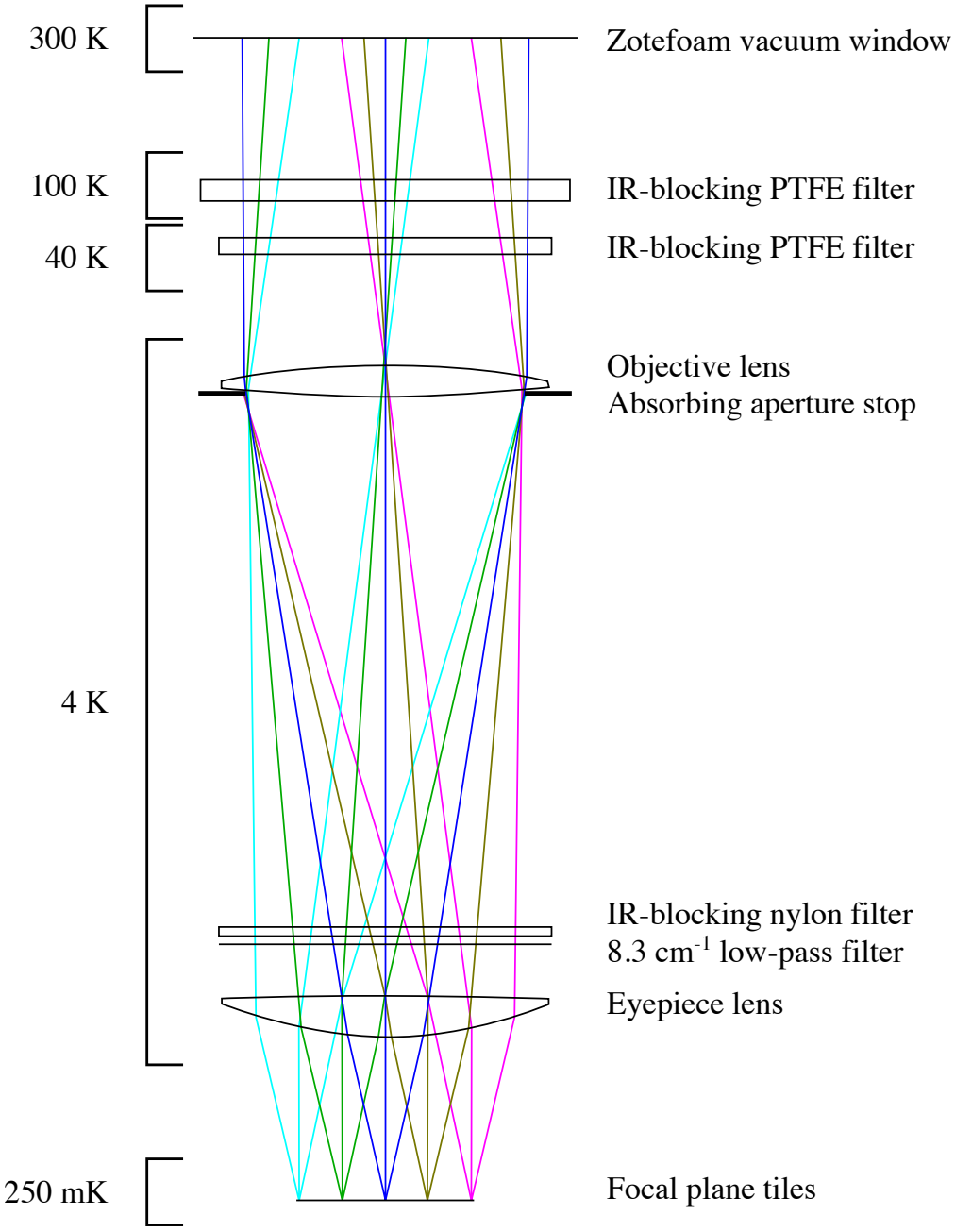

Figure 4.5: The optical design for BICEP2. The colored lines are ray traces originating from the detectors. The optical design for BICEP1 was nearly identical except the filters shown here by the eyepiece lens are within the feedhorn structures.

4.2.1 Cryogenic cooling system

The BICEP1 cryostat[6] was first cooled to 77 K via an internal toroidal liquid nitrogen tank. It then had a separate toroidal liquid helium tank to cool the optics

[6]The vacuum chamber which housed the receiver.

and focal plane to 4 K. In the BICEP2 design, we removed the liquid nitrogen tank in favor of a combination liquid helium and vapor cooled shield (VCS) system. With this setup, the VCS routed the helium boil-off through warmer parts of the cryostat, effectively using the cooling power from the cold gas to cool warmer parts of the telescope. This had the advantage of reducing the amount of liquid cryogens used, making refilling operations much easier.

Once the focal plane was cooled to 4 K, both cryostats employed a three-stage helium sorption fridge [27] to cool the detectors to ~ 250 mK. The refrigerator takes advantage of the temperature drop when changing phases from gas to liquid for helium. Via the ideal gas law, $pV = NRT$, we can see that reducing the pressure while keeping the volume and number of particles constant will reduce the temperature. In a closed cycle, ^{4}He gas is exposed to the 4 K bath via a heat switch. This condenses the gas into a still which reduces the temperature to ~ 1.4 K. This lower temperature is then transferred via another heat switch to gaseous ^{3}He which then condenses to reach ~ 350 mK. This is then transferred to a final ^{3}He stage which reduces the temperature further, to as low as 250 mK.

4.2.2 Sub-Kelvin design and thermal control

The low temperature thermal architecture was designed to isolate the ultra-cold (UC) stage containing the detectors from the higher temperature stages while maintaining rigidity. Both BICEP1 and BICEP2 achieved this using rigid aluminum rings supported by legs made from a low thermal-conductivity material. Vespel was used for BICEP1 and carbon fiber (CF) for BICEP2. The change was motivated by CF's low temperature performance as investigated by [62]. In addition, heat straps were used to transfer the cooling power from the refrigerator to each thermal stage. The heat strap in BICEP1 was a rigid copper plate which was found to induce heating due to vibrations during the telescope's scan. Due to its rigidity, the characteristic frequency of the strap was aliased into the science band as added noise. To reduce the vibrations and push the resonant frequency to below the science band, the thermal strap for BICEP2 was instead created from layers of copper foil, held rigid by a carbon fiber "spine" which was attached via teflon

string and G-10 blocks. A diagram of the sub-Kelvin thermal design is shown in Figure 4.6.

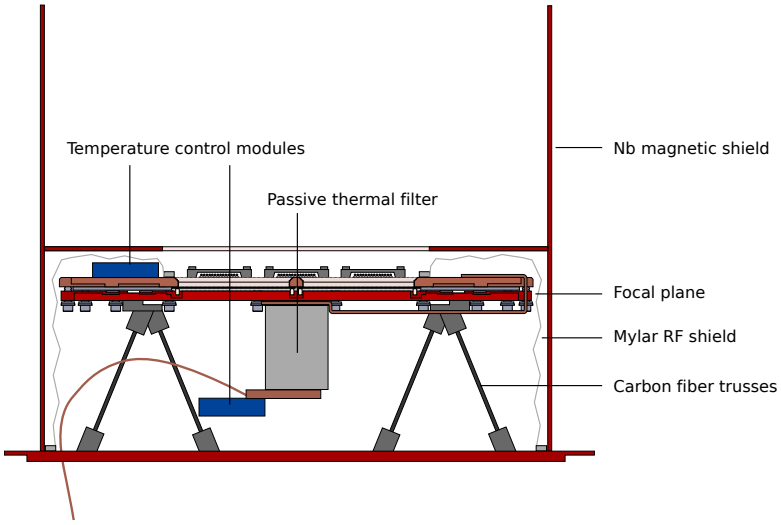

Figure 4.6: Schematic of the inter-cold (IC) and ultra-cold (UC) stages (350 and 250 mK, respectively). The UC stage including the focal plane is supported by a carbon fiber truss structure attached to the IC stage. The UC stage is enclosed within a mylar shield to block stray RF radiation and the entire IC + UC stage is enclosed in a cylindrical magnetic shield made from niobium. Also shown is the passive thermal filter, flexible UC thermal strap, and temperature control modules used for thermal stability of the focal plane.

It was shown in [68] that scan-synchronous thermal fluctuations on the BICEP1 focal plane would be too large to obtain the target sensitivity for BICEP2. To reduce these systematic thermal fluctuations, we employed a two-fold thermal control scheme, employing both passive and active thermal control systems. Part of the passive thermal control was reducing the rigidity of the UC heat strap for BICEP2 but one of the most significant changes was the addition of the passive thermal filter (PTF). The PTF was a 2.5 $\times$ 2.5 $\times$ 5 cm block of 316 stainless steel[7] attached between the copper thermal strap and the focal plane. This acted like a low-pass filter with characteristic frequency of $\sim$ 0.3 mHz, rejecting thermal fluctuations in the science band originating from the fridge side of the UC stage by at least four orders of magnitude.

[7]The alloy 316 was chosen due to its relatively low magnetic susceptibility.

In addition to the passive elements, we employed an active temperature monitoring system. We placed temperature control modules (TCMs) on either side of the passive thermal filter which allowed separate control for the "clean" focal plane-side components and the "dirty" fridge-side components. The TCMs consisted of a resistive heater and two neutron transmutation doped germanium thermistors (NTDs) to monitor temperatures. These allowed us to actively compensate for slow thermal gradients developing on the focal plane, and faster thermal fluctuations which occurred on the refrigerator.

The combination of the active and passive thermal control reduced the thermal systematic contribution to negligible levels for BICEP2. I will describe this thermal control in greater detail in Chapter 5.

4.2.3 Detectors and readout

Perhaps the most defining difference between BICEP1 and BICEP2 was the detector technology used. BICEP1 employed a corrugated feedhorn structure which directed radiation onto the polarization sensitive bolometers (PSBs) whereas BICEP2 employs photolithographed phased arrays of slot-dipoles coupled to superconducting transition edge sensor (TES) bolometers. This technological upgrade allowed for a factor of ten increase in detectors at 150 GHz between BICEP1 and BICEP2. This increase in detector count required a multiplexed readout for BICEP2.

BICEP1

In the BICEP1 design, radiation is coupled from the optics to the bolometers via a corrugated conical feedhorn structure. These feedhorns deposit the radiation onto a pair of PSBs [78]. Each PSB (Figure 4.8) consists of a square mesh of silicon nitride for which one direction has been deposited with gold, making it sensitive to linear polarization in one direction, and a neutron transmutation doped germanium (NTD Ge) thermistor is mounted to register the incident power. This is mounted with a PSB rotated by 90 degrees to achieve complete polarization sensitivity. The PSBs are AC biased and read out using junction-gate field-effect transistor (JFET) amplifiers heat-sunk to 4 K before being passed to room temperature electronics

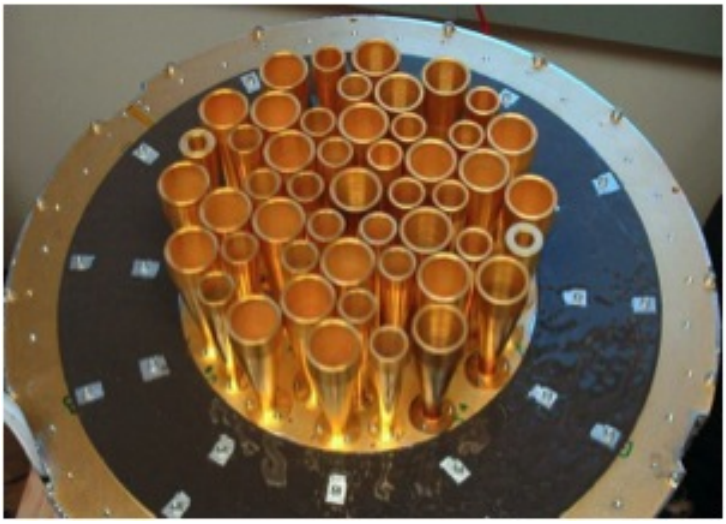

(a) BICEP1

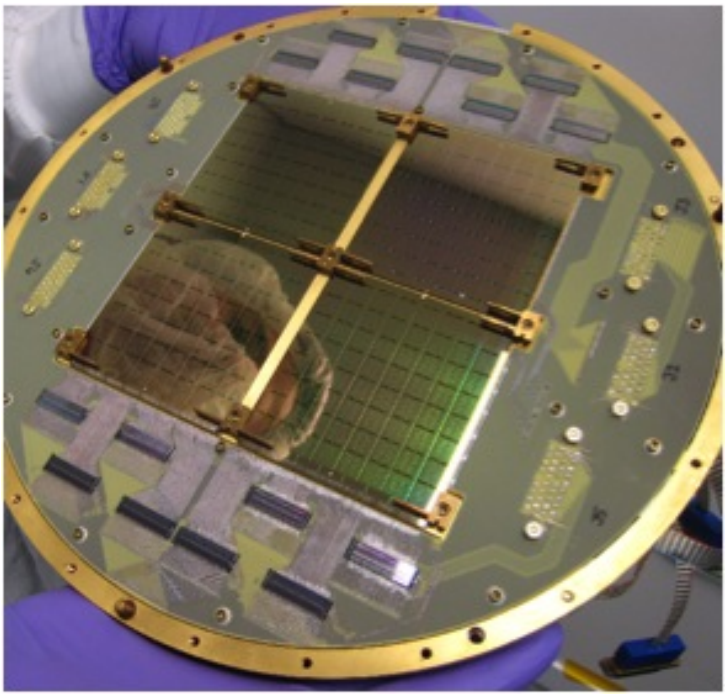

(b) BICEP2

Figure 4.7: The BICEP1 and BICEP2 focal planes. The BICEP1 focal plane consisted of 49 corrugated feedhorn structures attached to pairs of polarized polarization sensitive bolometers (PSBs): 25 at 100 GHz, 22 at 150 GHz, and two at 220 GHz (installed 2007). BICEP2 employed 256 pairs of polarized slot-dipole arrays attached to transition edge sensor (TES) bolometers all operating at 150 GHz.

for filtering and demodulation.

Figure 4.8: BICEP1 polarization sensitive bolometer (PSB).

BICEP2

For BICEP2, the detectors' beams are defined by a phased array of interleaved slot-dipoles sensitive to orthogonal polarizations (as shown in Figure 4.9a). The slot-dipoles are arranged such that both polarizations' beams are coincident on the sky. The individual absorbers are combined via a summing tree which then passes through a band defining integrated three-pole filter. The filter is comprised of three lumped inductors coupled via a T-network of capacitors. Whereas for BICEP1 the frequency cutoff was defined by the metal-mesh filters combined with the feedhorn waveguides, here the lithographed filter defines the band[8].

In-band power is then dissipated via a lossy gold meander onto the TES island (pictured in Figure 4.9). TES bolometers take advantage of the very steep slope in resistance as a function of temperature of a metal in its transition to superconducting. We voltage biased these TES bolometers to this transition such that small changes in temperature due to thermalized radiation led to significant changes in resistance. We then read out the resulting change in current via superconducting quantum interference devices (SQUIDs) [22]. This allowed for

[8]Though the filters define the band, we were susceptible to high-frequency radiation directly coupling to the TES island thus we installed a metal-mesh filter to reject these higher frequencies.

electro-thermal feedback to maintain the TES on its superconducting transition. BICEP2 utilized a two-stage TES: a low saturation power titanium (Ti) TES with transition temperature $\sim$ 500 mK for science observations, and a high saturation power aluminum (Al) TES with transition temperature $\sim$ 1.3 K for high optical loading environments such as in the laboratory or bright calibration sources.

Complementary to the upgrade in detector technology, BICEP2 also employed time-domain multiplexing to reduce heat load on the focal plane due to readout wiring. Multiplexing was accomplished via cryogenic SQUID readout electronics with the capability to register 33 channels at a time.

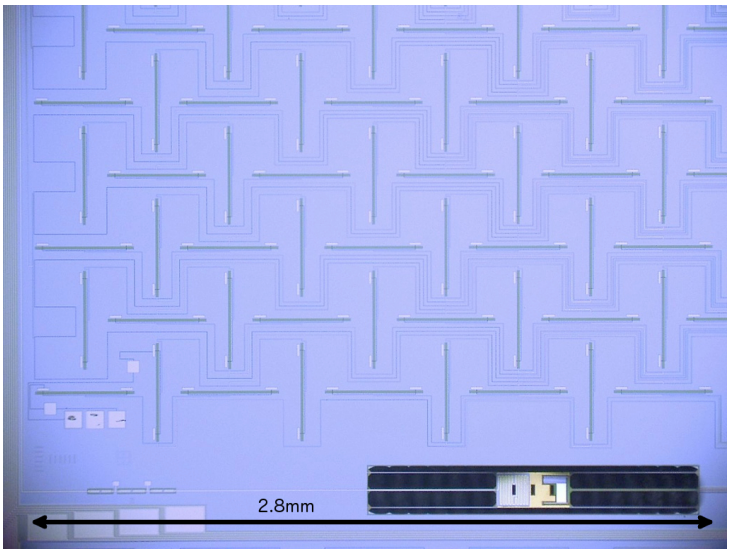

(a) Antennas

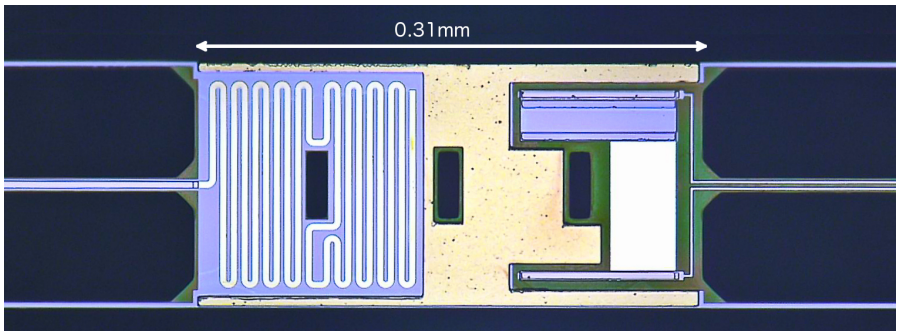

(b) TES island

Figure 4.9: A sample BICEP2 antenna array and transition edge sensor (TES) bolometer.

4.2.4 Analysis techniques

BICEP1 and BICEP2 both employed similar analysis techniques at the map-making level, however some significant changes were made for BICEP2 analysis, including the addition of automatic data selection, deprojection of beam mismatch systematic contamination, and map-based B-mode purification which reduced E-to-B leakage significantly.

Low-level data processing and map-making

For both telescopes, the CMB signal is essentially read out as raw time-ordered data. The first step in the analysis pipeline is to deconvolve the detectors' transfer functions. This was then followed by the removal of data that were contaminated by glitches. The next step is the application of a relative gain correction. In this step, the responses from the scan-bracketing sky-dips (or "el-nods") were regressed against a sinusoidal airmass template to derive the relative gain factors for each bolometer. Each bolometer is divided by its own gain coefficient and then multiplied by the median over the array of "good" detectors. The absolute calibration is done at the map level, further in the analysis pipeline.

Each detector pair[9] timestream was added and differenced to create "pair-sum" and "pair-difference" timestreams. We fit and subtracted a third-order polynomial to reduce atmospheric noise, and a ground-fixed template. Since the CMB moves with respect to azimuth due to sky-rotation, we can bin the timestreams in azimuth and any signals which are coherent are fixed to the ground and can be subtracted. Combining these filtered pair-sum and pair-difference timestreams with pointing data, we constructed temperature and polarization maps, respectively. To add different detector pairs and separate time-ordered-data, we weighted the contributions from each half-scan[10] by the inverse of its variance for BICEP1 and by the inverse variance of the full scan-set[11] for BICEP2, giving higher weight to

[9] A "detector pair" is comprised of the pair of bolometers sensitive to both x and y orthogonal polarizations. For example, although BICEP2 had 512 bolometers, these were defined as 256 detector pairs.

[10] Defined as one scan in azimuth (in either direction) at a given elevation.

[11] A scan set consists of the 106 half scans performed at each elevation step.

channels with lower noise. Deprojection templates were also constructed at this point, though BICEP1 only deprojected relative gain mismatch. Deprojection is described in more detail below.

Automatic data selection

For BICEP2, maps were made for each detector pair over each scan set. During this "pairmap" stage, a series of data quality checks, described in [9] were accumulated. These quality checks were used to remove data taken when the telescope was not operating nominally at the parimap level before the final map accumulation. These checks allowed us to automatically apply different data selection cuts with fine granularity without having to re-accumulate the detector timestreams into maps, saving significant computation time. The introduction of these "round-two" cuts was specific to BICEP2 phenomenologies, it was also advantageous as it allowed more freedom and finer granularity in the data cutting than what was used for BICEP1.

Deprojection

One of the most substantial advancements in data analysis methodology from both BICEP1 and BICEP2 was the inclusion of deprojection of differential beam effects. If the beams for both detectors in a pair have slightly different responses, i.e. gain or ellipticity, then temperature will leak to polarization [65], possibly contaminating the small Inflationary B-mode signal. A more detailed description of the deprojection procedure can be found in [2] and [11]. We used a six-parameter model of beam mismatch (assuming a gaussian beam-shape), shown in Figure 4.10. These are: differential gain and beam-width; differential pointing, which can be decomposed into a dipole oriented along the x-axis and a dipole oriented along the y-axis; and differential ellipticity, which can be decomposed into a quadrupole oriented in a + pattern and a quadrupole oriented in a $\times$ pattern [11].

To mitigate this leakage, we "re-observed" WMAP-7 V band and Planck 143 GHz maps for BICEP1 and BICEP2, respectively, by smoothing the temperature

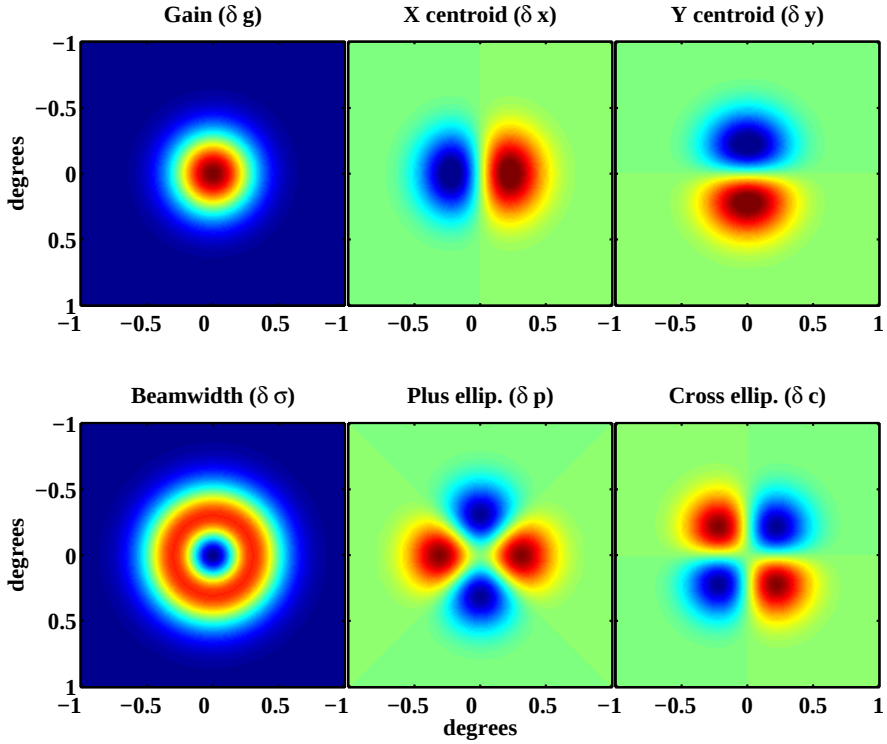

Figure 4.10: Residual beam-shapes of differenced gaussian beams for each of the BICEP2 six-parameter differential beam mismatches: gain, pointing (x and y), beam-width, and ellipticity ($+$ and $\times$) [11].

and derivative maps to the beams of the detectors. From these smoothed maps, we created time-ordered data for each detector pair to simulate the detectors' responses. These were then passed through the low-level analysis pipeline to apply filtering identically to the real data. We then regressed these re-observed template timestreams against the real data and subtracted off the fit. This subtraction filters real signal which can be accounted for by applying B-mode purification.

The deprojection procedure was originally developed with the BICEP1 three-year analysis pipeline, however only differential gain deprojection was available for the final analysis [6]. For BICEP2 data analysis, we extended this deprojection procedure to the full six-parameter differential beam model, however we only applied deprojection to differential gain and pointing. As any deprojection reduces signal-to-noise, we chose to only deproject these two relatively large systematic effects; differential beam-width created a negligible bias, and differential ellipticity

also created a small bias not worthy of deprojection.

B-mode purification

Non-instrumental effects can leak E-modes to B-modes which will contaminated the Inflationary B-mode signal. Filtering, including deprojection, as well as masking the data will induce $E \rightarrow B$ leakage. The mask induces $E \rightarrow B$ leakage as E and B are global quantities; since we only observe a small patch (3%) of the sky for BICEP1 and BICEP2, modes at the edge of the map are ambiguous and cause mode confusion.

For BICEP1, $E \rightarrow B$ leakage was determined via simulation [6]. Simulated detector timestreams were created from realizations of the CMB including E mode polarization but with B explicitly set to zero. These were then binned into maps which were used to create angular power spectra. Thus any B-mode signal was due to $E \rightarrow B$ leakage. The mean of this leakage over the realizations was subtracted from the real data, effectively "de-biasing" the B-mode power spectrum.

With BICEP2 data, the $E \rightarrow B$ leakage was characterized and subtracted by a matrix-based B-mode purification step [10]. First, pixel-pixel matrices were created, which tracked how simulated map pixels were mapped onto the resultant BICEP2 map due to filtering. This is essentially just a matrix-multiplication:

$$\tilde{\mathbf{m}} = \mathbf{R}\mathbf{m}, \tag{4.1}$$

where $\mathbf{m}$ is the vector of $[Q, U]$ values for each pixel in the simulated map, and $\tilde{\mathbf{m}}$ is the same but for the resultant BICEP2 map. We then used the matrix $\mathbf{R}$ to estimate how the covariance matrices for E- and B-modes were affected:

$$\begin{aligned} \tilde{\mathbf{C}}_E &= \mathbf{R}\mathbf{C}_E\mathbf{R}^T \\ \tilde{\mathbf{C}}_B &= \mathbf{R}\mathbf{C}_B\mathbf{R}^T. \end{aligned} \tag{4.2}$$

This filtering matrix, $\mathbf{R}$, induces $E \rightarrow B$ leakage, just as filtering in detector timestream-space. To "purify" this mixing of modes, we transform to a basis of eigenmodes in which the resultant E- and B-mode covariance matrices are perpendicular. We solve

$$\left(\tilde{\mathbf{C}}_B + \sigma^2\mathbf{I}\right)\mathbf{b} = \lambda_{\mathbf{b}}\left(\tilde{\mathbf{C}}_E + \sigma^2\mathbf{I}\right)\mathbf{b}, \tag{4.3}$$

where $\mathbf{I}$ is the identity matrix, σ^2 is a small scaling factor to regularize the problem, and the eigenmodes, $\mathbf{b}$, consist of the vectors of $[Q, U]$ values.

From this, we can construct the "pure" polarization modes as

$$\tilde{\mathbf{m}}_{\rm pure} = \Pi_{\mathbf{b}} \mathbf{m}, \tag{4.4}$$

where $\Pi_{\mathbf{b}}$ is the purification operator, defined as the sum of the outer-product of the eigenmode solutions to Equation 4.3,

$$\Pi_{\mathbf{b}} = \sum_i \mathbf{b}_i \mathbf{b}_i^T. \tag{4.5}$$

Self-Calibration of polarization angles

Any polarization rotation, whether systematic or astrophysical in origin, will positively bias the B-mode power spectrum [42]. To remove this contamination, BICEP2 applied self-calibration of the detector polarization angles. This method was first used in a follow-up analysis of BICEP1 three-year data that I led [42]. This involved rotating the Q and U maps to correct for the non-zero TB and EB correlations consistent with an overall polarization rotation. Self-calibration will be described in greater detail later in this dissertation.

Chapter 5

Thermal Stability of BICEP2

As mentioned in Chapter 4, one major change between BICEP1 and BICEP2 was an upgrade to the thermal stability architecture. This involved hardware and software improvements including passive and active elements. Here, I will describe the thermal architecture, and the thermal stability benchmark and achieved thermal stability calculations.

5.1 Motivation

5.1.1 Detectors

At the time of deployment, BICEP2 was the most sensitive CMB polarimeter ever created. It employed the relatively new[1] transition edge sensor (TES) bolometers. These superconducting detectors had to be cooled to ~ 250 mK to reach the photon-limited sensitivity target. This sensitivity, however, comes at a price. Bolometers, by construction, are attached to a thermal bath (large piece of metal) by a weak thermal link (tiny legs). This makes them excellent microphones, susceptible to vibrational pickup. BICEP1 found a significant amount of vibrational noise would originate at the refrigerator. For BICEP2 we wanted to reject these vibrations before they could thermalize on the focal plane.

In addition, each detector has a thermal responsivity to temperature fluc-

[1] For CMB polarimetry

tuations. If two detectors in a detector-pair have a thermal responsivity mismatch, it could potentially confuse thermal excursions as false polarization.

5.1.2 Telescope scan

Scanning the telescope excites vibrational modes which may resonate in the science band, contamination the small anisotropy signal. Lower speed scanning leads will excite fewer vibrational modes but at the cost of higher $1/f$ noise. BICEP2's scan strategy is designed to maximize coverage of the southern galactic hole with minimal excitement of thermal microphonics. BICEP2 can rotate in three axes: azimuth, elevation, and boresight; however, due to the scanning pattern, detectors are only subjected to movement in azimuth for CMB observations. A scanset is defined as 53 scans of 64° in azimuth[2] at a fixed elevation. This is repeated at 10 elevations separated by 0.25° for each patch. A full observing schedule involves six nine-hour CMB patches, one six-hour CMB patch, and one six-hour galactic patch, with a six hour maintenance period[3] performed at the beginning. This is all done at fixed boresight. The telescope is then rotated by 45° in boresight and the schedule is repeated for complete Stokes Q/U coverage. The telescope is then rotated by 180° and the process is repeated for characterization of systematics as well as jackknife consistency checks. Although stepping in elevation and rotating the boresight are vibrationally very "noisy," these movements are done in between scansets and thus do not affect the data. In addition, azimuth scans are very smooth, with the exception of the turnarounds. To minimize thermal contamination, data taken during these turnarounds are not used in the analysis.

5.2 Thermal design

BICEP2 is cooled with a combination of a toroidal liquid Helium (LHe) tank and a sub-Kelvin ^{4}He/^{3}He/^{3}He sorption refrigerator. The LHe tank cools

[2]Each scan in azimuth is defined as a 64° throw, then back to the origin.

[3]During this time the liquid Helium tank is refilled, the sub-kelvin fridge is re-cycled, and any snow is removed from in/around the telescope.

the optics and telescope assembly to 4 K[4] and the sub-Kelvin refrigerator cools the Focal Plane Unit (FPU) to 250 mK. To mitigate microphonic heating due to resonances, a flexible thermal strap made of layered copper foil supported by a carbon fiber structure is employed from the Ultra-Cooled (UC) stage of the fridge to the FPU. Connecting the FPU to the heat strap is a stainless steel passive thermal filter, meant to act as a low-pass filter, rejecting high frequency vibrational heating from the preceding thermal circuit. To minimize loading from the higher temperature Inter-Cooled (IC) stage, the FPU is supported by four sets of two-member carbon fiber struts. Carbon fiber was chosen for its ratio of elastic modulus to thermal conductivity at sub 4 K temperatures[62]. For increased conductivity, there is an additional copper heat strap which acts as a thermal short between the passive thermal filter and the copper coldplate. There are numerous diode and Cernox thermometers monitoring temperatures throughout the thermal circuit. In addition, there are several temperature control modules (TCMs) that monitor and actively control the temperature at different stages. The TCMs are placed on the UC stage of the fridge, the "dirty" (fridge) side of the passive thermal filter, the copper coldplate, and the detector tiles. Each TCM consists of one resistive heater and two Neutron Transmutation Doped (NTD) Thermistors to monitor temperatures.

Table 5.1: Thermal conductances along the cooling path. The FPU path is defined as the copper FPU coldplate (7 in figure 5.1) to the clean side of the thermal filter (6). The filter path is defined across the thermal filter (4). The strap path is defined from the dirty side of the thermal filter (b) to the fridge (c)

Path	Conductance (W/K)
G_{FPU}	3.65×10^{-4}
G_{Filter}	3.04×10^{-4}
G_{Strap}	3.15×10^{-3}

[4]There is also a two stage vapor cooling system (VCS) which cools filters and outer stages of the telescope that do not need to sit at 4 K.

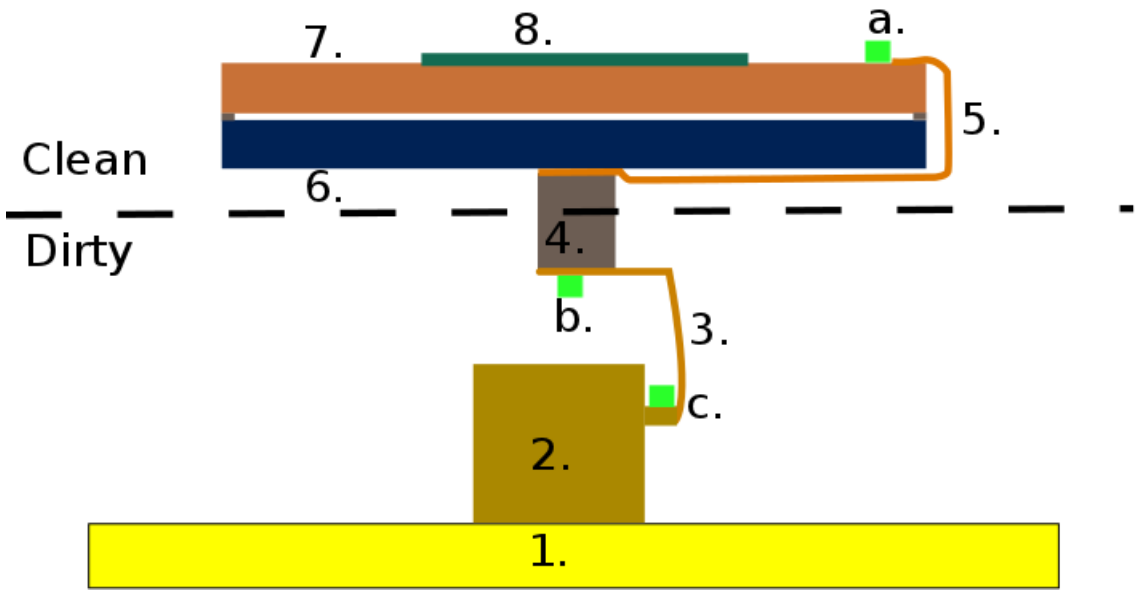

Figure 5.1: Schematic model of the thermal architecture showing the 4 K copper coldplate (1), the three-stage helium sorption fridge (2), UC heat strap (3), passive thermal filter (4), bypass heat strap (5), niobium FPU backplate (6), copper FPU coldplate (7), detector tiles (8); and the temperature control modules (TCMs) on the copper FPU (a), thermal strap (b), and UC fridge connection (c). The clean side is defined as the thermal circuit on the FPU side of the passive thermal filter and the dirty side is defined as the thermal circuit on the fridge side of the passive thermal filter.

5.3 Thermal stability

Due to the very faint signature of the B-modes, it is imperative to have stringent control over systematics. One class of systematics arises from thermal instabilities. The thermal systematics can be classified into two categories: scan asychronous and scan synchronous, with the latter being more problematic thermal events that are repeatable with the scanning of the telescope.

BICEP1's thermal architecture suppressed thermal systematics down to a level of $r \sim 0.1$[68] however, with BICEP2's target of $r \sim 0.01$, more stringent rejection of scan synchronous thermal fluctuations is required. This is achieved by employing passive thermal filtering as well as active thermal control via a proportional-integral (PI) feedback loop.

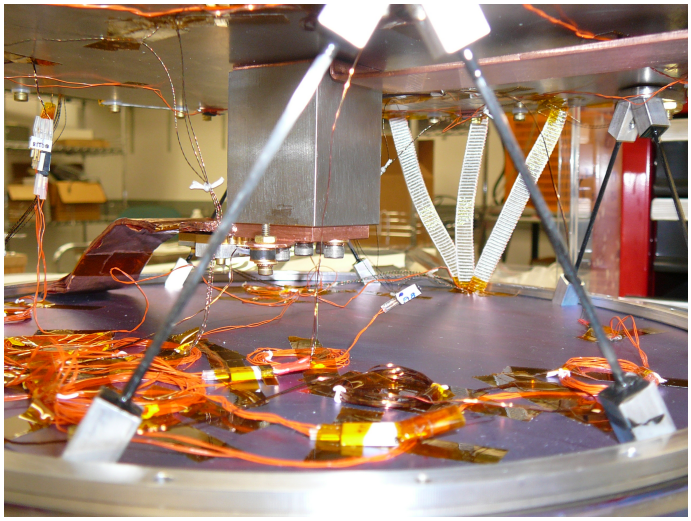

Figure 5.2: Thermal architecture of the Ultra-Cooled stage. Visible in the foreground are the carbon fiber strut support structure. In the background is the passive thermal filter. Also visible are the fridge thermal strap (center) and bypass thermal strap (top right).

5.3.1 Passive thermal control

One of the most significant differences in the thermal circuit between the BICEP1 and BICEP2 telescopes is the addition of a passive thermal filter (as inspired by the distributed passive thermal filter in the Planck HFI instrument[38]). The passive thermal filter is a 2.5 cm × 2.5 cm × 5.5 cm block of 316 stainless steel[5] situated directly under the niobium backplate of the FPU, connecting the FPU to the heat strap from the UC stage of the fridge. The dimensions were chosen to maximize the attenuation of thermal fluctuations in the science band for the space provided without significantly increasing the mass of the focal plane. The passive thermal filter acts as a continuous low-pass filter with characteristic frequency, f_0 = 0.29 mHz, rejecting higher frequency thermal perturbations originating from the fridge (or "dirty") side of the filter. This was tested both before and after the telescope was deployed by pulsing $\sim 1\mu$W of power on the TCM heater on the dirty side of the thermal filter in a square wave pattern with frequencies ranging

[5]The 316 SS alloy was chosen for its relatively low magnetic susceptibility. Although more exotic materials were considered, 316 SS was chosen for its availability and adequate thermal properties.

from 1 mHz to 2 Hz (see figure 5.3). The ratio of the responses was then fit to

$$\frac{T_{\text{clean}}}{T_{\text{dirty}}} = \exp\left[-\sqrt{\frac{f}{f_0}}\right] \tag{5.1}$$

to find the characteristic frequency. We find thermal fluctuations with frequencies in the BICEP2 science band (0.1 - 1 Hz) are reduced by at least four orders of magnitude. This measurement was limited by crosstalk in the NTD readout and the actual achieved rejection is is likely much stronger.

The conductance of the thermal filter was found to be 3.04×10^{-4} W/K (as shown in Table 5.1) which is in excellent agreement with the design goal of 3×10^{-4} W/K. From the characteristic frequency and the conductance, the heat capacity can be calculated from $f_0 = G/(\pi C)$, giving a heat capacity of 0.33 J/K.

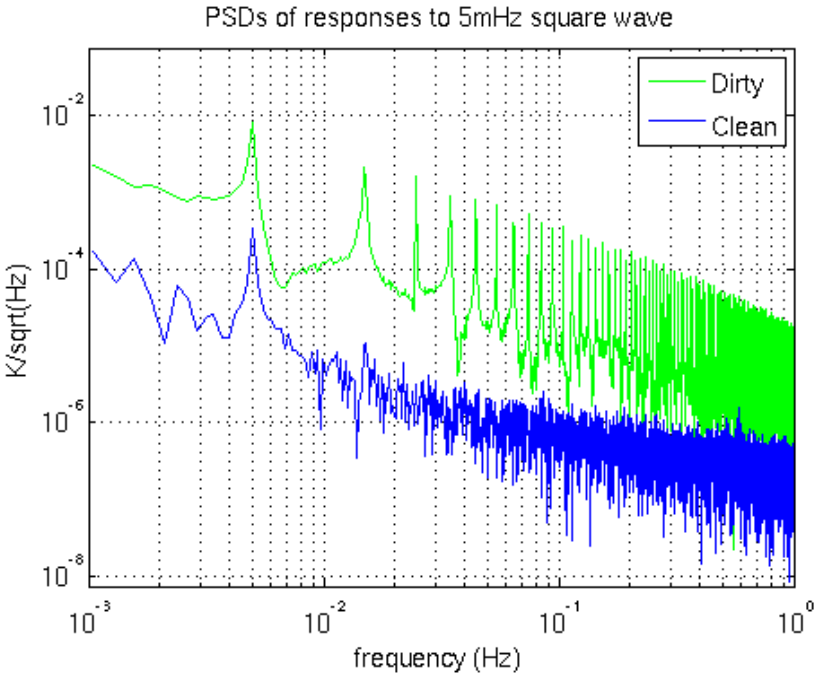

Figure 5.3: PSDs of timestreams of NTDs on clean and dirty sides of the thermal filter to square wave at 5 mHz.

5.3.2 Active thermal control

Although the passive thermal filter rejects high frequency thermal fluctuations, it is important to also have active thermal control to maintain the focal

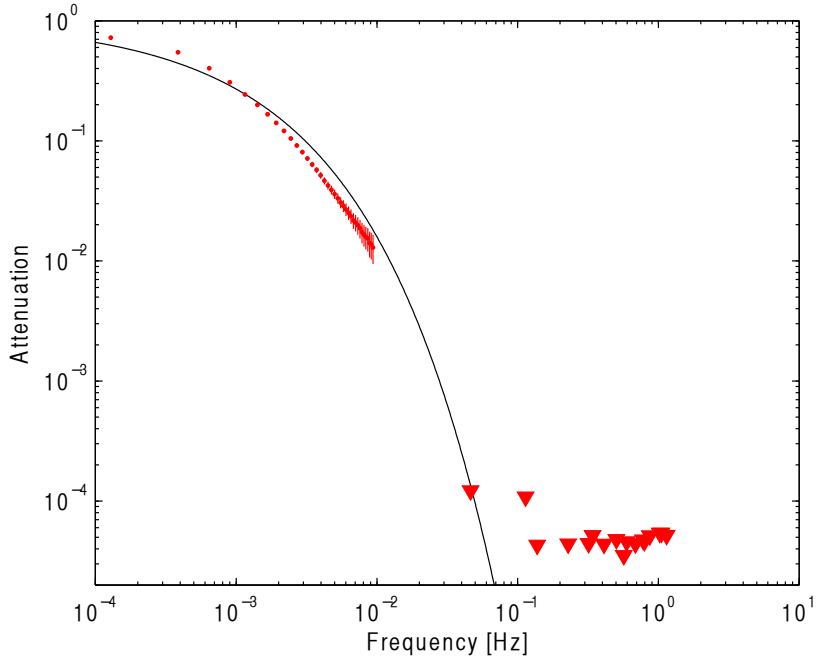

Figure 5.4: Passive Thermal Filter transfer function.

plane consistently at its optimal operating temperature. Active thermal control is implemented by Temperature Control Modules (TCMs) at two locations: on the fridge side of the passive thermal filter and on the copper focal plane coldplate. Each TCM consists of two NTD thermistors and one resistive heater. For the first observing season, the NTDs were alternating current biased at 55 Hz however, with a firmware upgrade between season one and season two, the frequency range was increased and the ability to control the phase of the bias was added, thus allowing use of a nulling circuit which increased the sensitivity of the focal plane NTD thermometers. Since the firmware upgrade, the NTDs are biased at 100 Hz [6] and the output is nulled with a 30 MΩ resistor tuned in bias voltage and phase to maximize the differential signal while maintaining linearity in response. The TCMs are then heated to maintain a slightly higher than base temperature: 280 mK and 272 mK for the clean and dirty sides respectively. The temperature is kept constant by increasing or decreasing the power dissipated from the heater via a PI feedback control loop. The PI coefficients were tuned differently for the clean

[6] 100 Hz was experimentally chosen to minimize the microphonic pickup in the 0.1 - 1 Hz sceince-band range while scanning the telescope.

and dirty sides with a fast response on the dirty side and a slower response on the clean side. A slower response was achieved by reducing the coefficients of the proportional and integral terms in the PI circuit (the coefficient of the differential term being zero).

5.3.3 Thermal stability benchmark

To quantify the required thermal stability, the same method was employed as with BICEP1, where the temperature of the $\ell = 100$ bin of the B-mode power spectrum is transformed to equivalent focal plane temperature from the focal plane array averaged thermal responsivity mismatches between detector pairs. The thermal responsivities were calculated during a 10 mK temperature excursion on the FPU. The median thermal responsivity of good light detectors was found to be 0.19 $\mu K_{CMB}/nK_{FPU}$ after correcting for relative gain mismatch from elevation nods and cross calibrating to WMAP. The median thermal mismatch within detector pairs was then found to be 0.15 $\mu K_{CMB}/nK_{FPU}$. Due to the detector pair mismatches being distributed randomly across the focal plane, the effects will be averaged down as the maps are coadded. Thus, the array averaged thermal mismatch is 0.0042 $\mu K_{CMB}/nK_{FPU}$. For the target $r = 0.01$, the temperature of B-mode power spectrum at $\ell = 100$ is 0.025 μK_{CMB}. Dividing this number by the array averaged thermal mismatch provides a benchmark of 6.0 nK_{FPU} at $\ell = 100$ for a detection of $r = 0.01$. For comparison, BICEP1's thermal stability benchmark was 3.2 nK_{FPU} for a detection of $r = 0.1$[68]. Due to better detector thermal performance, BICEP2's thermal benchmark is more relaxed even for a tighter limit on r.

5.3.4 Achieved Thermal Stability

To calculate BICEP2's achieved thermal stability, angular power spectra were calculated from full season coadded NTD maps using the same pipeline as for CMB maps. For the benchmark calculation, only data from the second season were used due to the increase in NTD sensitivity following the firmware upgrade

between season one and season two. To better approximate how thermal systematics will impact CMB power spectra, the NTD maps were processed similarly to CMB data by subtracting a third order polynomial from the timestreams and applying azimuth fixed template subtraction. From this method, the season averaged temperature fluctuations at $\ell = 100$ are 0.4 $\mathrm{nK_{FPU}}$, an order of magnitude below the 6 nK requirement. From jackknife tests, it is clear that this achieved thermal stability is dominated by the noise of the NTD so real physical thermal fluctuations are likely much lower.

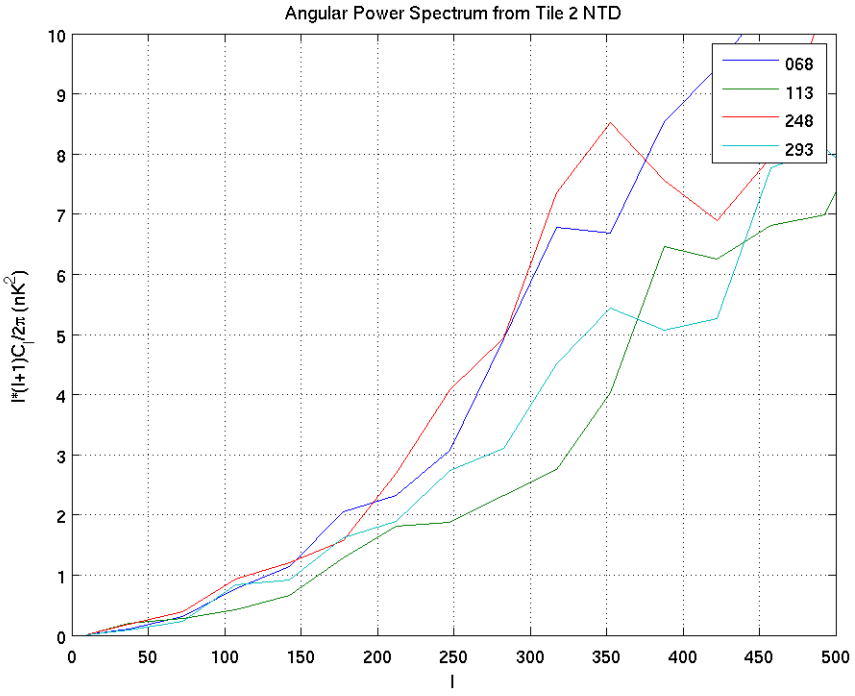

Figure 5.5: Angular power spectrum of second season coadded map of NTD thermometer on one of the four detector tiles for each of the four boresite angles observed. Note that at $\ell = 100$, the power is less than 1 nK^2. Note that the power spectrum rises as ℓ^2, as expected for a constant "white-noise" source.

Figure 5.6 shows maps of the thermal noise over BICEP2's second observing season for NTDs on the dirty and clean side of the thermal filter with active thermal control. It is clear that the active and passive thermal control suppresses temperature fluctuations originating from the fridge by at least two orders of magnitude.

The combination of active and passive thermal controlling elements have reduced the thermal systematic contribution to well below the BICEP2 requirement.

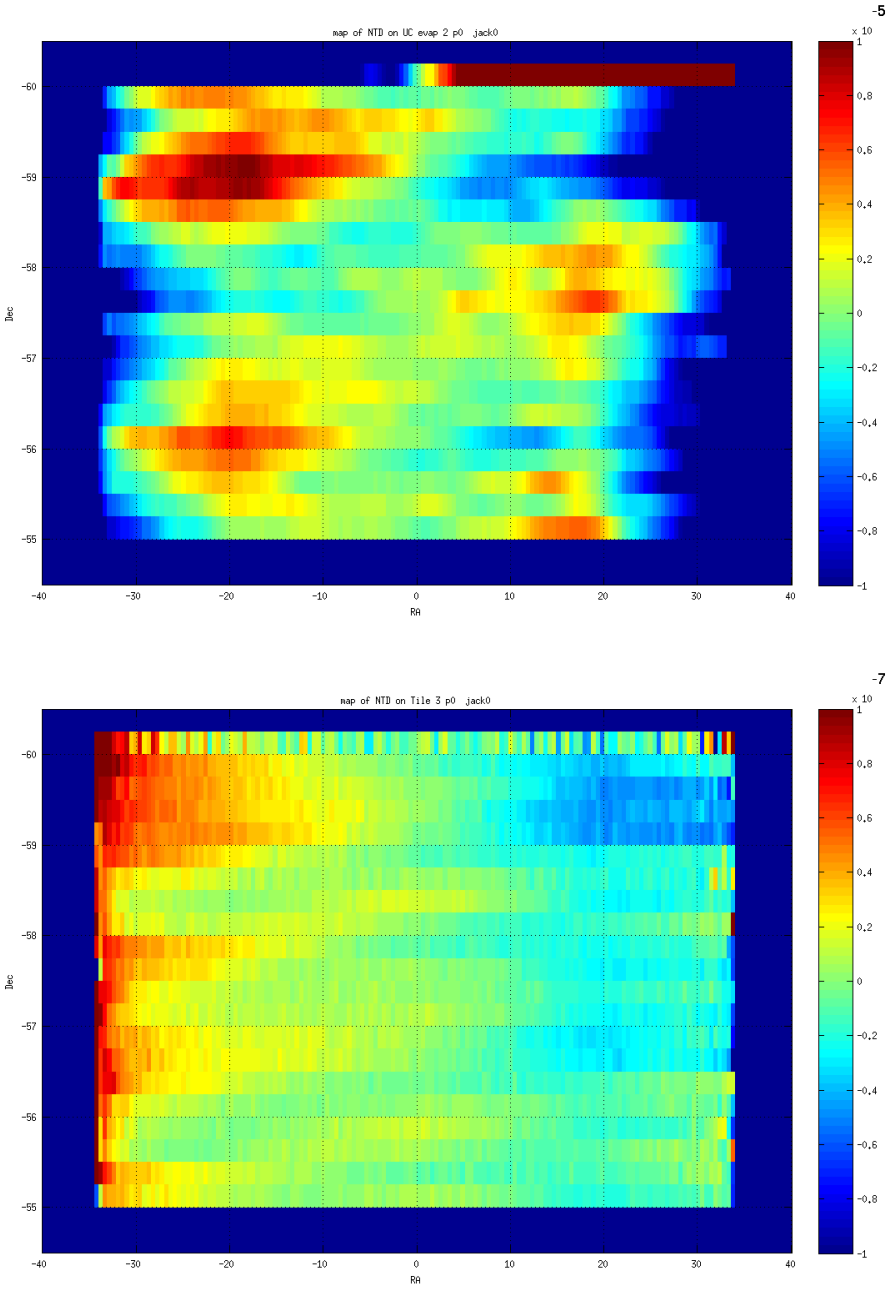

Figure 5.6: Temperature maps for thermal fluctuations coadded over the second season of observation. **Top:** on the fridge temperature control module (TCM). **Bottom:** on the copper focal plane coldplate TCM. Each strip in elevation has been mean subtracted.

Chapter 6

Self-Calibration of BICEP1 Three-Year Data and Constraints on Astrophysical Polarization Rotation

Cosmic Microwave Background (CMB) polarimeters aspire to measure the faint B-mode signature predicted to arise from inflationary gravitational waves. They also have the potential to constrain cosmic birefringence, rotation of the polarization of the CMB arising from parity-violating physics, which would produce non-zero expectation values for the CMB's TB and EB spectra. However, instrumental systematic effects can also cause these TB and EB correlations to be non-zero. In particular, an overall miscalibration of the polarization orientation of the detectors produces TB and EB spectra which are degenerate with isotropic cosmological birefringence, while also introducing a small but predictable bias on the BB spectrum. We find that BICEP1 three-year spectra, which use our standard calibration of detector polarization angles from a dielectric sheet, are consistent with a polarization rotation of $\alpha = -2.77^\circ \pm 0.86^\circ$(statistical) $\pm\, 1.3^\circ$(systematic). We have revised the estimate of systematic error on the polarization rotation angle from the two-year analysis by comparing multiple calibration methods. We also

account for the (negligible) impact of measured beam systematic effects. We investigate the polarization rotation for the BICEP1 100 GHz and 150 GHz bands separately to investigate theoretical models that produce frequency-dependent cosmic birefringence. We find no evidence in the data supporting either these models or Faraday rotation of the CMB polarization by the Milky Way galaxy's magnetic field. If we assume that there is no cosmic birefringence, we can use the TB and EB spectra to calibrate detector polarization orientations, thus reducing bias of the cosmological B-mode spectrum from leaked E-modes due to possible polarization orientation miscalibration. After applying this "self-calibration" process, we find that the upper limit on the tensor-to-scalar ratio decreases slightly, from $r < 0.70$ to $r < 0.65$ at 95% confidence.

6.1 Introduction

The cosmic microwave background (CMB) is a powerful cosmological probe; recombination physics, structure formation, and the cosmological reionization history represent only a small subset of the phenomena probed by its temperature and polarization anisotropy. In addition, several aspects of fundamental physics can be constrained by CMB observations, the most familiar of which are inflationary physics revealed via the imprint of primordial gravitational waves in the polarization of the CMB and the masses of neutrinos which can be probed via gravitational lensing by dark matter. These phenomena create B-mode polarization at the sub-μK level.

Cosmological information can be extracted from the CMB's power spectra. Out of the six possible pairings of the temperature anisotropy T and polarization E- and B-modes, only four have non-vanishing expectation values in the ΛCDM cosmological paradigm. The expectation values of the TB and EB cross-correlations vanish in the standard cosmological model due to parity symmetry but may assume non-vanishing values in the presence of systematics, astrophysical foregrounds, or, more interestingly, parity-violating departures from the standard models of electromagnetism and gravity. Any mechanism capable of converting E-

Table 6.1: Previous rotation angle constraints from CMB experiments, following [35]. Systematic uncertainties are shown in parentheses, where provided.

Experiment	Frequency (GHz)	ℓ range	α (degrees)
WMAP7 [47]	41+61+94	2 - 800	-1.1 ± 1.4 (± 1.5)
BOOM03 [58]	143	150 - 1000	-4.3 ± 4.1
QUaD [73]	100	200 - 2000	-1.89 ± 2.24 (± 0.5)
QUaD [73]	150	200 - 2000	$+0.83 \pm 0.94$ (± 0.5)

to B-mode polarization necessarily leaks the TE and EE correlations to TB and EB, respectively.

A detection of TB and EB correlations of cosmological origin could undermine the fundamental assumptions of parity symmetry and Lorentz invariance by showing that our Universe possesses a small degree of chirality. This phenomenon can be best revealed by CMB polarization where minuscule effects can accrue to observable levels over the 13.8 Gyrs since CMB photons last scattered from the primordial plasma. This preferred chirality can be induced by the coupling of a pseudo-scalar field to either Chern-Simons-type terms in the electromagnetic interaction [16, 15, 14] or the Chern-Pontrayagin term in the case of gravitational interactions [50, 3, 4]. This work constrains the parameters in a scale-independent cosmological birefringence model as well as investigating frequency-dependent scale-independent models. Current best constraints (not including this work) on scale-independent cosmological birefringence from CMB experiments are shown in Table 6.1. Though constraints on scale-dependent birefringence models have been reported with WMAP data [76, 34, 33], we do not provide such constraints in this work. A 3σ detection of cosmic birefringence was reported from combined WMAP, BOOMERanG, and BICEP1 two-year results (while explicitly excluding QUaD data) in [75]. This work was later updated to include the impact of systematic effects at the levels reported by the three experiments and the significance reduced to 2.2σ [74].

BICEP1 has set the most stringent constraints on the CMB's B-mode power spectrum [18, 6] in the multipole range $30 < \ell < 300$. BICEP1 also measured the TB and EB power spectra in this range[18, 6]. These TB and EB modes are

extremely sensitive probes of departures from the standard cosmological model. In this work, we analyze the full BICEP1 three-year spectra [6] for evidence of polarization rotation, considering systematic uncertainties including our primary and alternate polarization calibrations, and exploring constraints on cosmological birefringence. We then use this polarization angle to "self-calibrate" detector polarization orientations and calculate the tensor-to-scalar ratio from the "self-calibrated" BB spectrum.

The outline of the paper is as follows: Section 6.2 contains a review of polarization rotation and how it affects the observed CMB power spectra. The data sets and analysis procedure are described in Section 6.3. Results and consistency checks are presented in Section 6.4. The impact of instrumental systematics is discussed in Section 6.5. Consistency of the data with different birefringence models are in Section 6.6. Application of "self-calibration" and its effect on the tensor to scalar ratio, r, are in Section 6.7, and we discuss our results in Section 6.8.

6.2 Polarization Rotation of the CMB Power Spectra

The CMB can be described by the statistical properties of its temperature and polarization. E- and B-mode polarization can be formed from linear combinations of the Stokes Q and U parameters. Maps of the temperature, T, and Stokes parameters, Q and U, are expanded in scalar and spin ± 2 spherical harmonics [63, 41] to obtain

$$\begin{aligned} T(\hat{n}) &= \sum_{\ell,m} a^T_{\ell m} Y_{\ell m}(\hat{n}) \\ (Q \pm iU)(\hat{n}) &= \sum_{\ell,m} a_{\pm 2,\ell m}\ {}_{\pm 2}Y_{\ell m}(\hat{n}), \end{aligned} \tag{6.1}$$

where the E- and B-modes of polarization have expansion coefficients $a^E_{\ell m}$ and $a^B_{\ell m}$ which can be expressed in terms of the spin ± 2 coefficients

$$a_{\pm 2,\ell m} = a^E_{\ell m} \pm i a^B_{\ell m}. \tag{6.2}$$

The spherical harmonic coefficients, $a_{\ell m}$, are characterized by their statistical properties

$$\begin{aligned} \left\langle a^X_{\ell m} \right\rangle &= 0 \\ \left\langle a^{X*}_{\ell m} a^{X'}_{\ell' m'} \right\rangle &= C_\ell^{XX'} \delta_{\ell\ell'} \delta_{mm'}, \end{aligned} \tag{6.3}$$

where X and X' are either T, E or B. Here, $\langle a \rangle$ stands for the ensemble average. The polarization modes, E- and B-, are pure parity states (even and odd, respectively) and thus the correlation over the full sky of the B-mode with either the temperature or E-mode polarization vanishes [63, 41]. However, if the polarization of the CMB is rotated, there will be a mixing between E and B, subsequently inducing TB and EB power spectra (Figure 6.1):

$$\begin{aligned} C_\ell'^{TT} &= C_\ell^{TT} \\ C_\ell'^{TE} &= C_\ell^{TE} \cos(2\alpha) \\ C_\ell'^{EE} &= C_\ell^{EE} \cos^2(2\alpha) + C_\ell^{BB} \sin^2(2\alpha) \\ C_\ell'^{BB} &= C_\ell^{EE} \sin^2(2\alpha) + C_\ell^{BB} \cos^2(2\alpha) \\ C_\ell'^{TB} &= C_\ell^{TE} \sin(2\alpha) \\ C_\ell'^{EB} &= \frac{1}{2} \left(C_\ell^{EE} - C_\ell^{BB} \right) \sin(4\alpha). \end{aligned} \tag{6.4}$$

No assumption has been made here as to the source of this rotation, namely whether or not it is cosmological. In the literature, α is identified with the birefringence rotation angle (see [47, 73]), though here it is used to denote polarization rotation of any origin.

6.3 Data and Analysis Methodology

BICEP1 observed for three years at the South Pole in three frequency bands: 100, 150 and 220 GHz, and released two year results from 100 and 150 GHz frequency-combined spectra in [18] and three year frequency combined spectra in [6]. Results from the BICEP1 100, 150, and 220 GHz observations of the galactic plane are in [12] and from Faraday Rotation Modulators in [53].

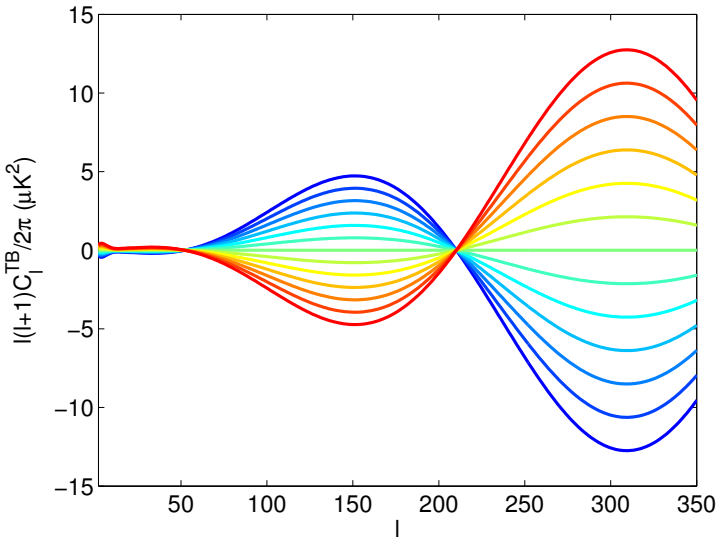

(a) TB

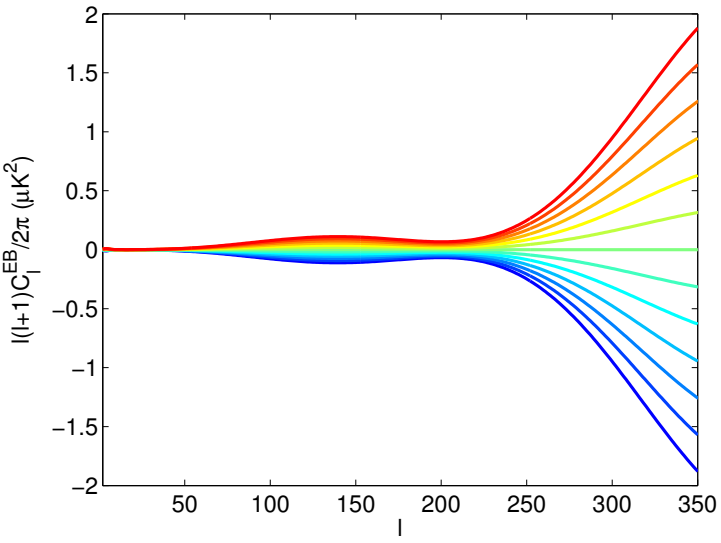

(b) EB

Figure 6.1: Standard ΛCDM power spectra after applying polarization rotation of -3° (blue) to +3° (red), in 0.5° steps, for TB (left) and EB (right).

We employ maximum-likelihood estimation for determining the best-fit polarization rotation angles of the power spectra following Equation 6.4. We use two methods to construct the likelihoods, a Gaussian bandpower likelihood approximation and the Hamimeche-Lewis likelihood construction [36].

6.3.1 Data Sets

We calculate rotation angles from the three-year frequency combined "all-spectra" estimator, where "all-spectra" is defined as $TE + EE + BB + TB + EB$. We can break this down by frequency and by spectral estimator for consistency checks. From this, we get four frequency subsets consisting of the two frequency auto-spectra: 100 GHz auto-spectra (denoted "100") and 150 GHz auto-spectra (denoted "150"), and the two frequency cross-spectra: 100 GHz cross-correlated with 150 GHz (denoted "cross") and 150 GHz cross correlated with 100 GHz (denoted "alt-cross"). Note that although the EE and BB spectra are identical for the "cross" and "alt-cross" data sets, the TB and EB spectra are not, e.g., $T^{100}B^{150} \neq T^{150}B^{100}$.

In addition, we have four spectral combinations to constrain α: the TB and EB modes as well as the combination of TB+EB, and all-spectra: TE+EE+BB+TB+EB since polarization rotation also affects TE, EE, and BB; however, from Equation 6.4, we can see that for small α the rotated TE, EE, and BB deviate from the unrotated spectra by order α^2 and thus their constraining power for α is much weaker than the TB and EB spectra, which are linear in α. In addition, since they are quadratic in α, the sign of α cannot be directly determined. TB or EB break this sign degeneracy. These are not independent estimators but are useful as any unexpected discrepancies can be used to test the validity of the analysis.

6.3.2 Likelihood Analysis

We employ two likelihood constructions for this analysis: a Gaussian bandpower likelihood approximation and the more accurate Hamimeche-Lewis (HL) likelihood approximation [36]. The two likelihood constructions produce similar

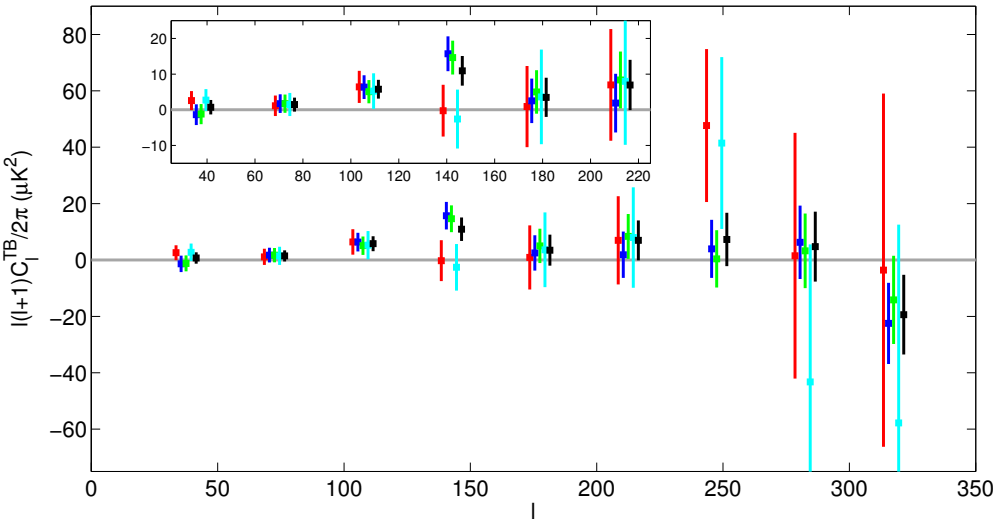

(a) TB

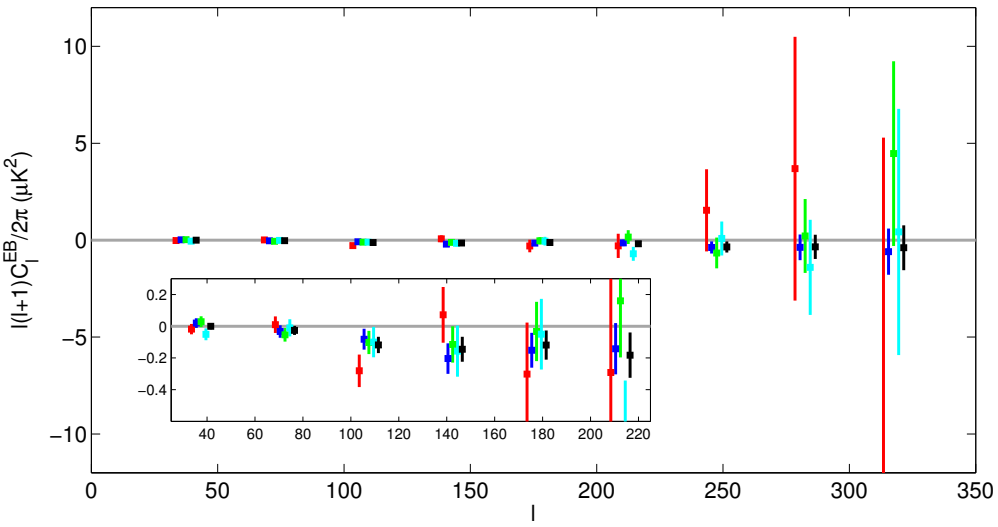

(b) EB

Figure 6.2: BICEP1 TB and EB power spectra for all frequency combinations: 100 GHz auto-spectra (red), 150 GHz auto-spectra (blue), 100 $\times$ 150 GHz cross-spectra (green), 150 $\times$ 100 GHz "alt-cross" spectra (cyan), and frequency combined 100 + 150 GHz spectra (black). The points have been displaced in ℓ for clarity.

results, although we use the HL method for the final results since it more accurately treats cross-spectra covariances. We test both likelihood constructions for any biases and, in simulations, we find they accurately recover known input rotation angles.

For both methods, we calculate $\chi^2 = -2 \ln \mathcal{L}$, where χ^2 is defined in Equation 6.6, below. We found the rotation angle that maximized the likelihood, and constructed 1σ error bars by finding the minimum-width 68% credible interval, assuming a uniform prior on α, for both likelihood constructions.

Gaussian Bandpower Likelihood Approximation

This method was chosen due to its computational efficiency for isolating individual spectral estimators without including corresponding auto-spectra. Here, the difference between the observed spectra and theory spectra including rotation

$$\Delta_b^{XY}(\alpha) \;=\; \hat{\mathcal{D}}_b^{XY} - \mathcal{D}_b^{XY}(\alpha), \tag{6.5}$$

is computed as a function of rotation angle, α, for each BICEP1 multipole bin, where BICEP1 reports nine bins of uniform width $\Delta\ell = 35$, with the first bin spanning $20 \leq \ell \leq 55$ and the ninth bin spanning $300 \leq \ell < 335$. Here, $\hat{\mathcal{D}}_b^{XY}$ is the measured BICEP1 XY power spectrum and $\mathcal{D}_b^{XY}(\alpha)$ is the theoretical rotated bandpower for XY for a given α. We use $\mathcal{D}_b^{XY}$ to denote binned estimates of $\mathcal{D}_\ell^{XY} = \ell(\ell+1)C_\ell^{XY}/2\pi$. Here, $XY = TB$ or EB for each frequency combination. The χ^2 statistic is then constructed using

$$\chi^2_{XY}(\alpha) = \sum_{bb'} \Delta_b^{XY}(\alpha) \mathcal{M}^{-1}_{bb'} \Delta_{b'}^{XY}(\alpha), \tag{6.6}$$

where $\mathcal{M}_{bb'}$ is the covariance between multipole bins b and b'. The covariance matrix, $\mathcal{M}$, was modeled as block-pentadiagonal, where only bandpowers separated by ± 2 bins in ℓ are used for the calculation as the covariances between bandpowers with a larger separation are not well characterized (due to the finite number of simulations, 499 in total), but the contributions from these off-diagonal elements are known to be small.

Hamimeche-Lewis Method

The Hamimeche-Lewis method is the bandpower likelihood approximation used in [6]. As before, the χ^2 statistic is constructed as in Equation 6.6 but following the procedure outlined in [6]. One crucial difference between this method and the Gaussian bandpower likelihood approximation is that XY includes all combinations of the spectra X and Y. For example, for EB, this method does not calculate the χ^2 for EB but actually the χ^2 which includes $EB + EE + BB$ – the comparison of the measured spectra to theoretical rotated spectra for EB, EE, and BB simultaneously. To calculate the χ^2 statistic for any "pure" spectral combination using this method, we calculate the χ^2 of the full spectral combination and subtract off the other spectral combinations. For example, for EB: $\chi^2_{EB} = \chi^2_{EE+BB+EB} - \chi^2_{EE} - \chi^2_{BB}$.

6.4 Rotation Angle Results

The rotation angle, α, was calculated using the HL method from the standard BICEP1 three-year frequency combined spectra. The best fit rotation angle is $\alpha = -2.77^\circ \pm 0.86^\circ$, where the quoted uncertainty is purely statistical. These spectra use our standard calibration of detector polarization angles from a dielectric sheet; systematic uncertainty on this calibration is discussed below in Section 6.5. Figure 6.4 plots the peak-normalized HL likelihood and Figure 6.5 shows the best fit rotation angle spectra plotted compared to the BICEP1 three-year data and 499 simulated ΛCDM realizations (i.e., with $\alpha = 0$).

6.4.1 Consistency Between Analysis Methods

To check that the rotation angle is not dependent on the analysis method, polarization rotation angles derived from the two analysis methods were compared. In Figure 6.6, the likelihoods calculated for TB, EB, and $TB + EB$ for the frequency combined spectra for both the HL and Gaussian bandpower likelihood approximations are overplotted. For all three available spectral estimators,

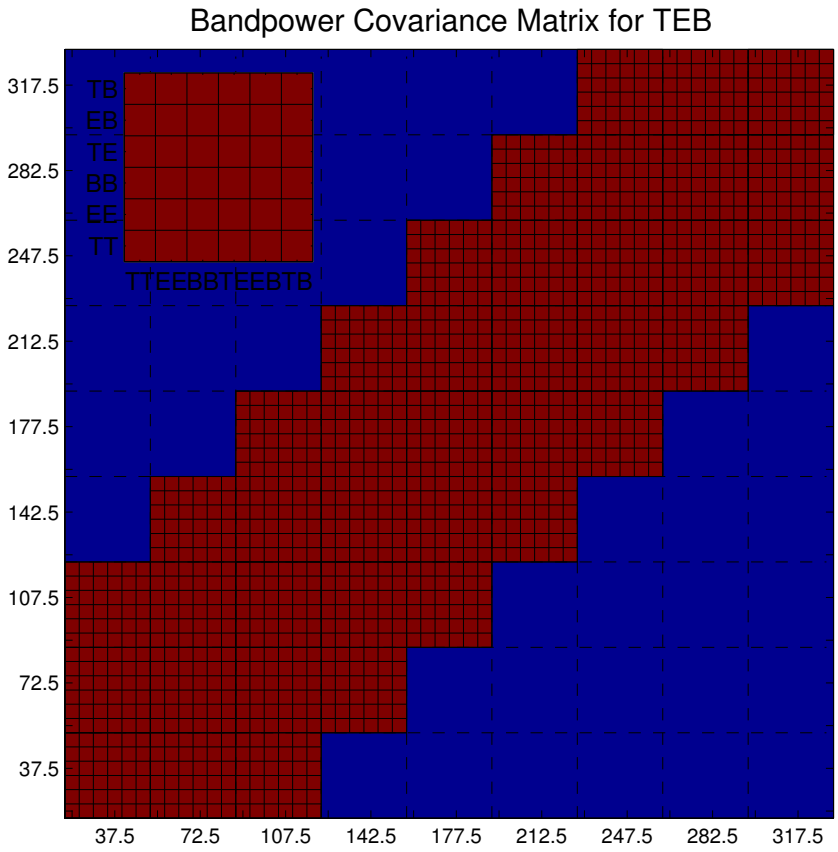

Figure 6.3: A two-color plot showing the elements of the bandpower covariance matrix used in the all-spectra HL likelihood calculation. Each 6×6 matrix represents the covariances between bandpowers b and b' for all six spectral bands: TT, EE, BB, TE, EB, and TB. The red squares are the elements used in the calculation and the blue elements are excluded. The inset shows the spectral band breakdown of each individual bandpower covariance matrix.

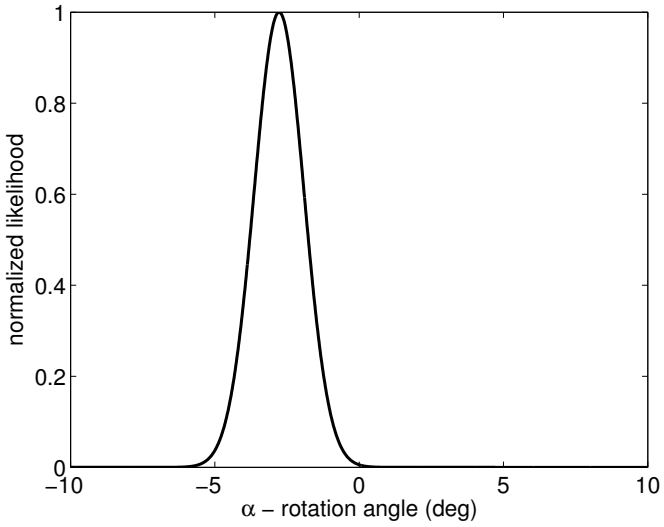

Figure 6.4: The peak-normalized Hamimeche-Lewis likelihood for the all-spectra ("TEB") rotation angle. The maximum likelihood value is -2.77° and the 68% confidence limits are ±0.86° from the peak value, corresponding to 3.22σ statistical significance.

the analysis methods agree to within 0.32σ, 0.30σ, and 0.18σ for TB, EB, and $TB + EB$, respectively.

6.4.2 Consistency Between Frequencies

For consistency, the different frequency combinations were checked to determine if they have similar rotation angles. Table 6.2 shows the calculated rotation angles from each frequency data set and for all four spectral estimators. Figure 6.7 shows the HL likelihoods for the all-spectra ("TEB") rotation angles for each data set.

Table 6.2: Maximum likelihood value and 1σ error for α. All numbers are in degrees.

Dataset	TB only	EB only	$TB + EB$	all spectra
100 GHz	$-1.79^{+3.18}_{-3.14}$	$-3.53^{+2.38}_{-2.26}$	$-2.27^{+2.06}_{-1.98}$	$-2.27^{+2.06}_{-2.02}$
150 GHz	$-4.37^{+1.92}_{-1.78}$	$-2.95^{+1.20}_{-1.18}$	$-3.13^{+1.14}_{-1.12}$	$-2.91^{+1.06}_{-1.04}$
cross	$-3.93^{+1.84}_{-1.74}$	$-2.55^{+1.68}_{-1.60}$	$-2.83^{+1.28}_{-1.24}$	$-2.67^{+1.20}_{-1.18}$
alt-cross	$-2.71^{+3.52}_{-3.74}$	$-3.25^{+2.26}_{-2.20}$	$-3.45^{+2.24}_{-2.18}$	$-3.15^{+1.96}_{-2.00}$
comb	$-3.47^{+1.66}_{-1.56}$	$-3.05^{+1.00}_{-0.96}$	$-2.99^{+0.94}_{-0.92}$	$\mathbf{-2.77^{+0.86}_{-0.86}}$

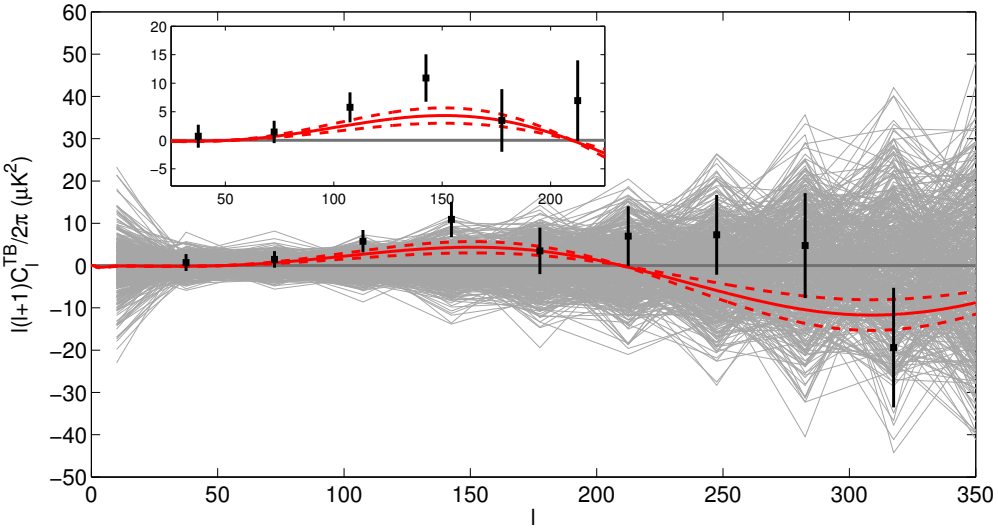

(a) TB

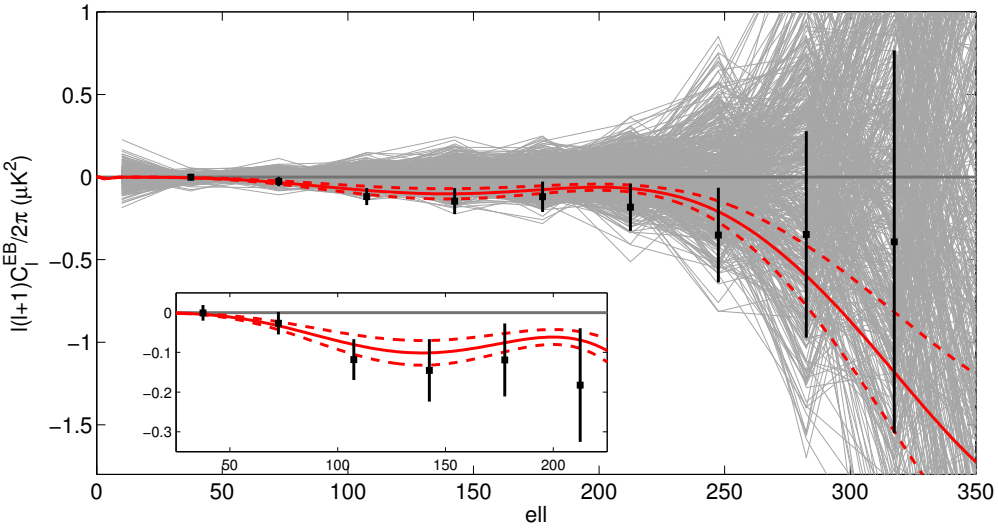

(b) EB

Figure 6.5: Frequency-combined three-year BICEP1 spectra (black points) shown with the theoretical rotated spectra from the best fit all-spectra rotation angle, $\alpha = -2.77^\circ \pm 0.86^\circ$ (red solid), the 1σ confidence limits (red dashed), and the 499 simulation realizations (gray). All simulations realization assume $\alpha = 0$.

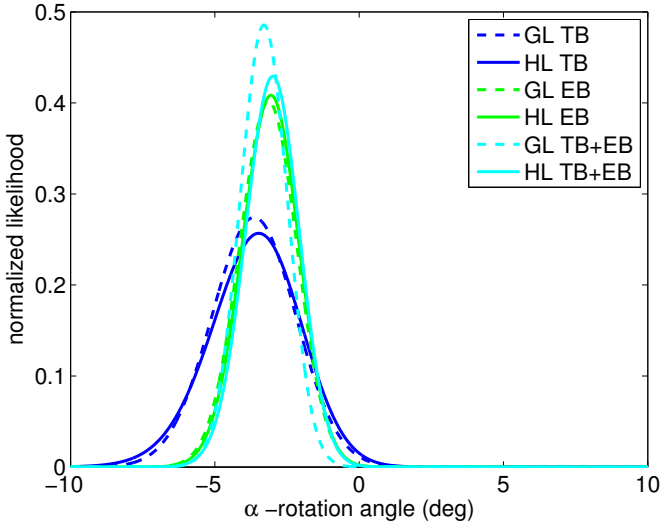

Figure 6.6: Comparison of the two likelihood methods employed for the rotation angle calculation for the frequency combined data. Likelihoods computed from the Gaussian bandpower likelihood approximation are shown as dashed lines and the Hamimeche-Lewis method likelihoods are shown as solid lines. The TB likelihood is in blue, EB is in green, and the $TB + EB$ likelihood is cyan. The likelihoods have been normalized by their integral over α.

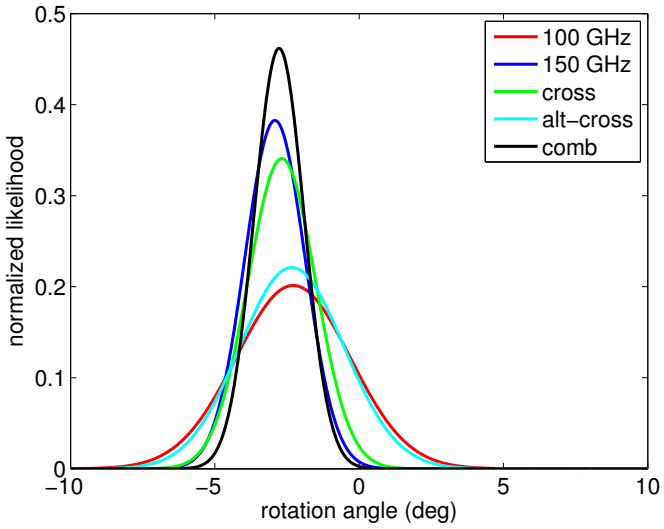

Figure 6.7: Comparison of integral-normalized Hamimeche-Lewis method likelihoods of all-spectra (TEB) rotation angles for 100 GHz auto-spectra (red), 150 GHz auto-spectra (blue), 100 $\times$ 150 GHz cross-spectra (green), 150 $\times$ 100 GHz "alt-cross" spectra (cyan), and frequency combined spectra (black).

6.4.3 Consistency with Planck Temperature Maps

The TB spectrum estimate of the polarization rotation explicitly depends on the BICEP1 measurement of temperature. To check for systematics in the TB power spectrum, we replace BICEP1 maps with Planck temperature maps [60] for both 100 and 150 GHz and find the recovered angles agree to within 0.2σ.

6.5 Impact of Instrumental Systematic Effects

BICEP1 was the first experiment designed specifically to measure the B-mode power spectrum in order to constrain the inflationary cosmological model [43]. Accordingly, the analysis of instrumental systematics focused on potential bias of the BB spectrum and the tensor-to-scalar ratio with a benchmark of $r = 0.1$ [68]. Here, we extend the analysis to include the impact of measured systematics on the TB and EB power spectra for the three-year data set.

6.5.1 Polarization Angle Calibration

An error in the detector polarization angles used for map-making is the only systematic which is completely degenerate with a rotation due to isotropic cosmic birefringence, and the only systematic capable of producing self-consistent TB and EB power spectra [77]. This calibration requirement is much more stringent when attempting to measure α than for r.

Calibrating detector angles for CMB polarimeters is very challenging. Some commonly employed methods include man-made calibrators, such as a polarizing dielectric sheets [68, 43] or polarization-selecting wire grids [67, 32], and observations of polarized astronomical sources [30, 13]. Man-made polarization calibration sources suffer from a host of challenges: they are often situated in the near-field of the telescope, they can be unstable over long timescales, and they can be cumbersome to implement and align. Astronomical sources are not visible from all observatories and even the best characterized sources have orientations measured to an accuracy of only 0.5° [5]. In addition, the brightness of both astronomical

and man-made calibration sources can overload the detectors, forcing them into a non-linear response regime [44].

BICEP1 employed several hardware calibrators to measure detector polarization angles. The primary calibration comes from a dielectric sheet calibrator (DSC), described in detail in [68], but additional calibrations were made using sources with polarizing wire grids in the near and far field. The BICEP1 beam size and observatory location prevented polarization calibration using astronomical sources.

The polarization angle measurement from the DSC was performed the most frequently and is the best studied, which is why it was chosen for results in [18, 6], as well as this work. Repeated measurements during each observing season produced polarization angles that agree with an rms error of 0.1°. However, measurements taken before and after focal plane servicing between the 2006 and 2007 observing seasons show an unexplained rotation of 1° in the polarization angles. There is also some uncertainty in translating the results of the DSC measurement to parameters appropriate for CMB analysis. The details of the polarized signal from the dielectric sheet depend on the near field response of each detector, which is not well characterized.

We also consider two alternate calibrations for the detector polarization angles, which were both described in [68] as methods to measure the cross-polar response of the detectors. The first is a modulated broadband noise source, broadcasting via a rectangular feedhorn located behind a polarizing wire grid. The source is located on a mast at a range of 200 meters. We measure the detector response as a function of angle by scanning over the source with 18 different detector orientations. The advantage of this method is that the source is in the far field of the telescope. A challenge is that the observations require the use of a flat mirror, complicating the pointing model. In addition, it takes a significant amount of time to perform scans at all 18 orientations, which makes it more difficult to maintain stable source brightness. For BICEP2, we have invested significant effort in improving polarization orientation calibrations with the far-field broadband noise source, both by developing a high-precision rotating polarized source and

improving the pointing model used for calibration analysis. These improvements were motivated by BICEP1 experience with systematic uncertainties on both the DSC and broadband source calibrations.

Another polarization angle calibrator consists of a wire grid covering a small aperture that is chopped between an ambient temperature absorber and cold sky. For calibrations, this source is installed in the near field of the telescope and the wire grid is rotated to measure detector polarization angles. The interpretation of results from this source has significant uncertainty because the small aperture probes only a small fraction of the detector near field response yet the results are extrapolated to the full beam response.

Table 6.3 lists the values of α measured from maps made using each of the polarization angle calibrations. Also shown is the result obtained if we simply assume that the detector polarization angles are as-designed. These derived α values are qualitatively consistent with the average difference in the detector polarization angles between any two calibration methods, though the details depend on how each detector is weighted in the three-year maps. Besides the global rotations between each calibration method, which contributes to the variation in α, the per-detector polarization angles show scatter of 0.6–0.9° between methods, much larger than the 0.1° consistency seen from repeated measurements using the DSC. Despite this scatter, we can observe significant structure in the pattern of polarization angles from detector to detector, which is not present in the as-designed angles.

From consideration of the 1.14° difference between alpha as derived from the DSC calibration and the mean of the three alternate calibrations, which have very different sources of systematic uncertainty, as well as the 1° shift observed in the DSC calibration results between observing seasons, we assign a calibration uncertainty of 1.3° on the overall orientation from the DSC calibration. We believe this upward revision of the 0.7° uncertainty quoted for this same calibration in [68] is warranted by the tension with the alternate calibrations. While this systematic error is larger than the 0.86° statistical error on α, we stress the fact that the polarization angle calibration is quite a bit better than what is needed to meet the

$r = 0.1$ benchmark for the primary BICEP1 science goal.

Table 6.3: Polarization rotation angles derived using different detector polarization angle calibrations: the dielectric sheet calibrator (DSC), the far-field wire grid broadband noise source, the near-field wire grid aperture source, and assuming the polarization angles are as-designed.

Calibration method	near/far-field	α (degrees)
DSC	near	-2.77
wire grid broadband source	far	-1.71
wire grid aperture source	near	-1.91
as-designed	—	-1.27

In Section 6.7, we adopt a different approach and "self-calibrate" the polarization orientations by rotating the polarization maps to minimize α. Note that the calibration uncertainty on α applies only when we use the DSC calibrated maps and attempt to measure astrophysical polarization rotation. To judge how well the self-calibration procedure can debias the B-mode map, only the statistical error is relevant.

6.5.2 Differential Beam Effects

Differential beam mismatches potentially mix E-modes and B-modes or leak intensity to either E- or B-mode polarization. Here, we investigate the impact of differential beam size, differential relative gain, differential pointing, and differential ellipticity on the derived rotation angle.

Beam systematics affect the EB spectra in a different way than TB spectra [65, 52]. As a result, the scale dependence of the beam systematic polarization will imply a different *effective* rotation angle in the TB spectrum versus the EB spectrum, for a fixed $\ell-$range.

The BICEP1 beams were measured in the lab prior to deployment using a source in the far-field (50 meters from the aperture) and each observing season during summer calibration testing. Beam maps were fit to a two dimensional elliptical gaussian model which included a beam location, width, ellipticity, and orientation of the major axis of the ellipse with respect to the polarization axes.

Differential Beam Size

Though the differential beam size effect can leak temperature to polarization, due to circular symmetry it will not break the parity of the underlying sky and thus cannot generate the parity-odd TB and EB modes [65].

Differential Relative Gain

As with differential beam size, circular symmetry is preserved by differential relative gain and thus there is no breaking of the parity of the sky which would generate TB and EB modes [65]. We ran differential gain simulations using observed values and random values drawn from a gaussian distribution with an rms of 1%. None of the simulations showed polarization rotation greater in magnitude than 0.25°.

A significant difference between the BICEP1 two-year results reported in [18] and the BICEP1 three-year power spectra is that the three-year spectra undergo relative gain deprojection which reduces B-mode contamination due to this systematic to negligible levels [6].

Differential Pointing

The effect of differential pointing is analytically calculated using the measured magnitude and direction of beam offsets with the expected amount of false BB power scaling as the square of the magnitude of the differential pointing, following the construction in [65]. The upper limit on differential pointing error was estimated to be $< 1.3\%$ of the beam size. While this was found to be the dominant beam systematic effect for the BICEP1 limit on r [6], it is clear from Figure 6.8 that differential pointing does not induce TB or EB, and has a negligible effect on the polarization rotation angle estimation. This was calculated for the "worst-case" scanning strategy and therefore provides very conservative bounds on the TB and EB produced.

Differential Ellipticity

Differential ellipticity values were derived by fitting each measured beam in a detector pair for ellipticity and then differencing those values for the two detectors in a pair. The fits were generally not repeatable when the telescope was rotated about its boresight angle, so only upper limits on differential ellipticity are quoted. The BICEP1 estimated differential ellipticity is $< 0.2\%$.

As with differential pointing, we calculate the TB and EB following the construction in [65]. As before, this is for the "worst-case" scenario, where the major axes of the ellipticities are separated by 45°. From Figure 6.8, it is clear differential ellipticity can generate TB power which has a different spectral shape than that produced by polarization rotation. In addition, the TB spectrum is inconsistent with the polarization rotation of EB.

6.5.3 Experimental Consistency Checks

To probe the susceptibility of BICEP1 data to systematic effects irrespective of origin, [18] created six null-tests or "jackknife" spectra that were used as consistency tests. These tests involve splitting the data in two halves and differencing them. The two halves are chosen to illuminate systematics since signals which are common to both data sets will cancel, and the resultant jackknife will either be consistent with noise or indicate contamination. The jackknife splits are by boresight rotation, scan direction, observing time, detector alignment, elevation coverage, and frequency, as described in [18, 6].

In the power spectrum analyses [18, 6], the jackknife maps were obtained by differencing the maps for each half whereas here we ran each jackknife half through the full analysis pipeline to produce power spectra. Unlike in the previous analyses, we did not look for consistency with zero but self-consistency between jackknife halves. We fit rotation angles for each jackknife half and difference the resultant best-fit angles to form $\Delta\alpha$. Only the frequency-combined spectra are used to improve the constraining power of these tests. We then calculate the probability to exceed (PTE) the observed $\Delta\alpha$ value by chance, given measurement uncertainties. These results are shown in Figure 6.9. If there is an instrumental systematic

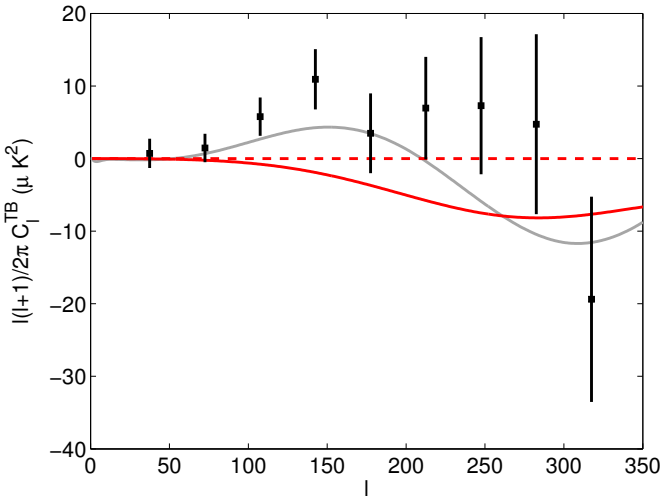

(a) TB

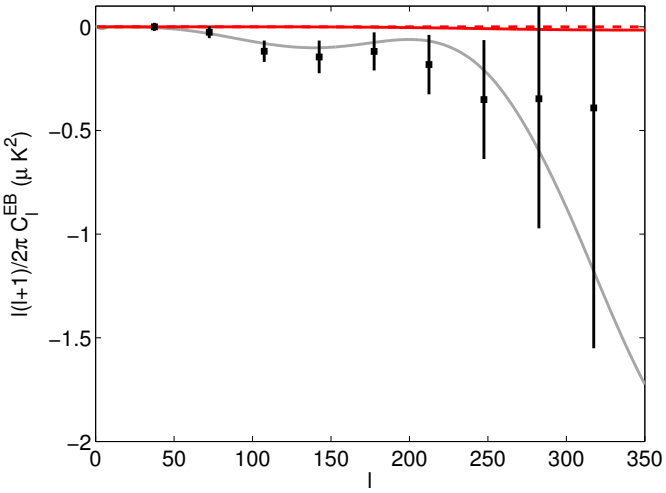

(b) EB

Figure 6.8: A plot of the effects of differential ellipticity (red solid line) and differential pointing (red dashed line) on the TB (left) and EB (right) power spectra. The gray line shows the power spectra with $\alpha = -2.77°$. The black points are the frequency-combined three-year band powers. The differential ellipticity and differential pointing are at the level of 0.2% and 1.3%, respectively, corresponding to the upper limits reported in [68]. In both cases, the systematic curves correspond to "worst-case" scenarios: the major axes of the ellipticities are separated by 45° and differential pointing assumes a poorly-chosen scan strategy[52].

contribution to a detection of α that is tested using these null tests then excess PTE values near zero will arise. The jackknife halves are considered consistent if

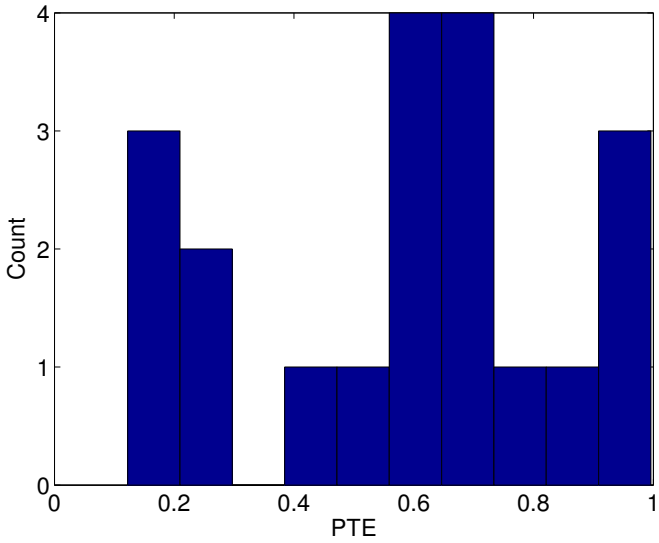

Figure 6.9: A histogram of the probability to exceed values for the measurement of $\Delta\alpha$ in each of the jackknife spectra. There are 20 spectral combinations (which are not all independent): TB, EB, $TB+EB$, and "all-spectra" estimators for the frequency-combined spectra for each of the five jackknife tests.

they meet the following three criteria: 1) fewer than 5% of the jackknives have PTE values smaller than 5%, 2) none of the PTE values are excessively small (defined as $\ll 1\%$), and 3) the PTE value from all jackknives are consistent with a uniform distribution between zero and one. Given the consistency of the jackknife PTEs with these criteria, systematics probed by these jackknifes are not the source of the observed polarization rotation angle.

6.6 Constraints on Frequency Dependent Cosmological Birefringence

This paper has focused on the assumption that polarization rotation is independent of electromagnetic frequency. However, several models feature polarization rotation that predicts a manifestly frequency-dependent rotation angle. One such birefringence model has been proposed by Contaldi, Dowker, and Philpott in [19], hereafter called the "CDP" model.

Another effect which could cause frequency dependent polarization rotation

would be Faraday rotation of CMB polarization due to the Milky Way's magnetic field.

6.6.1 Contaldi Dowker Philpott Model

In the CDP model, there are two electromagnetic frequency-dependent parameters (μ and χ) leading to the following power spectra

$$\begin{aligned}
C_\ell'^{TT} &= C_\ell^{TT} \\
C_\ell'^{TB} &= e^{-\mu} C_\ell^{TE} \sin(2\chi) \\
C_\ell'^{EB} &= \frac{1}{2} e^{-2\mu} \left(C_\ell^{EE} - C_\ell^{BB} \right) \sin(4\chi) \\
C_\ell'^{TE} &= e^{-\mu} C_\ell^{TE} \cos(2\chi) \\
C_\ell'^{EE} &= e^{-2\mu} C_\ell^{EE} \cos^2(2\chi) + e^{-2\mu} C_\ell^{BB} \sin^2(2\chi) \\
C_\ell'^{BB} &= e^{-2\mu} C_\ell^{EE} \sin^2(2\chi) + e^{-2\mu} C_\ell^{BB} \cos^2(2\chi)
\end{aligned} \tag{6.7}$$

where $\mu/\chi \sim 1/\nu$, and ν is the electromagnetic frequency (*i.e.* 100 and 150 GHz). Here, χ is a frequency-dependent rotation angle, and μ characterizes the frequency-dependent damping parameter. The frequency-independent spectra are obtained in the limit $\mu \to 0$, with χ identified with α.

As is evident from Eq. (6.7), to constrain the frequency-dependent CDP model, the TE, EE, and BB spectra must also be included in the analysis in order to break the degeneracy between χ and μ.

The results for the damping parameter and rotation angle χ are presented in Table 6.4 and Figure 6.10. The inferred μ is consistent with zero and μ/χ is not inversely proportional to ν, thus there is no compelling evidence for frequency dependent birefringence in the CDP picture.

Table 6.4: Maximum likelihood values for the damping parameter, μ, and the rotation angle, χ, along with their 1σ error bars for the CDP model.

Frequency (GHz)	μ	χ (degrees)
100	$-0.017^{+0.073}_{-0.076}$	$-2.25^{+2.02}_{-2.02}$
150	$-0.029^{+0.042}_{-0.043}$	$-2.91^{+1.02}_{-1.02}$

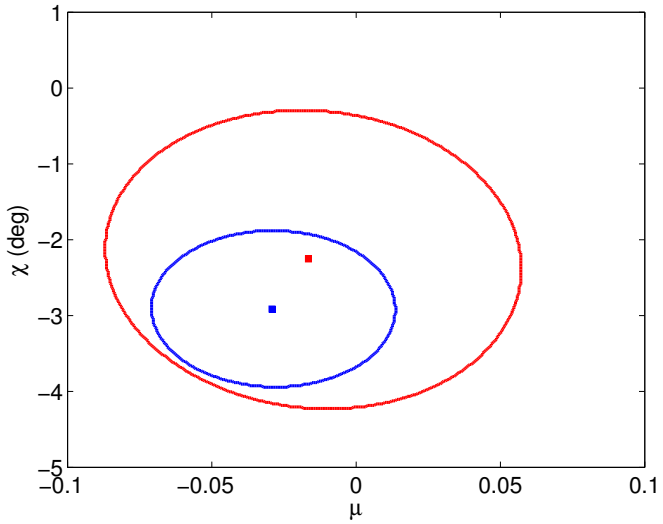

Figure 6.10: Best fit μ and χ values for the CDP model for 100 GHz (red point) and 150 GHz (blue point) from the all-spectra estimator, along with their 68% confidence interval contours (red and blue contours respectively).

6.6.2 Faraday Rotation of Galactic Magnetic Field

Faraday rotation due to the Milky Way's magnetic field predicts frequency-dependent polarization rotation proportional to the inverse of the frequency squared [21]. Scaling the 150 GHz "all-spectra" estimator α by $(100/150)^{-2}$, we would expect to see polarization rotation of the 100 GHz spectra consistent with an $\alpha = -6.55^{+2.34}_{-2.39}$ degrees, whereas our 100 GHz "all-spectra" estimator results in a polarization rotation of $\alpha = -2.27^{+2.06}_{-2.02}$, corresponding to a 1.37σ discrepancy. While there is some tension between the predicted α and the measured α, Faraday rotation cannot be ruled out as the cause of the rotation.

6.7 Self-Calibrated Upper Limit on Tensor to Scalar Ratio

If the polarization rotation is systematic in nature, the derived rotation angle can be used to calibrate the detector polarization orientations [44]. The three-year "all-spectra" rotation angles were added to the polarization orientations

treating the frequency bands as independent, i.e., only the 100 GHz (150 GHz) derived rotation angle was added to the 100 GHz (150 GHz) detectors. These "self-calibrated" polarization orientation angles were propagated through the power spectrum analysis pipeline [6]. The self-calibrated power spectra were analyzed for residual polarization rotation which yielded a rotation angle $\alpha = +0.01^\circ \pm 0.86^\circ$ from the frequency-combined all-spectra estimator, consistent with zero, as expected.

Any polarization rotation, regardless of cosmic or systematic origin, will positively bias r since E-mode power will be leaked into the B-mode spectrum (Equation 6.4). There is also a reduction to the B-mode power spectrum due to B-modes leaking to E-modes, however since the E-modes are significantly larger than the B-modes, the net result is a positive bias on the B-mode power spectrum. From the self-calibrated three-year power spectra, following the procedure in [6], we find the upper limit on the tensor-to-scalar ratio reduces from $r < 0.70$ to $r < 0.65$ at 95% confidence. From simulations, we find that the bias on r from self-calibration with no underlying polarization rotation is less that 0.01.

6.8 Conclusion

The BICEP1 three-year data, when analyzed using detector polarization orientations from our standard dielectric sheet calibrator, show non-vanishing TB and EB spectra consistent with an overall polarization rotation of $-2.77^\circ \pm 0.86^\circ$ at 3.22σ significance. The significance for non-zero rotation of astrophysical origin is only 1.78σ, given the 1.3° systematic uncertainty on our orientation calibration which adds in quadrature. This result passes experimental consistency tests which probe for systematic differences of polarization rotation in various subsets of data. We rule out beam systematics as significant, and identify polarization orientation miscalibration as the primary concern among instrumental systematics. Isotropic cosmic birefringence can not be excluded, though it is degenerate with a polarization miscalibration. The data show no compelling evidence for frequency-dependent isotropic cosmic birefringence models. An alternate use of

the measurements described here is to self-calibration the detector polarization orientations, at the expense of losing constraining power on isotropic cosmological birefringence [44]. Self-calibrating the BICEP1 three-year data reduces the upper limit on the tensor-to-scalar ratio from $r < 0.70$ to $r < 0.65$ at 95% confidence.

Future CMB polarimeters with improved polarization calibration methods will be needed to break the degeneracy between polarization rotation and detector polarization orientation uncertainty. In addition to the CMB, complimentary astronomical probes such as the polarization orientation of radio galaxies and quasars [24, 40] can help constrain cosmological birefringence. However, these objects can only constrain cosmic birefringence over a limited range of redshifts and only along particular lines-of-sight, whereas CMB polarization can be used to constrain cosmic birefringence over the entire sky and is sensitive to effects accrued over the history of the entire Universe. Polarization angles calibrated with current man-made or astronomical sources are accurate enough for current generation B-mode measurements, but are insufficiently characterized for cosmic birefringence searches. Based on BICEP1 experiences with systematic uncertainties on polarization orientation calibration reported in this paper, improved far-field calibrators have been developed for BICEP2 and other future experiments. The revolutionary discovery potential of a detection of cosmic birefringence motivates the development of more accurate hardware calibrators and further investigation of astronomical sources, to achieve a precision of $\ll 0.5^\circ$. Ultimately, a combination of precisely understood man-made and astronomical sources will allow for powerful constraints on parity violation which will come concomitantly with bounds on the physics of inflation.

This chapter, in part, is a reprint of material as it appears in Physical Review D 89, 062006, 2014. J. P. Kaufman, N. J. Miller, M. Shimon, D. Barkats, C. Bischoff, I. Buder, B. G. Keating, J. M. Kovac, P. A. R. Ade, R. Aikin, J. O. Battle, E. M. Bierman, J. J. Bock, H. C. Chiang, C. D. Dowell, L. Duband, J. Filippini, E. F. Hivon, W. L. Holzapfel, V. V. Hristov, W. C. Jones, S. S. Kernasovskiy, C. L. Kuo, E. M. Leitch, P. V. Mason, T. Matsumura, H. T. Nguyen, N. Ponthieu, C. Pryke, S. Richter, G. Rocha, C. Sheehy, M. Su, Y. D. Takahashi, J. E. Tolan, and K. W. Yoon. American Physical Society, 2014.

Chapter 7

Detection of degree-scale B-mode polarization with BICEP2

The goal of BICEP1 and BICEP2 was to detect B-mode polarization around the degree angular scale, where the Inflationary signal is expected to peak. This was lovingly considering a "wild-goose chase" by our principal investigator, Andrew Lange. With three-years of BICEP1 data, we chipped away at these B-modes, concluding that the amplitude must be below $r < 0.65$ with 95% confidence [42]. This result provided the tightest constraints ever made at that time directly from measurements of the B-mode polarization spectrum.

With BICEP2, we kept the strategy the same but upgraded several key technologies. These upgrades provided us with a factor of ten greater mapping speed over BICEP1. I can say honestly that even with these upgrades, few of us (if any) expected to see anything at the low angular scales. After three-years of observations with BICEP2, we have detected non-zero B-mode polarization at the degree-scale inconsistent with ΛCDM (including lensing) to greater than 5σ.

In this chapter, I will present details of the data set used to make these measurements; I will present the maps and power spectrum results; discuss some of the internal consistency checks we performed; investigate actual and potential contamination to the B-mode signal from our instrument and our sources other than the CMB; and finally, I will provide a Cosmological interpretation of our results.

Figure 7.1: The Dark Sector Laboratory which housed BICEP1 and BICEP2. The South Pole telescope can be seen to the left. The orange flag marks the location of an IceCube detector string.

7.1 Data set

BICEP2 was installed in the Dark Sector Laboratory in late 2009 and did not break vacuum or warm up until December of 2012. This allowed us to observe the sky continuously for three years, breaking only during the "warm" summer months. This can be seen in Figure 7.2. During this time, it was the duty of graduate students like myself to perform characterization, calibration, and optimization measurements at a furious pace, often foregoing meals, sleep, and (not by choice) personal hygiene.

We use the full three-year data set for analysis which consists of ≈ 590 days of observations, or over 1.8 million scans in azimuth.

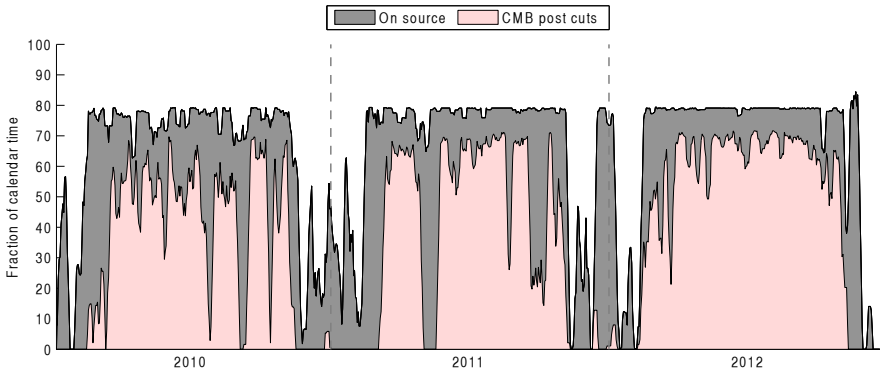

Figure 7.2: Live time of BICEP2 and the fraction of data used for the final analysis. The division between summer calibrations measurements and winter CMB measurements is clearly shown. [10]

Data selection

To make sure that we only include data taken when our telescope is working appropriately, we employ a series of data quality checks sensitive to particular instrument phenomenologies. We break our data selection procedure into a two step process so that we can investigate cut thresholds and track these phenomenologies without requiring significant re-analysis of data. The first cuts remove data which are definitively useless during the computationally intensive data reduction stage, prior to map-making. Examples of these are glitches (like cosmic ray hits), flux jumps in the SQUID readout[1], and any issues with synchronization in the data acquisition system. Over 90% of the data pass this first round of data cuts. These are applied at the half-scan granularity, defined as one throw in azimuth.

The second-round cut statistics are accumulated during the binning of the timestreams into pairmaps, another computationally intensive step. This allows us to vary cut parameters as we co-add the pairmaps into a full CMB map without having to re-create pairmaps for each new cut framework.

A list of data cuts we apply is found in Table **??**. Here, the amount of time the instrument as a whole spent on-source used for the CMB analysis is denoted as

[1]The units of the detector readout are arbitrary but dependent on the lock-point of the SQUID amplifier. A flux jump changes this lock point which appears as a step in the detector's timestream.

Table 7.1: BICEP2 data cuts, as shown in [9].

Cut parameter	Total time [10^6 s]	Integration [10^9 det $\cdot$ s]	Fraction cut [%]
Before cuts	36.5	14.8	–
Channel cuts	36.5	13.2	10.9
Synchronization	35.3	12.7	3.1
Deglitching	33.6	10.7	13.8
Per-scan noise	33.6	10.7	$< 0.01\%$
Passing channels	33.3	10.7	0.22
Manual cut	33.0	10.6	0.43
Elevation nod	31.0	9.2	9.5
Fractional resistance	31.0	9.2	0.16
Skewness	31.0	9.1	0.41
Timestream variance	30.9	9.0	0.52
Correlated noise	30.9	9.0	$< 0.01\%$
Noise stationarity	30.7	8.9	0.64
FPU temperature	30.6	8.9	0.20
Passing data	27.6	8.6	1.7

"Total time". "Integration" is the collective time including only detectors which pass the cuts. Some cuts will affect a few channels out of a scan whereas some will cut a chunk of time from the whole scan. The numbers in each row reflect the amount of data left over after the cut in the last column has been applied. The cuts are:

- *Channel cut* - Essentially a detector yield cut, where detector pairs with wildly discrepant beam-shapes or faulty readout are removed. The channel cut affects $\sim$ 10.9% of the detectors. Note that this reduces the per-detector "integration" time, it leaves the total time unchanged.

- *Synchronization cut* - Removes a small amount of data limited to a few isolated instances where the time-stamps from the detector data could not be matched to the telescope pointing data.

- *Deglitching cut* - Removes data with sharp, often discontinuous jumps. Events that trigger these are the aforementioned flux jumps and cosmic ray hits. This cut would also remove data from nearest-neighbor detectors which could suffer from crosstalk. Due to this precaution, it was the most significant cut of the data. Detectors with significant number of glitches were removed from the entire scan-set.

- *Per-scan noise* - Tracks the variance of the detectors during a scan. This would cut detectors which became unstable within a scan.

- *Passing channels* - Scans in which $< 70\%$ of detectors in a multiplexing column passed all other cuts were removed. This prevented misbehaving detectors from interacting with "good" detectors via crosstalk.

- *Manual cut* - There was a short period of time in 2010 (less than one full day) when we had optimized our multiplexing rate but not yet changed the filtering and downsampling. Although these data are likely fine to use, we cut them as the telescope was not operating nominally during this time.

- *Elevation nod* - The elevation nods ("elnods") that bracket each scanset are used to calculate the relative gain for each detector. If the gain changes by more than 30% between elnods for a given detector then it is cut. Similarly, if the ratio of the A/B detectors in a pair changes by greater than 10%, the pair is cut. Detectors are also cut if their elnods do not fit to the atmospheric profile. These dramatic gain changes or failures to fit are almost entirely due to weather. Overcast skies or blowing snow greatly change the detector responses during an elnod, causing an elevation nod cut failure.

- *Fractional resistance* - Since our TES bolometers operate by being biased in their superconducting transition, we want to catch any detectors which fall out of this transition to become superconducting or normal. Any detector whose fractional resistance, $R_{\rm TES}/R_{\rm normal}$, is either less than 10 % or greater than 95% was cut. Like the elevation nod cut, this is sensitive to bad weather as clouds increase the atmospheric loading, which can push detectors into their normal resistance regime.

- *Skewness, timestream variance, correlated noise, and noise stationarity* - These four parameters were compared to a standard noise model and data were cut for detectors which are wildly discrepant. This is also a probe for bad weather, as well as temporary readout system issues.

- *FPU temperature* - Any data in which the focal plane temperature rose to greater than 300 mK, or for which the standard deviation of the focal plane temperature was greater than 50 μK were cut. This removed a small fraction of data in which the focal plane temperature had not settled immediately following a cycle of the refrigerator.

- *Passing data* - Data where fewer than 50% of the detectors pass all the other cuts were removed by this final cut. This probed periods

where no one issue caused the data to fail a cut but the overall data demonstrated that the telescope was not behaving properly.

After applying all data selection cuts, the total pass-fraction of data was 75.6% of total on-source time, or 58.1% including cuts of individual detectors.

7.2 Maps

After the initial low-level analysis, including deconvolution of detector transfer functions and relative gain corrections, the data were passed through the first round of data selection cuts. For each detector pair, the pair-sum and pair-difference (which corresponded to temperature and polarization maps, respectively) were calculated, third-order polynomial filtered, and cleaned of any azimuth-fixed pickup. Here, left-moving and right-moving scans in azimuth were treated independently. At this stage, the deprojection timestreams were created and second round data selection cuts were accumulated.

Next, pair sum and difference data were accumulated into right ascension (RA) and declination (Dec) maps in a per-phase granularity, and weights were calculated separately for the pair-sum and pair-difference maps as the inverse of the variance. To generate temperature and polarization maps, we start with the simplified detector timestreams, following [39, 18]:

$$d_{nj} = g_{nj}\left[T(\mathbf{p}_j) + \gamma_n(Q(\mathbf{p}_j)\cos 2\psi_{nj} + U(\mathbf{p}_j)\sin 2\psi_{nj})\right], \tag{7.1}$$

where g is the gain, $\gamma \equiv (1-\epsilon)/(1+\epsilon)$ is the polarization efficiency correction (ϵ is the polarization efficiency – a perfect detector would have $\epsilon = 0$), and ψ is the detector polarization orientation on the sky (i.e., including boresight orientation). n spans the number of detectors and j represents the j^{th} time-sample. $\mathbf{p}_j$ is a given map pixel observed at time j. We then construct pair-sum and pair-difference timestreams as

$$d^{\pm}_{nj} = \frac{1}{2}\left(\frac{d_{Aj}}{g_A} \pm \frac{d_{Bj}}{g_B}\right), \tag{7.2}$$

where A and B denote the orthogonal polarized detectors in a pair.

To construct temperature maps, we use the pair sum:

$$\sum_{n}^{\text{no. pairs}} \sum_{j\in\mathbf{p}} w^{+}_{nj} d^{+}_{nj} \Big/ \sum_{n}^{\text{no. pairs}} \sum_{j\in\mathbf{p}} w^{+}_{nj} \propto T(\mathbf{p}), \tag{7.3}$$

where w^{+} are the weights of the pair-sum data. For stokes Q and U maps, we construct

$$\sum_{n}^{\text{no. pairs}} \sum_{j\in\mathbf{p}} w^{-}_{nj} \begin{pmatrix} d^{-}_{nj}\alpha_{nj} \\ d^{-}_{nj}\beta_{nj} \end{pmatrix} = \frac{1}{2} \sum_{n}^{\text{no. pairs}} \sum_{j\in\mathbf{p}} w^{-}_{nj} \begin{pmatrix} \alpha^{2}_{nj} & \alpha_{nj}\beta_{nj} \\ \alpha_{nj}\beta_{nj} & \beta^{2}_{nj} \end{pmatrix} \begin{pmatrix} Q(\mathbf{p}) \\ U(\mathbf{p}) \end{pmatrix}. \tag{7.4}$$

Similar to before, w^{-} are the weights of the pair-difference data. Here, we've introduced the orientation angle coefficients, α and β, which we define as

$$\alpha_{nj} = \gamma_{n_A} \cos 2\psi_{n_A j} - \gamma_{n_B} \cos 2\psi + n_B j \tag{7.5}$$

$$\beta_{nj} = \gamma_{n_A} \sin 2\psi_{n_A j} - \gamma_{n_B} \sin 2\psi + n_B j. \tag{7.6}$$

For a given boresight orientation, the determinant of the 2×2 matrix in Equation 7.4 is zero. Thus we cannot invert the equation to get stokes Q and U with only one boresight orientation. Although I've stated previously that we used boresight angles separated by 45° for complete Q and U coverage, this is the mathematical reason why.

Polarization orientation and efficiencies are derived from dielectric sheet measurements, including measurements I had taken. We found the polarization efficiency to be very good, at around 99% [9].

At this stage in the pipeline, we applied the second-round data selection cuts. After the cuts were applied, we accumulated the per-detector, per-scanset pairmaps into per-detector per-phase maps. A phase consisted of ten scansets, which comprised $\sim$ 10 hours of data. Next, the deprojection procedure, as described in Chapter 4, was applied to the data. These per-phase per-pair maps were accumulated into the full temperature and polarization maps, as well as many subset maps which were used to probe systematic contamination. The final step in the map-making pipeline is the application of an absolute calibration to get the maps into units of CMB temperature[2]. To calculate this absolute calibration,

[2]At this stage, maps are in units of "airmass" from the relative gain correction off the atmosphere from elevation nods.

we cross-correlated our maps with existing high signal-to-noise CMB temperature maps from WMAP 9-year [8] and Planck [59, 61]:

$$g_i^{\rm abs} = \frac{\sum_{\ell\in\{\ell_i\}}\langle a_{\ell m}^{\rm ref} a_{\ell m}^{\rm B2}\rangle}{\sum_{\ell\in\{\ell_i\}}\langle a_{\ell m}^{\rm ref} a_{\ell m}^{\rm cal}\rangle}, \tag{7.7}$$

where i represents the $i^{\rm th}$ multipole bin.

We performed this calibration with WMAP V-band and W-band as "ref" and "cal," and with Planck 100 GHz and 143 GHz as "ref" and "cal." Each map was re-observed to apply the same filtering and beam smoothing as BICEP2.The final gain value was the average of these two results.

The three-year BICEP2 temperature and Stokes Q and U maps are shown in Figure 7.3, along with the first half of the data minus the second to show the noise level. We can visually see that the temperature and polarization maps are signal-dominated.

From the Q and U maps, we can construct E and B maps[3], which are shown in Figure 7.4. These are shown with simulated lensed-ΛCDM maps. From this, we see that BICEP2 has detected B-mode polarization over the standard lensed-ΛCDM expectation.

The effective area of the maps is $\sim$ 380 square-degrees. The polarization maps have a map-depth of 87.2 nK in square degree pixels over this effective area [9].

7.3 Power spectra

Before computing the power spectra of the maps, matrix purification to remove the $E \rightarrow B$ leakage was applied, as described in Chapter 4. After this step, the power spectrum estimation is relatively simple: we anodized the temperature and polarization maps by the inverse of their noise variance maps and took the 2-D Fourier transform. From this we constructed the E and B Fourier modes from the Q and U modes. We then correlated these T, E, and B modes by

[3]This is done by calculating the Fourier modes of the Q and U maps and combining these to get the E and B Fourier modes. These are then inverse Fourier transformed to get the E and B maps. Matrix purification must also be done.

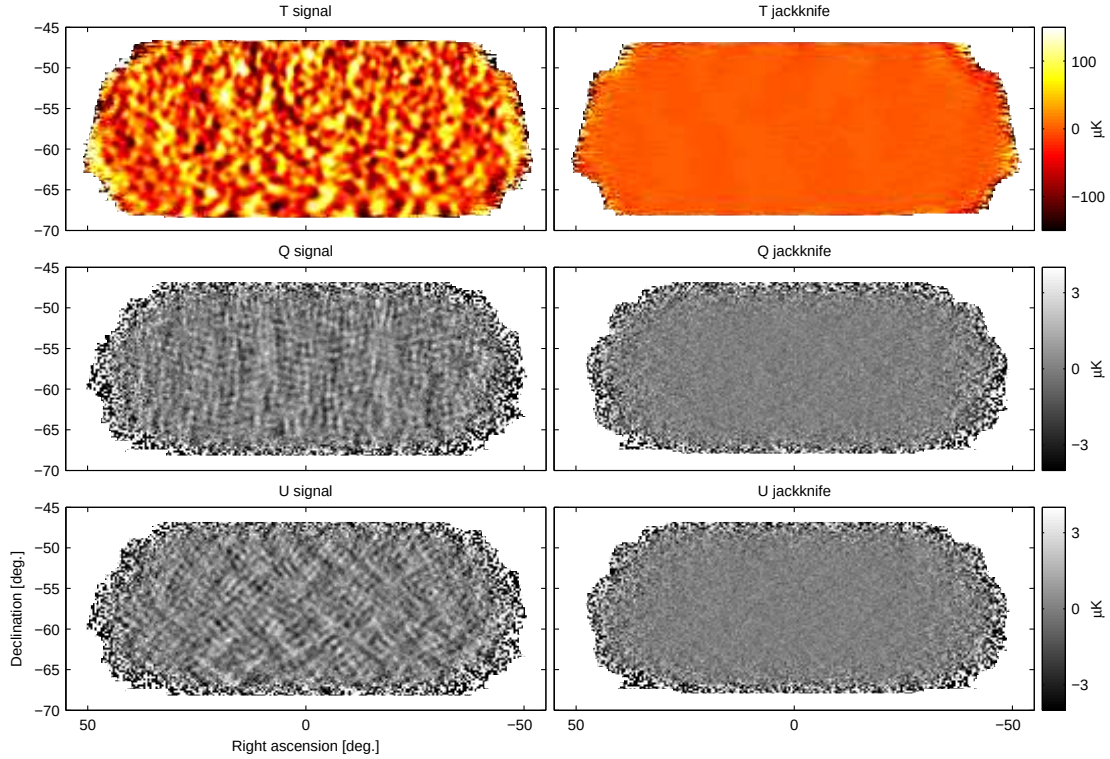

Figure 7.3: *Left:* Three-year temperature and Stokes Q and U maps [10]. *Right:* First half of the data minus the second half of the data "jackknife" which demonstrates the noise level. We can see structure in temperature and polarization with very high signal-to-noise. The striping in the polarization maps is consistent with an E-mode-like pattern dominating the sky.

multiplying by the complex conjugate of second 2-D Fourier transform to construct TT, TE, EE, BB, TB, and EB. Finally, we binned these into annuli in 2-D Fourier space and averaged over these bins to generate 1-D power spectra. As in [18] and [6], we use nine bins with $\Delta\ell \approx 35$ from $20 < \ell < 340$.

Since our experiment is not completely free of noise, auto-spectra suffer from a noise bias on the observed power spectrum. To de-bias this noise, we subtract the mean of the 500 noise pseudo-simulation realizations. These noise simulations are constructed by co-adding real pairmaps but randomly flipping the sign such that "positive" and "negative" maps have equal weight.

The telescope's beam and the filtering applied (including deprojection) apply some amount of suppression at each multipole bin. We can determine this

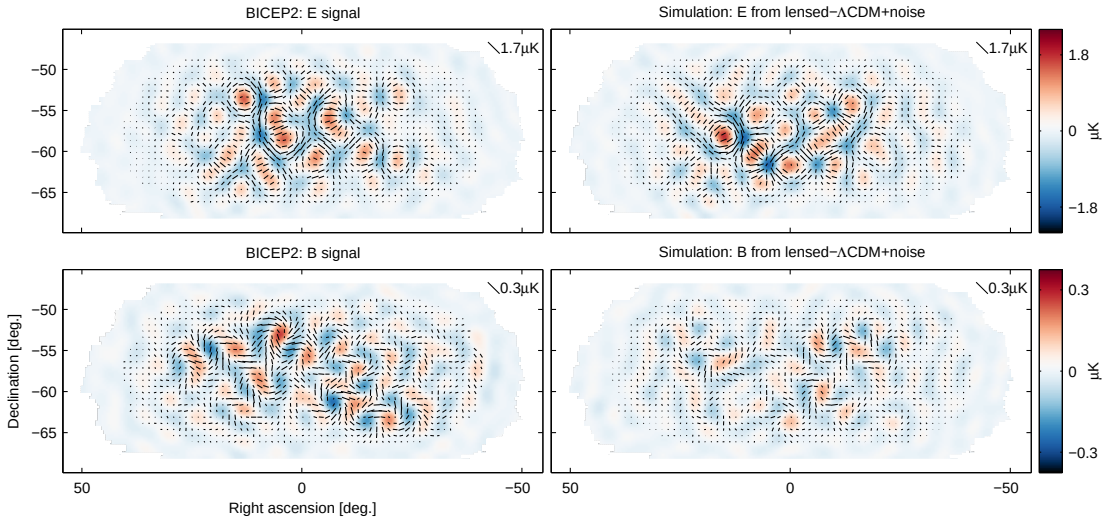

Figure 7.4: *Left:* E and B maps from three-years of BICEP2 data. *Right:* Simulated E and B maps of polarization from lensed-ΛCDM including instrument noise. We can see the characteristic B-mode "swirl" pattern just to the top-left of center in the real B-mode map [10].

suppression by comparing many simulated data realization, which have been run through the analysis pipeline, to theoretical input spectra. To correct for this suppression, we calculate the "band-power window function" (BPWF), similar to the construction in [46]. The integral of the BPWF is the amount by which the bandpowers have been suppressed, thus we can correct for this suppression in the final power spectra.

These resultant power spectra for TT, TE, EE, BB, TB, and EB are shown in Figure 7.5. Also shown are the temporal-split jackknifes for the spectra. These are constructed by differencing the first half and the second half of the three-year data. We can see that all the spectra except the BB spectrum fit to the lensed-ΛCDM model very well. In the B-mode auto-spectrum, we see an excess of power at low-ℓ over lensed-ΛCDM discrepant to 5.3σ[4].

[4]Although there are two data points at $\ell > 200$ which are discrepant with lensing, they do not provide much constraining power. If we only use the first five bandpowers, the significance of the detection reduces slightly to 5.2σ.

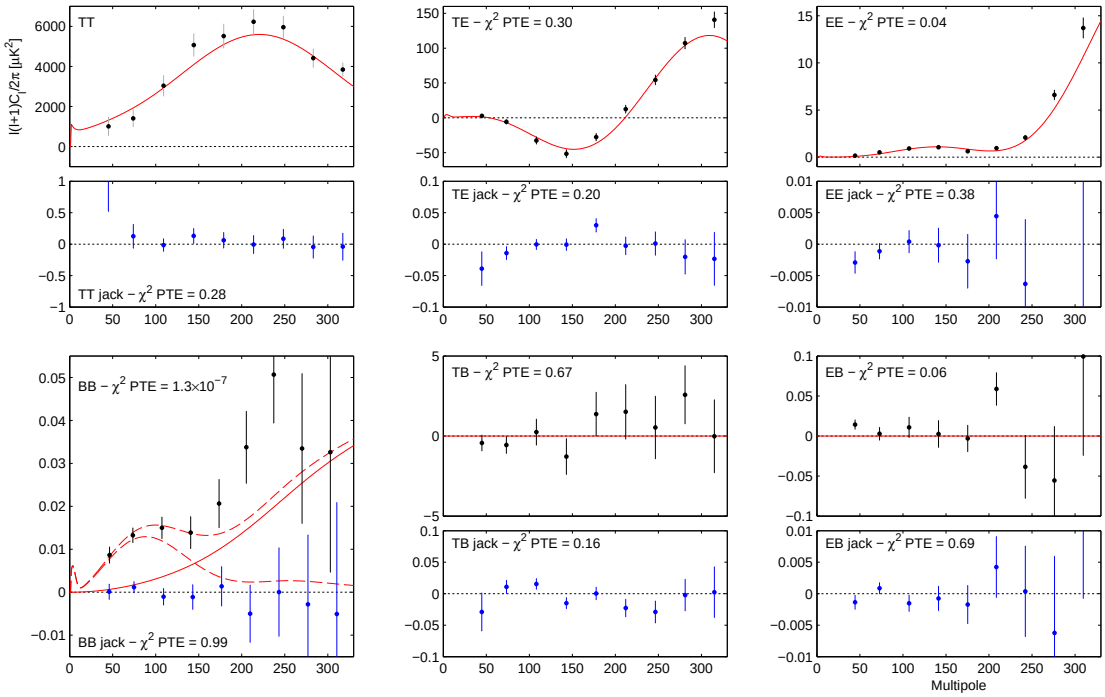

Figure 7.5: TT, TE, EE, BB, TB, and EB power spectra plots [10]. The BICEP2 data are shown as black points, the temporal-split jackknifes are shown in blue points, theoretical lensed-ΛCDM spectra from current best constraints are shown as red solid lines. In the BB plot, the red dashed lines are $r = 0.2$ with and without lensing. Also shown is the probability to exceed (PTE) the observed value of a simple χ^2 statistic.

7.4 Consistency tests

To prove that the signal we see is real, and not some systematic contribution, we split the data into two equal halves and difference them. We difference in map-space and then compute the power spectrum. Any real signal which is correlated between the two data halves will cancel upon differencing, leaving any uncorrelated noise. If one half of the data is subject to a signal that is not present in the other half, this will remain after subtraction showing a contamination in the data. We call this procedure a "jackknife." The division of data is chosen to probe for specific systematic effects. We used a set of fourteen jackknifes to scrutinize our data. They are:

- *Boresight orientation (Deck)* - BICEP2 observed at two sets of complete Q/U coverage boresight orientations (deck angles), $68° + 113°$

and 248°+293°. Here, we compare the maps made for each pair of deck angles. Differential pointing of the two detectors in a pair will average down in the usual combination of these two deck angle pairs. Differencing these will amplify differential pointing contamination thus this jackknife is extremely sensitive to detector pair differential pointing.

- *Scan direction* - Here we difference the maps made from left-moving and right-moving scans in azimuth. This is sensitive to systematic effects on short time-scales such as detector transfer functions. It is also sensitive to any differential scan-synchronous effects and the scan turnarounds.

- *Temporal split* - We difference the first and second halves of the data. The half-way point is determined such that the two halves have equal weights. This is sensitive to any long-term changes in the instrument.

- *Tile* - Differences the combination of detector tiles 1+3 and 2+4. This probes any differences in the detectors across the tiles.

- *Azimuth* - Here, the observed region is broken into two halves in azimuth. This probes any ground-fixed origin of the signal.

- *Mux column* - Even and odd numbered multiplexing columns are differenced. This is sensitive to crosstalk effects due to the readout.

- *Alt-Deck* - Similar to the Deck jackknife, we combine two pairs of boresight orientations with complete Q/U coverage. Here, we difference deck angles $68° + 293°$ and $113° + 248°$. As before, this is particularly sensitive to differential pointing.

- *Mux Row* - We split the data according to multiplexing row: columns 0-16 vs 17-33. This is sensitive to crosstalk between detectors due to the readout electronics.

- *Tile/Deck* - Tiles 1 and 2, and 3 and 4 are rotated 180° with respect to each-other on the focal plane. Because of this, when we rotate 180° in boresight, the "top" tiles are always facing up and the "bottom" tiles are always facing down. To probe for any tile-fixed effects, we difference the combination of Tiles 1+2 at deck $68° + 113°$ and Tiles 3+4 at deck $248° + 293°$ with the combination of Tiles 3+4 at deck $68° + 113°$ and Tiles 1+2 at deck $248° + 293°$.

- *Focal plane inner/outer* - Inner half of the detectors vs outer half. This probes for any systematic effects correlated with radial position on the focal plane, e.g. interactions of the detector beams with the optics.

- *Tile top/bottom* - We difference maps made from detectors in the top of the tiles and detectors in the bottom of the tiles. "Top" and "bottom" are designed with respect to the fabricated tiles, thus the top and bottom detectors for Tiles 1+2 and 3+4 are shifted 180° from each-other in focal plane coordinates. This probes for any tile-fixed effects that depend on the detector location.

- *Tile inner/outer* - Similar to the focal plane inner/outer jackknife, except inner and outer and defined for each individual tile. As with the previous jackknife, this probes for any tile-fixed effects that depend on the detector location.

- *Moon* - The appropriately named "moon" jackknife differences maps made when the moon is above the horizon vs when the moon is below the horizon. This probes for any contamination from the moon, e.g. moon men firing polarized laser beams at our telescope.

- *A/B offset best/worst* - Here the detector pairs are divided in halves according to their differential pointing. The pairs with the lowest differential pointing offset are compared with the pairs with the largest differential pointing offset.

To quantify these consistency checks, we compare each jackknife to the expected residual[5] from lensed-ΛCDM+noise simulations. We use two metrics for defining the consistency of each jackknife test. We calculated these metrics over all nine bandpowers and just the first five, where the Inflationary signal is expected to be strongest.

The first metric is a standard χ^2 statistic,

$$\chi^2 = (\mathbf{d} - \langle \mathbf{m} \rangle)^{\mathrm{T}} \, \mathbf{D}^{-1} \, (\mathbf{d} - \langle \mathbf{m} \rangle) \, . \tag{7.8}$$

Here, $\mathbf{d}$ is the vector of BICEP2 bandpowers for a given jackknife, $\langle \mathbf{m} \rangle$ is the mean of the jackknife bandpowers over the 500 realizations of lensed-ΛCDM+noise simulations, and $\mathbf{D}$ is the bandpower covariance matrix which is calculated from these simulations. We also compute this χ^2 for each realization of the simulations so we can calculate the probability to exceed (PTE) for the real data jackknife from the distribution of simulations.

[5] Although usually zero, differences in sky coverage and filtering effects can create a non-zero expectation value for the residual.

The second metric is a *chi* statistic, where we calculate the sum of the normalized deviations. This probes for data that are consistently higher or consistently lower than the expectation values. This statistic is defined as

$$\chi = \sum_i \frac{(d_i - \langle m_i \rangle)}{\sigma_{m_i}}. \tag{7.9}$$

Similar to the χ^2 statistic, here, d_i is the BICEP2 real data jackknife bandpowers, $\langle m_i \rangle$ is the average bandpowers over the simulations, and σ_{m_i} is the standard deviation over the simulations. As with the previous statistic, we also calculate χ for each individual simulation realization so we can calculate the PTE for the real data from the distribution of the simulations.

The PTE values from both of these metrics for all fourteen jackknife combinations computed for all nine and the first five bandpowers are shown in Table 7.2. Although we calculate PTE values for TT, TE, and TB, following the convention of [18, 6], we only show PTE values for EE, EB, and BB. Histograms of the PTE values are shown in Figure 7.6, demonstrating that they adhere to a uniform distribution.

Though there are seven very low PTE values (PTE $< 1\%$), six are from EE. This is due to the extremely high signal-to-noise of the EE measurement, thus even small calibration uncertainties will lead to large differences in the jackknife map. This leaves one BB jackknife with a low PTE value out of 112 $EE + EB$ jackknife combinations, well within the number expected from a uniform distribution.

7.5 Instrumental contamination

To detect the faint B-mode polarization of the CMB, we must make sure our instrument does not induce spurious polarization which could contaminate the signal. We classify these types of systematic contamination as "beam" from the pair differences of the six-parameter Gaussian beam model, and "other" for contributions from anything outside of this six-parameter model.

Table 7.2: Probability to exceed (PTE) values from the χ^2 and χ metrics for all fourteen jackknife tests. These metrics were computed for all nine BICEP2 bandpowers and the first five, where the Inflationary signal is expected to peak [10].

Jackknife	Bandpowers 1–5 χ^2	Bandpowers 1–9 χ^2	Bandpowers 1–5 χ	Bandpowers 1–9 χ
Deck jackknife				
EE	0.046	0.030	0.164	0.299
BB	0.774	0.329	0.240	0.082
EB	0.337	0.643	0.204	0.267
Scan Dir jackknife				
EE	0.483	0.762	0.978	0.938
BB	0.531	0.573	0.896	0.551
EB	0.898	0.806	0.725	0.890
Temporal Split jackknife				
EE	0.541	0.377	0.916	0.938
BB	0.902	0.992	0.449	0.585
EB	0.477	0.689	0.856	0.615
Tile jackknife				
EE	0.004	0.010	0.000	0.002
BB	0.794	0.752	0.565	0.331
EB	0.172	0.419	0.962	0.790
Azimuth jackknife				
EE	0.673	0.409	0.126	0.339
BB	0.591	0.739	0.842	0.944
EB	0.529	0.577	0.840	0.659
Mux Col jackknife				
EE	0.812	0.587	0.196	0.204
BB	0.826	0.972	0.293	0.283
EB	0.866	0.968	0.876	0.697
Alt Deck jackknife				
EE	0.004	0.004	0.070	0.236
BB	0.397	0.176	0.381	0.086
EB	0.150	0.060	0.170	0.291
Mux Row jackknife				
EE	0.052	0.178	0.653	0.739
BB	0.345	0.361	0.032	0.008
EB	0.529	0.226	0.024	0.048
Tile/Deck jackknife				
EE	0.048	0.088	0.144	0.132
BB	0.908	0.840	0.629	0.269
EB	0.050	0.154	0.591	0.591
Focal Plane inner/outer jackknife				
EE	0.230	0.597	0.022	0.090
BB	0.216	0.531	0.046	0.092
EB	0.036	0.042	0.850	0.838
Tile top/bottom jackknife				
EE	0.289	0.347	0.459	0.599
BB	0.293	0.236	0.154	0.028
EB	0.545	0.683	0.902	0.932
Tile inner/outer jackknife				
EE	0.727	0.533	0.128	0.485
BB	0.255	0.086	0.421	0.036
EB	0.465	0.737	0.208	0.168
Moon jackknife				
EE	0.499	0.689	0.481	0.679
BB	0.144	0.287	0.898	0.858
EB	0.289	0.359	0.531	0.307
A/B offset best/worst				
EE	0.317	0.311	0.868	0.709
BB	0.114	0.064	0.307	0.094
EB	0.589	0.872	0.599	0.790

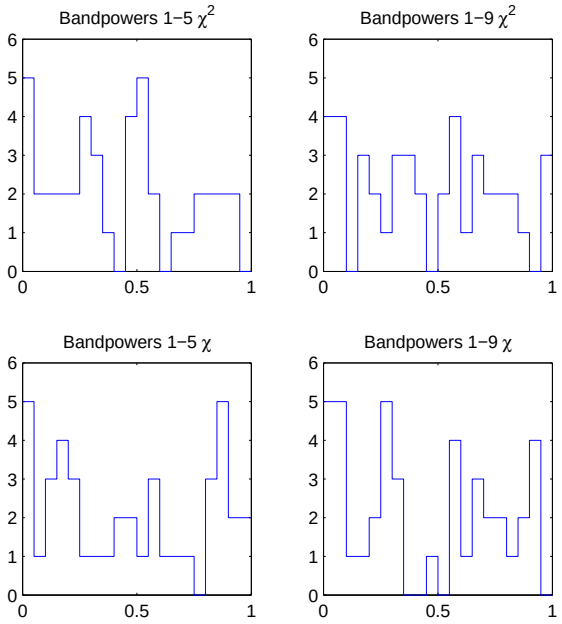

Figure 7.6: Histograms of PTE values for the χ^2 and χ metrics for all fourteen jackknife tests from Table 7.2.

7.5.1 Beam sources

As described in Chapter 4, there are several detector-pair differential beam asymmetries which can leak the temperature signal into polarization, shown in Figure 4.10. These are: differential gain, pointing, beam-width, and ellipticity.

If we approximate our beams as an elliptical Gaussian, then we can characterize them by their amplitudes (gain), g; centroids, $\vec{r}$; major and minor axes, $\sigma_{\rm maj}$ and $\sigma_{\rm min}$; and ellipse angles, θ. We can transform these to parameters which will be more useful for defining differential quantities. These are beam width,

$$\sigma_i = \left(\frac{\sigma_{\rm maj}^2 + \sigma_{\rm min}^2}{2} \right)^{1/2}, \tag{7.10}$$

plus-ellipticity,

$$p_i = \left(\frac{\sigma_{\rm maj}^2 - \sigma_{\rm min}^2}{\sigma_{\rm maj}^2 + \sigma_{\rm min}^2} \right) \cos 2\theta, \tag{7.11}$$

and cross-ellipticty,

$$c_i = \left(\frac{\sigma_{\rm maj}^2 - \sigma_{\rm min}^2}{\sigma_{\rm maj}^2 + \sigma_{\rm min}^2} \right) \sin 2\theta. \tag{7.12}$$

For *differential gain*, $\delta_g = g_A - g_B$, if two detectors in a pair with a gain offset observe a spot on the sky, then one will resolve the patch as slightly hotter. When we difference the timestreams from the detectors to determine the polarization, we are left residual power equal to the temperature times the differential gain, thus creating a false polarization signal.

Differential pointing can be thought of as the beams in a detector pair being translated. When we difference these two beams, $\vec{r}_A - \vec{r}_B$, we are left with a dipole. We can classify the direction of this pointing offset as a linear combination of a dipole oriented in the x-axis and a dipole oriented in the y-axis: $\delta_x = x_A - x_B$, and $\delta_y = y_A - y_B$. If we take the difference of the detector timestreams which suffer from differential pointing, we get nothing if the two spots observed by the A and B detector are the same temperature. However, if the spots have a different temperature, then this temperature gradient remains in the differenced timestream, leaking into the polarization signal.

Differential beam-width, $\delta_\sigma = \sigma_A - \sigma_B$, arises when the two detectors in a pair have different sizes. Whereas differential gain and pointing couple to the monopole and derivative of the temperature field observed, differential beam-width coupled to the second derivative of the temperature field. Similarly with *differential ellipticity*, the quadrupole effect will leak temperature to polarization if there is a difference in the second derivative of the temperature field in orthogonal directions, i.e. if the second derivative field is saddle shaped. We describe this quadrupole as a plus-shape and the 45° rotated cross-shape, $\delta_p = p_A - p_B$, and $\delta_c = c_A - c_B$.

We have measured our beam properties to high accuracy and they are presented in Table 7.3. Note that although one could naively expect a single number to characterize the differential gain, because the beams-shapes in a detector pair are not exactly matched, then relative gain is actually a function of multipole.

The expected level of B-mode contamination from these measured differential beam parameter is shown in Figure 7.7a, as well as the effect of deprojecting these. We can see that differential pointing has the largest systematic contamination, followed by differential gain. The effect of deprojecting differential beam-width is negligible. Differential ellipticity has a small effect when deprojected,

Table 7.3: Measured differential beam parameters [9]

Parameter[a]	Mean[b]	Scatter[c]
Differential pointing, δx	$0.80'$	$0.38'$
Differential pointing, δy	$0.80'$	$0.42'$
Differential beam-width, $\delta\sigma$	$-0.02'$	$0.1'$
Differential ellipticity, δp	-0.002	0.016
Differential ellipticity, δc	-0.004	0.014

[a] Differential parameters are calculated by differencing measured beam parameters for detectors A and B within a polarized pair.
[b] Mean across all detector pairs used in science analysis.
[c] Standard deviation across all detector pairs used in science analysis, dominated by true pair-to-pair variation.

however, it was found in simulation that deprojection modified the TE spectrum. Because of this, it was decided to subtract the differential ellipticity effect instead of deprojecting it.

7.5.2 Other sources

There are many other possible sources of polarization leakage and we characterized all we could think of. We show the expected levels (or upper limits) of these contaminants calculated from simulations using measured effects in Figure 7.7b. These are:

- *extended beam* - Beam map simulations which extends up to 4°, including beam deformities from crosstalk and sidelobes.
- *thermal contamination* - Temperature fluctuations of the focal plane being thermalized on the detectors.
- *systematic polarization error* - An overall polarization orientation miscalibration.
- *random polarization error* - A random uncertainty in polarization orientation.
- *ghosted beams* - Small secondary beams offset from the main beam produced by crosstalk between detectors and reflections off of the optics.
- *transfer functions* - A mismatch in detector pair transfer functions.
- *crosstalk* - General crosstalk between detectors.

We can see that the contamination from all these sources is negligible.

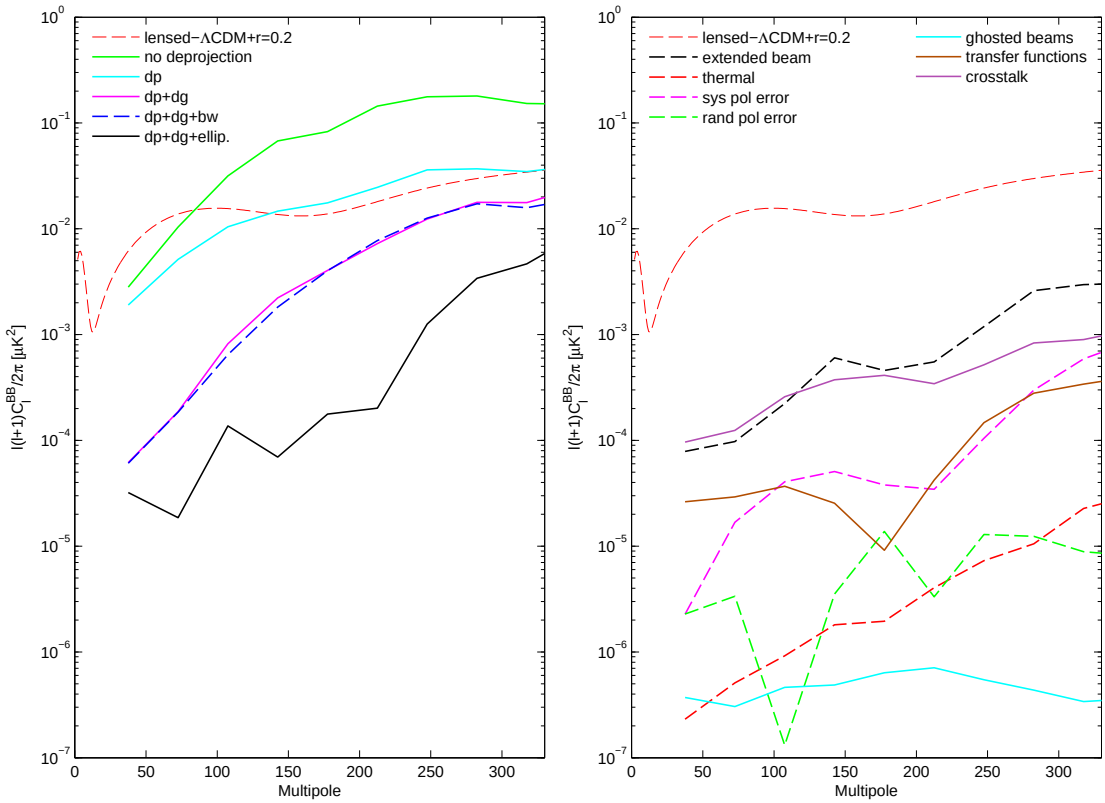

(a) Differential beam mismatch

(b) Other sources

Figure 7.7: *Right:* Expected contamination to the B-mode power spectrum calculated from simulated CMB data using measured differential beam parameters after applying deprojection for differential pointing (green), pointing + gain (purple), pointing + gain + beam-width (light blue), and pointing + gain + ellipticity (black). Lensed-ΛCDM with $r = 0.2$ is shown in red. *Left:* Expected contamination (solid lines) or upper limits (dashed lines) from other sources of spurious polarization.

7.6 Foreground contamination

A foreground is defined as any source of polarization between the CMB and our telescope. The three types of foregrounds which could potentially create false B-mode polarization are extra-galactic polarized point sources, synchrotron radiation, and polarized dust.

By design, BICEP2 observes a region of sky that is expected to have minimal foreground contamination, particularly from dust [31].

7.6.1 Polarized point sources

To determine the contamination expected from point sources we combine fluxes from the Planck 143 GHz compact source catalog in our field [60] with 20 GHz polarization information from the Australia Telescope Compact Array (ATCA) [51]. We then subtracted these objects from our map and calculated the effect on polarization. We found that these point sources contributed to the B-mode power spectrum at the level of $r \approx 0.001$.

7.6.2 Synchrotron radiation

At low frequencies, synchrotron radiation – emission from relativistic electrons spiraling through magnetic fields – is the most prevalent potential foreground. To determine the amount of synchrotron radiation we expect in our field, we use WMAP 23 GHz maps in our observing field and extrapolate these to 150 GHz using a power law with spectral index $\beta = -3.3$, as derived from WMAP foreground data products. We found that the WMAP 23 GHz map is noise dominated in our field and at angular scales greater than $\ell = 30$. From extrapolating WMAP's noise dominated maps to 150 GHz, we find the expected contamination level to be at the level of $r = 0.003$. We also cross correlated our maps with the WMAP 23 GHz map and found the result to be negligible. This was investigated using a spectral index as high as $\beta = -2.8$ with negligible effects.

7.6.3 Polarized dust

The least well characterized potential foreground is polarized dust. Dust is dominant at higher frequencies and has not been well studied at 150 GHz in our field. We have investigated several current dust models, as well as provided two new ones, for the expected level of contamination. These are shown in Figure 7.8 and are well below the observed level of B-mode polarization, particularly at higher ℓ. We use the following dust models:

- *BSS* - Bi-symmetric spiral model of Galactic magnetic fields [57].
- *LSA* - Logarithmic spiral arm model of Galactic magnetic fields [57].

- *FDS* - Model 8 from [31], assuming a 5% uniform polarization fraction and setting $Q = U$.
- *PSM* - The Planck sky model version 1.7.8 [23], with 15% intrinsic dust polarization fraction and Galactic magnetic field pitch angle set to $-30°$.
- *DDM1* - Data-driven model 1, 353 GHz Planck map scaled to 150 GHz using a constant emissivity value of 1.6 and temperature of 19.6 K. Polarization angles from the PSM are used and a constant 5% polarization fraction is assumed.
- *DDM2* - Data-driven model 2, is derived similarly to DDM1 but maintaining the polarization fraction and angles in the 353 GHz map. DDM2 contains significant noise above $\ell = 200$ from the resolution of the polarization fraction and angles in the 353 GHz map and thus has been truncated in multipole space.

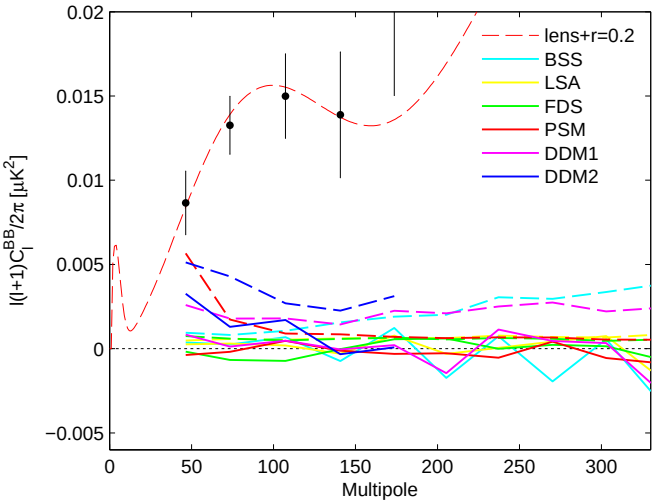

Figure 7.8: Predicted level of B-mode contamination due to galactic dust from several models. Auto-spectra are plotted as dashed lines and cross spectra with BICEP2 data are plotted as solid. Real BICEP2 bandpowers are plotted as black dots and lensed-ΛCDM with $r = 0.2$ is plotted as a dashed red line.

We can see in Figure 7.8 that all the auto-spectra of the dust models aside from DDM1 and DDM2 are well below our observed B-mode data points, and the cross spectra are all consistent with noise, indicating that the BICEP2 data are not correlated with dust. Although we believe DDM1 and DDM2 to be fairly

conservative estimates of the polarized dust contamination in our field, we will have to wait until Planck releases their polarization maps to know the actual contamination level. In addition, a detection of this polarization at 100 GHz (or taking the cross spectrum of BICEP2 with a high-sensitivity 100 GHz B-mode map) will alleviate foreground concerns.

7.7 Comparison with Bicep1 and Keck array

As robust as our internal consistency checks are, the most powerful consistency test is to cross-correlate BICEP2 with another experiment which has uncorrelated noise and see the same signal. As we have access to both BICEP1 and Keck array data – the successor to BICEP2 utilizing a more compact design to pack five 150 GHz BICEP2-like telescopes onto one mount, we were able to take cross-spectra with these. As described in greater detail in Chapter 4, the detectors, readout, and analysis procedures are completely different for BICEP1. Although the Keck array shares detector technology, instrumental systematics are unlikely to be correlated.

Figure 7.9 shows the EE and BB power spectra for the BICEP2 auto-spectra, BICEP2×BICEP1$_{100\ \mathrm{GHz}}$, and BICEP2×BICEP1$_{150\ \mathrm{GHz}}$. We can see that all three spectra detect the E-mode power spectrum with high signal-to-noise[6], and both BICEP2×BICEP1$_{100\ \mathrm{GHz}}$ and BICEP2×BICEP1$_{150\ \mathrm{GHz}}$ also show positive correlation. Although the significance of the BICEP2×BICEP1$_{100\ \mathrm{GHz}}$ is $\approx 3\sigma$, measurements with higher significance are needed to confirm a detection at 100 GHz.

We also looked at cross-spectra between BICEP2 and the frequency-combined BICEP1 data [6], shown in Figure 7.10. Unsurprisingly, the frequency-combined cross-spectra shows a $\approx 3\sigma$ detection of B-modes over lensed-ΛCDM. Although the Keck array data are still preliminary, Figure 7.10 shows a strong correlation with BICEP2. Note that the two points between $200 < \ell < 250$ which are discrepant with the lensed-ΛCDM with $r = 0.2$ theory curve become consistent when crossed with Keck array data. This implies that those discrepant points in the BICEP2 auto-spectrum are likely "unlucky" statistical fluctuations and not real.

[6]The lowest multipole points do appear to be discrepant with the theory curve however this is likely due to sample variance.

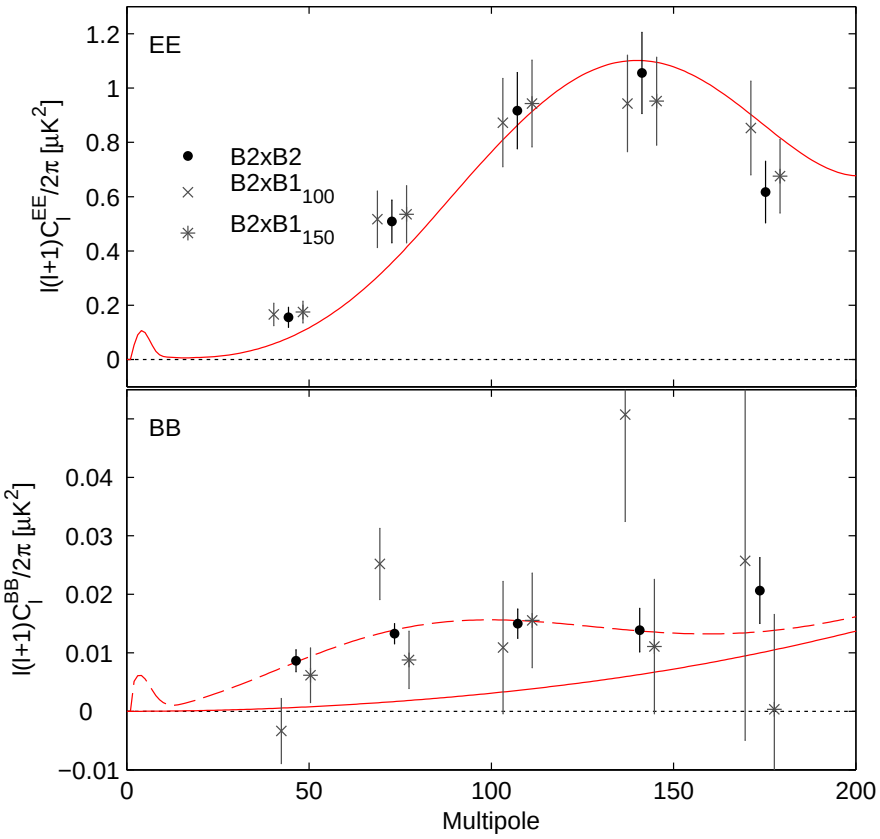

Figure 7.9: BICEP2 auto-spectra plotted with cross-spectra between BICEP2 and BICEP1 100 GHz, and between BICEP2 and BICEP1 150 GHz for E-modes (top) and B-modes (bottom).

7.8 Cosmological interpretation

After accounting for systematic and foreground contributions, we are left with an excess of B-mode power over lensed-ΛCDM at large angular scales. This excess is correlated across two separate experiments.

As this excess appears in the same multipole region where Inflationary B-modes are expected, we fit our data to the lensed-ΛCDM which includes tensor modes. Following the same procedure as for the constraints from self-calibrated BICEP1 data, we find the maximum-likelihood tensor-to-scalar ratio $r = 0.2^{+0.07}_{-0.05}$. Using this model we can rule-out $r = 0$ to 7.0σ significance [10].

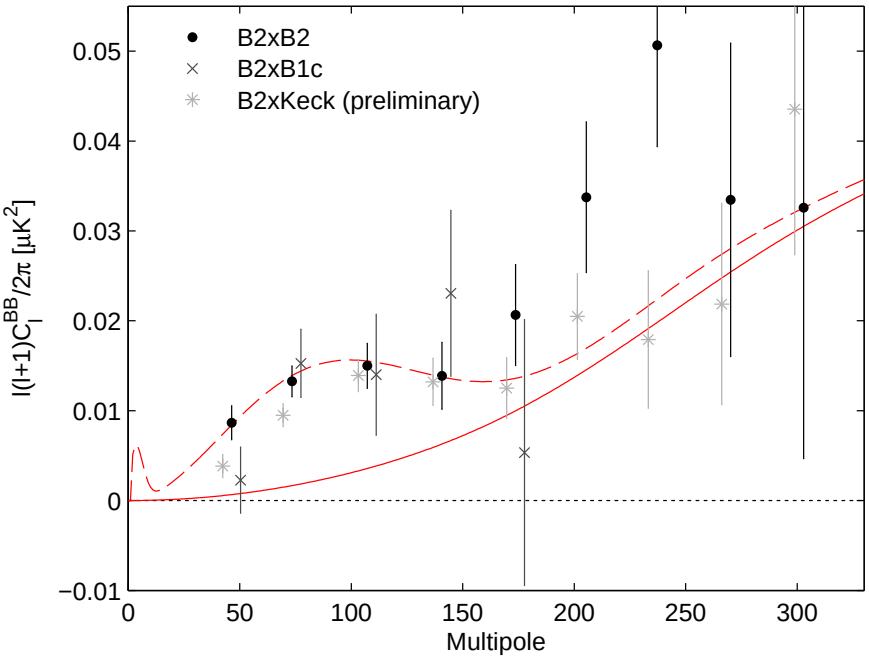

Figure 7.10: BICEP2 auto-spectra plotted with cross spectra between BICEP2 and the frequency-combined BICEP1 data, and between BICEP2 and the Keck array (at 150 GHz).

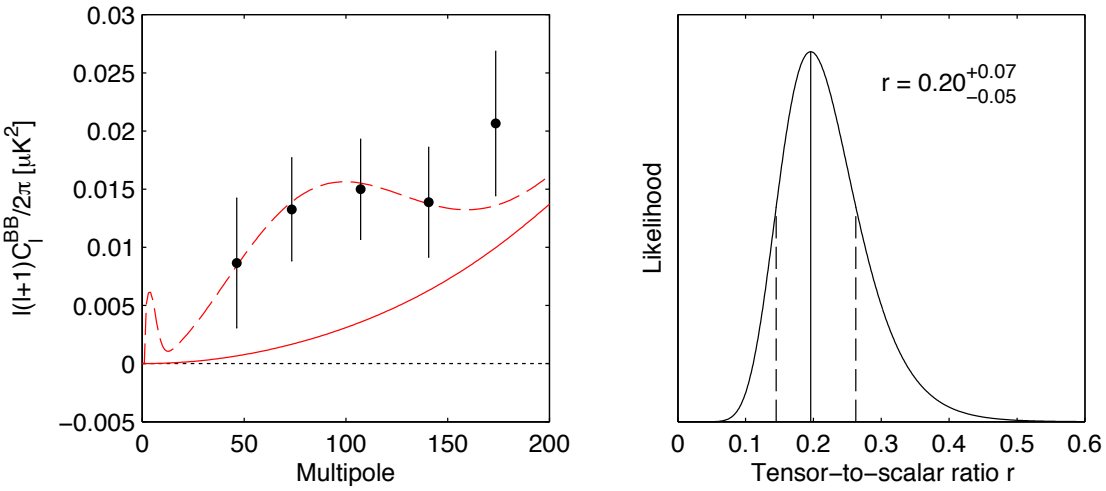

Figure 7.11: *Left:* BICEP2 BB bandpowers with the best-fit lensed-ΛCDM + $r = 0.2$. *Right:* Likelihood plot of the tensor-to-scalar ratio from these data. $r = 0$ is disfavored by these data to 7.0σ significance.

Tension with constraints derived from temperature data

Although the 95% upper limit on r set directly from polarization data was $r < 0.65$ [42], Planck had recently set a limit of $r < 0.11$ from combining Placnk, SPT, and ACT temperature data with WMAP polarization data[7] [1]. Recall from Chapter 2 that experiments which precisely measure the temperature power spectrum can estimate r using the amplitude of the scalar modes, the scalar spectral index, and the slow-roll consistency equation.

The Planck constraint assumes that the scalar modes obey a power law exactly. If we allow deviations from a perfect power law, such as "running" of the scalar spectral index, $dn_s/d\ln k$, the Planck constraint relaxes to $r < 0.26$ with 95% confidence [1]. It is possible that the scalar perturbations do not follow a simple power law. As shown in [66], Planck and WMAP have a deficit in power at low-ℓ even in a model which assumes $r = 0$. Allowing r to take on non-physical negative values, the maximum-likelihood r from Planck data actually peaks 1.6σ below zero. [66] shows that this can become a 3σ preference for negative r with an *a posteriori* choice of ℓ range. This tension and preference for a non-physical r value can be interpreted as evidence that there must be an extension to the model, whether it be the running of the scalar spectral index, a non-zero tensor spectral index, n_t, or a higher effective number of relativistic species, $N_{\rm eft}$.

[7] Note that the WMAP polarization data is weak and was only used to constrain the optical depth to the last scattering surface, τ.

Chapter 8

Path forward

This is a fantastically exciting time in Cosmology. High-precision measurements of both the E- and B-mode polarization are possible with today's technology, which will allow us to probe many new regimes of physics. With this, there are many paths forward for both B-mode and polarization rotation science.

8.1 B-modes

Within one week, the B-mode power spectrum was detected at large and small angular scales [69, 10]. As this search was so fiercely competitive, there are many more telescopes poised to publish their findings soon [32, 55, 64, 59], and many that are being constructed [70, 28].

The BICEP2 detection, though high significance, needs to be confirmed. It is unlikely that there is an error in our telescope, especially considering the significance when cross-correlating with both BICEP1 and the Keck array. Although the cross spectrum with the BICEP1 100 GHz map led to a 3σ significance detection of degree-scale B-mode polarization, and constraints on the spectral index of the polarization were consistent with CMB [10], we need a multi-frequency high-significance detection to confirm that the polarization isn't due to foregrounds. Though we have shown that synchrotron radiation is well below the level of our detected B-mode power, our dust projections are just models. We require accurate measurements of polarized dust in our regions to definitively rule-out dust

contamination. With the Planck satellite and the Keck array, we should have measurements of dust and multi-frequency detections of B-mode polarization within the next two years.

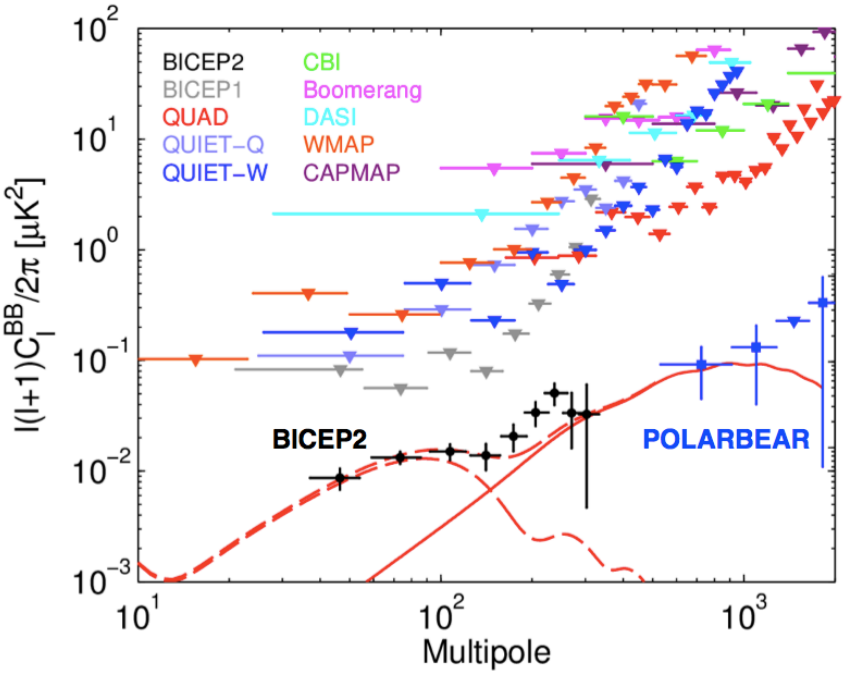

Figure 8.1: The search for B-mode polarization. Within one week, B-mode power was detected in both the lensing and Inflationary regimes. Here, the solid line is the lensed B-mode spectrum, the dashed lines are the Inflationary and Inflationary+lensing spectra.

If the B-mode polarization that we have detected can be confirmed to be Inflationary, then we have ushered in a new era in polarization astronomy. With light, we cannot see further back than the time of the CMB. With B-mode polarization, we can now probe time scales $< 10^{-32}$ seconds after the Big Bang. From Equation 2.29, the BICEP2 maximum-likelihood r value corresponds to the grand-unification theory (GUT) energy scale. Thus with precise measurements of the B-mode spectrum, we will be able to probe physics at the GUT scale. Measuring the complete spectrum will involve de-lensing using measurements of the lensed B-mode spectrum from telescopes that target small-angular scales.

In addition to the Inflationary B-modes, lensed B-modes offer a wealth of information about the makeup and structure of our Universe. Thus lensing is

sensitive to cosmological parameters which trace out structure formation such as the dark energy equation of state and the sum of the masses of the neutrinos. It is likely that within the next five years, measurements of the lensed B-mode spectrum will provide the long sought-after neutrino mass hierarchy.

8.2 Cosmic polarization rotation

With the precise measurements of the polarization of the CMB, we can easily measure correlations between temperature and polarization, and between E-mode and B-mode polarization as probes of cosmic polarization rotation. With the noise-levels currently achieved, we can measure a rotation angle of one degree to 5σ significance. However, for these TB and EB correlations, systematic mis-calibration of detector polarization orientations provides a significant source of uncertainty. Uncertainty in detector polarization angles scales quadratically for BB, but linearly for TB and EB. Thus methods for calibrating detector polarization orientations to measure the B-mode power spectrum that have 0.5° precision have not been precise enough to constrain polarization rotation to high significance.

There are paths forward to improve both man-made and astrophysical calibrations of detector polarization angles. Although dielectric sheet calibrators have been prone to systematic installation errors, new wire-grid polarizers coupled to bright microwave sources are being developed and deployed to characterize polarization angles. Though these sources suffer from their own uncertainties, I plan to lead a larger effort to characterize and understand these.

Measurements of Tau A to calibrate detector polarization angles are limited by the precision of the polarization of Tau A, which is only known to 0.5° [5]. Improved measurements from telescopes like those at ALMA [72] can reduce this uncertainty. In addition, CMB telescopes using improved ground-based man-made calibrators can be used to characterize Tau A,

If we assume there is no cosmic polarization rotation, we may continue to use measured TB and EB correlations as a calibrator. This self-calibration technique has been adopted by BICEP1, BICEP2, and POLARBEAR, and is likely

to be used by many other CMB polarimeters in the coming years.

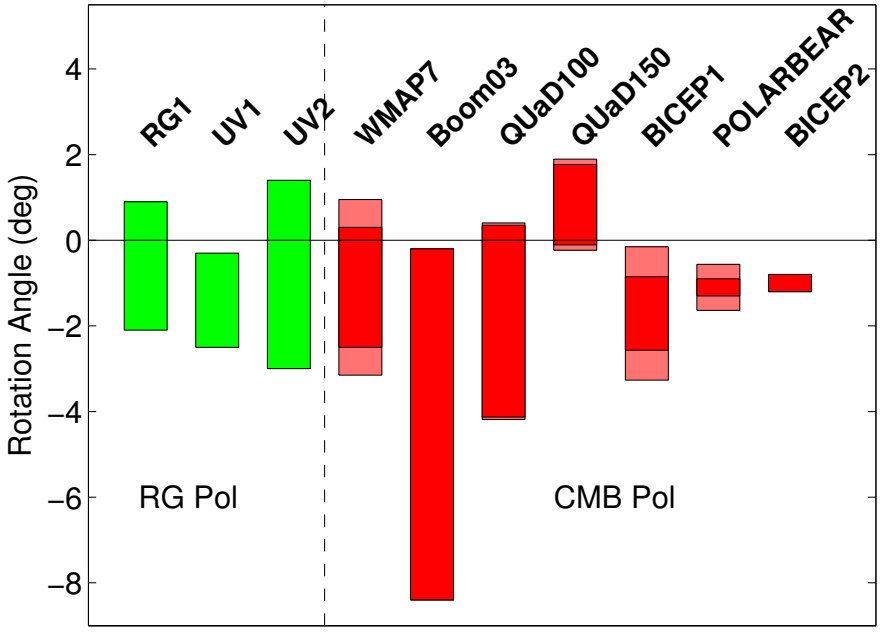

Figure 8.2: Derived rotation angles from galaxy sources from Table 3.1 (green) and the CMB from Table 3.2 with the BICEP1 and BICEP2 results (red). The solid bars represent the statistical uncertainty and the light red bars represent the combined statistical and systematic uncertainties (where available). Although BICEP2 has the most precise measurement of a polarization rotation angle, the systematic uncertainty has not been thoroughly investigated.

Though popular in the late 1990s, the study of the polarization of galaxies in the radio and UV spectrums has been all but abandoned. There are many improvements to these measurements that can be done. Simply increasing the number of sources observed should improve the uncertainty on the constraint by the inverse of $\sqrt{N}$ thus an increase to $\sim$400 objects would allow comparable sensitivity to near-future CMB experiments [40]. Measuring the intensity and polarization of radio sources and performing an E- and B-mode decomposition will also allow for more sensitive constraints by computing the intensity-B-mode correlation. A combination of these two improvements would yield higher precision from this method.

Through a combination of improved calibration on current and next generation CMB telescopes and measurements of the polarization of radio galaxies, we

should be able to determine cosmic polarization rotation to high precision which will allow us to probe new parity violating physics [33].

Figure 8.3: Light reflects and refracts off of ice crystals in the upper atmosphere to create a 22° halo, sun dogs (bright spots), upper tangent arc, and a parhelic circle.

Appendix A

Spectral bandpass of the BICEP2 telescope

In order to determine the band center and bandwidth of BICEP2, we took Fourier transform spectronomer (FTS) measurements before and after deployment. The pre-deployment FTS testing allowed us to find and fix a blue-leak, where out of band radiation was directly coupling to our TES detectors. Measurements at Pole were used to determine the expected temperature-to-polarization leakage due to spectral gain mismatch between detectors in a polarization pair.

A.1 What is an FTS?

FTSs are calibration devices used to determine the frequency response of a detector. The consist of a source, a beamsplitter, a stationary mirror, a moving mirror, and an output. Scanning the moving mirror will create an interference pattern which is the Fourier transform of the spectrum of the detector. Although we use a Martin-Pupplett interferometer which requires two sources, a splitting wire-grid, and roof mirrors to invert the polarization, the technique is essentially the same. The actual FTS used at Pole is shown in Figure A.1.

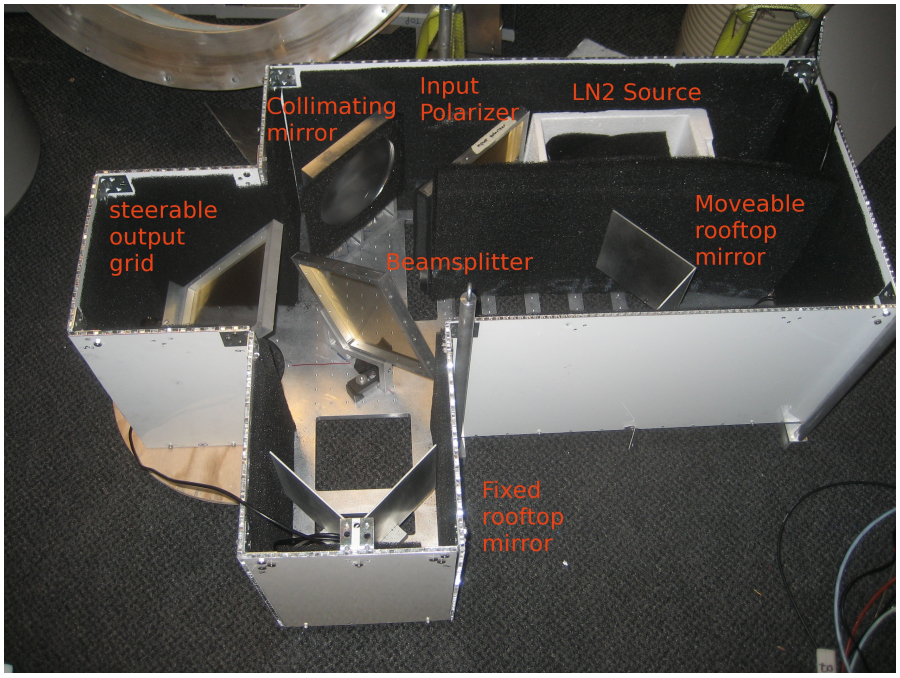

Figure A.1: The FTS used at Pole for BICEP2 calibrations. The sources are liquid nitrogen and room temperature eccosorb which are polarized by the input polarizing grid. The resultant radiation gets collimated before passing through a wire-grid beam splitter. One of the polarizations reflects to the moving roof mirror and the other passes through to the stationary roof mirror. The two polarized signals recombine at the beam-splitter with a phase shift dependent on the distance of the moving mirror and are directed to the telescope via the steerable output grid.

A.2 Measurements at Pole

FTS measurements were taken in December of 2011 and again in December of 2012, prior to decommissioning. Problems with coupling of the FTS to the telescope in the December 2011 run led to low signal to noise. Only the data set taken in 2012 was used for instrument characterization.

The FTS used in 2012 was designed to sit directly above the BICEP2 cryostat (off the mount), coupling the output to the detector beams without the need for complicated optical paths like those used for BICEP1 [68]. Though ultimately, this

led to repeatability issues due to the output not filling the beam of the detectors, this was a much easier setup to employ and small modifications to the design can fix this. As the FTS was designed to be stationary when attached to the cryostat, a movable output grid was used to direct the beams from the output across the focal plane. We were able to illuminate $\sim 4-8$ detectors per pointing and steered the beam across the focal plane to get spectral responses for all the detectors. We rotated the cryostat to several orientations: 0, 45, 90, 135, and 180, to test for systematic effects. We also took data for many different output grid orientations to track how the detectors' responses changed as the output was steered away.

A.3 The pipeline

Generally speaking, the steps to go from interferogram to spectra are as follows:

- load data
- cut interferogram from data
- low pass filter interferogram
- center data around the white light fringe (WLF)
- window with a Hann function
- take fourier transform

This is all handled with the function `fts2fft` which resides in `FTS_analysis/` in `bicep2_analysis/`. To get spectra from time ordered data, use `[fftdat f] = fts2fft(t1, t2, gcp, x, v, demod)` where:

- `t1`: the start time of the FTS scan
- `t2`: the end time of the FTS scan
- `gcp`: the gcp coordinate for a given detector
- `x`: the scanning distance from WLF
- `v`: scanning velocity

Figure A.2: The FTS coupled directly to the BICEP2 cryostat prior to decommissioning at the South Pole in December 2012. The mount is just off screen to the left.

- `demod`: flag to demodulate data
- `fftdat`: the output structure containing:
  - `fftdat.fft`: the final spectra
  - `fftdat.orig`: the original timestream, nothing applied
  - `fftdat.ref`: reference signal used for demodulation (when applicable)
  - `fftdat.demod`: demodulated timestream (when applicable)

  - `fftdat.filtered`: low pass filtered timestream
  - `fftdat.rmslope`: filtered and de-sloped timestream
  - `fftdat.centered`: filtered, de-sloped, and centered about the WLF timestream
  - `ffftdat.hanning`: filtered, de-sloped, centered, and windowed with a Hann window timestream

- `f`: the frequency range for the FTS scan.

A.3.1 Getting an interferogram

The function `fts2fft` loads in the data for the specified detectors in the range between `t1` and `t2` by calling `load_arc`. Note that loading too many detectors at once will crash the Matlab session but I've been able to load 50 at a time without issue. As usual, the output is the structure `d` which contains all the pertinent information. The function then passes this structure to `get_interferogram` which returns the part of the timestream where the moving roof mirror is translating.

`get_interferogram` first throws out points where the stage is stationary (at the beginning and end of the scan). It then searches the encoder output for where the WLF should be then, based on the speed and the throw, finds the edges of the scan and returns the relevant part of the data.

A.3.2 Filtering

The low pass filtering is done directly in `fts2fft` using a 2 pole low pass butterworth filter. The normalized cutoff frequency is set to 0.04. Recall that the cutoff frequency is normalized by the Nyquist frequency which is half the sample frequency ($f_n = f_c/(f_S/2)$). The butterworth filter is then applied using `filtfilt`, effectively making it a 4-pole filter.

For our timestreams, there was a residual slope signifying a change in loading from one edge of the scan to the other, most likely due to internal alignment issues which would require a rather significant modification to fix. I removed this

slope by doing a simple one pole polynomial subtraction. This was done by the sub-function `deslopefts`.

A.3.3 Centering around WLF

When trying to produce spectra quickly, this step is often skipped. If you plot the absolute value of the fft, you will get the spectra but you will also rectify the noise. It is much better to spend a little time making sure that the timestream is centered about the WLF. To do this, I wrote the function `center_wlf_v2` which centers about the WLF by shifting the timestream until the power in the imaginary part of the fft is minimized.

A.3.4 Windowing the data

The last step before taking the Fourier transform is to window the data using a Hann window. I don't know exactly (at this time) why the Hann window was chosen over any other window but I know the Hann window is supposed to have very low aliasing. The window kernel looks like:

$$w(n) = 0.5 \cdot \left[1 - \cos\left(\frac{2\pi n}{N-1}\right)\right], \quad 0 \leq n \leq N-1$$

where N is the sample size.

A.3.5 Getting the spectra

Before taking the fast fourier transform (fft), we need to shift the data so that the WLF occurs at the edges of the timestream instead of the center. This creates a more visually recognizable spectrum. Luckily matlab has the `fftshift` command which does this automatically. We then take the fft.

A.3.6 Correcting for the spectrum of the source

The observed interferogram is the inverse fourier transform of the intensity of the source, so when we take the fft we are not seeing the telescope's pass band but some combination of the source spectra with the telescope's pass band. To

correct for this effect, we must divide out the spectrum of the source. To do this, we assume that the liquid Nitrogen source behaves as a blackbody, characterized by the Rayleigh-Jeans law.

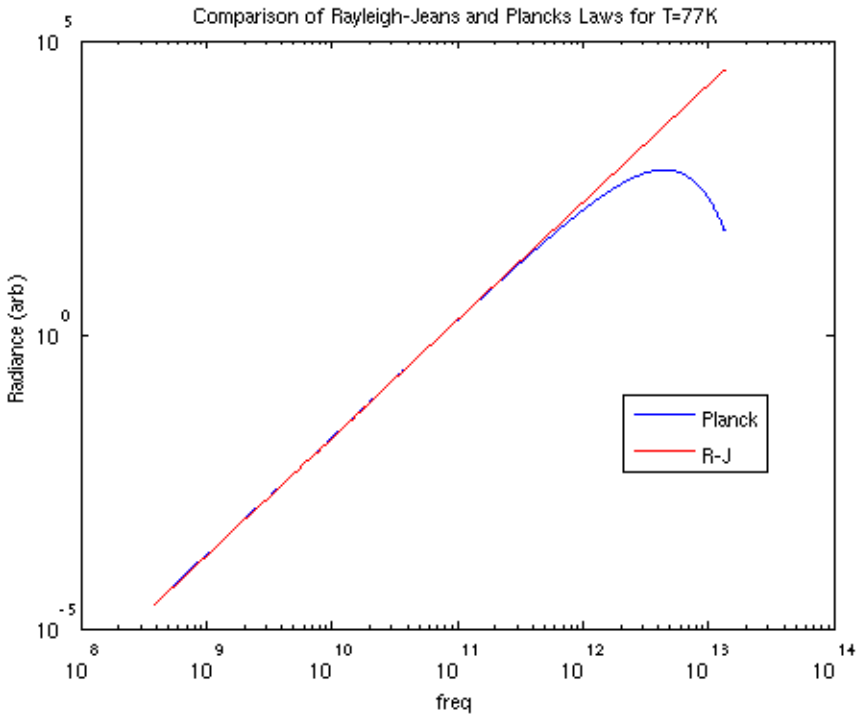

Figure A.3: Comparison plot of the Radiance for a Blackbody using Planck's Law and for the Rayleigh-Jeans Law. Note that in our frequency range, 100 GHz - 1 THz, the Rayleigh-Jeans law is a fine approximation.

The Rayleigh-Jeans law can be stated as:

$$B(\nu) = \frac{2kT\nu^2}{c^2} \tag{A.1}$$

where k is the Boltzmann constant, T is the temperature of the blackbody, ν is the frequency, and c is the speed of light.

The actual application of this in the pipeline is fairly simple and is handled by the function `rj_corr`. `fts2fft` passes `rj_corr fftdat.fft` and `f`. `rj_corr` calculates the Rayleigh-Jeans spectrum for the frequencies given and then divides the fft spectrum by the Rayleigh-Jeans spectra.

A.3.7 Shifting the frequency axis

The only tricky part in all this is shifting the output of the fft to the correct frequency range. To do this, we scale the sample frequency:

$$f_i = F_s \left(\frac{c}{4v}\right) \cdot i, \quad i = 0..N/2 \tag{A.2}$$

Where

- F_s is the sample frequency
- c is the speed of light
- v is the velocity of the moving roof mirror.
- N is the total number of samples (or $N+1$ for odd length data sets)

Note that the notation f_i is meant to correspond to the i^{th} frequency bin of the fft. This is defined from 0 to the Nyquist frequency.

A.4 Results

The array-averaged bandpass for "really good light" (RGL) detectors is shown in Figure A.4, along with the atmospheric transmission, and the CMB anisotropy spectrum.

A.4.1 Band center

To calculate the band center, I used the following definition:

$$\langle \nu \rangle = \frac{\int \nu F(\nu) d\nu}{\int F(\nu) d\nu}, \tag{A.3}$$

where $F(\nu)$ is the spectral response for a given detector. With this definition, BICEP2's array-averaged band center is 149.8 ± 1.04 GHz.

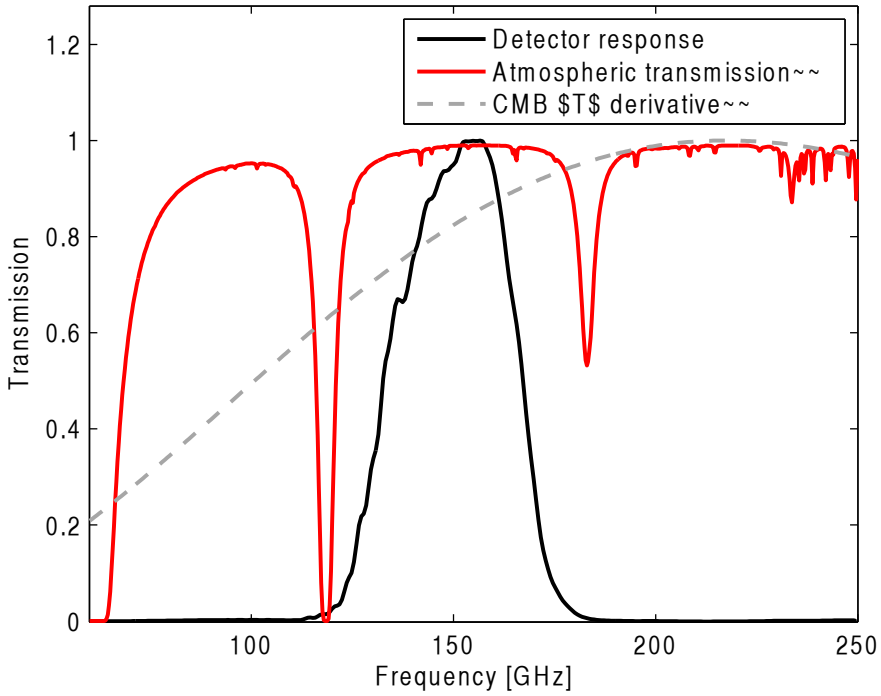

Figure A.4: Array-averaged bandpass for RGL detectors (black) plotted with the atmospheric transmission (red) and the CMB anisotropy (gray). The BICEP2 band has been normalized to one.

A.4.2 Bandwidth

For bandwidth I use the following definition:

$$\text{bandwidth} = \frac{\left(\int F(\nu)d\nu\right)^2}{\int F^2(\nu)d\nu}. \tag{A.4}$$

From this definition, the array-averaged bandwidth for BICEP2 was found to be 42.2 ± 0.9 GHz.

A.5 Spectral gain mismatch

For BICEP2, we measure the spectra to determine how much temperature to polarization leakage to expect due to differences in spectral responses between detector pairs and calibration off of the atmosphere. We define the spectral gain

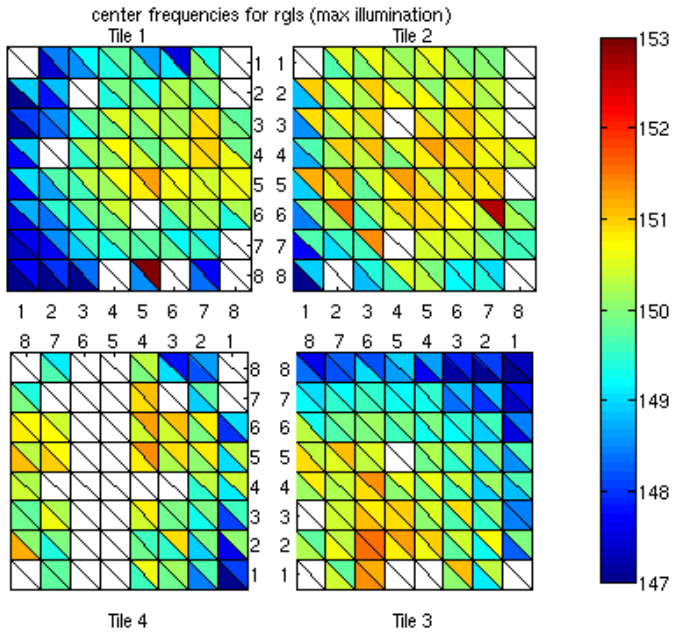

Figure A.5: Calculated band centers for the BICEP2 focal plane. Each square represents a detector pair used in the final data set, called RGL ("really good light") detectors. White squares represent non-RGL, dark, or dead detectors.

mismatch as

$$\xi = \frac{G_A - G_B}{G_A + G_B}, \tag{A.5}$$

where G is the responsivity for a given detector, defined as

$$G_{A,B} = \frac{\Gamma_{\rm sky}}{\Gamma_{\rm CMB}}. \tag{A.6}$$

Here, Γ is given by

$$\Gamma = \int F(\nu) S(\nu) \lambda^2 d\nu, \tag{A.7}$$

where $F(\nu)$ is the spectral response for a given detector, $S(\nu)$ is the spectral radiance, and λ^2 accounts for the throughput of the optics.

The spectral radiance for the atmosphere is calculated from the software AM7.2[1] and for the CMB it is just the derivative of a blackbody with peak temperature set to 2.7 K. Both spectral radiances are shown in Figure A.4. For BICEP2 we calculate the responsivity using $100 \leq \nu \leq 200$ GHz for the limits of integration.

[1] https://www.cfa.harvard.edu/ spaine/am/

Unfortunately the repeatability of the FTS pointing and illumination coupled with the BICEP2 band's slight coupling to the oxygen line led to an upper limit on the spectral gain mismatch that the standard deviation of $\xi < 1.7\%$, below the 0.35% requirement for $r < 0.01$[2]. Although the actual spectral gain mismatch is likely below this level, any contamination due to spectral gain mismatch is removed by relative gain deprojection.

[2]This was found by taking the $\sim 1\%$ requirement from [68] and scaling it by $1/\sqrt{10}$ to reach $r < 0.01$ sensitivity.

Appendix B

Algorithm for determining snowfall on the BICEP2 window

B.1 Cosmology at the South Pole

The South Pole offers a fantastic environment for telescopes which operate in the microwave spectrum. Being located in the world's largest desert, the water content in the atmosphere is among the lowest worldwide, reducing noise contributions from atmospheric water emission line. In addition, due to the extremely low temperatures and pressure, residual atmospheric water is mostly frozen, and ice crystals do not contaminate in our band.

The South Pole has a fairly constant wind stemming from the top of the plateau. Occasionally this wind will kick up ground-snow and blow it into the ground shield of our telescopes. Although our telescopes are designed with snow mitigation techniques, we monitor our windows for snow accumulation using an optical/near-infrared camera.

B.2 Snow in July?

Observations from early July 2011 seemed to have a large amount of data failing quality cuts. During inclement weather[1], the detector responses would vary wildly, with significant noise. However, during this period, the phenomenology of the detector responses was very different from standard bad weather. For both BICEP1 and BICEP2, a near-infrared camera was installed within the lower forebaffle (LFB) which captured pictures of the telescope window every 20 minutes. A quick glance at the pictures corresponding to the oddly behaving periods showed a significant amount of snow accumulation on the window.

To prevent snow accumulation, a thin polypropylene membrane was installed just above the window. We pumped room-temperature nitrogen gas between this membrane and the window so any snowfall will be sublimated away. Figure B.1 shows a picture of this membrane before installation. Light snowfall will sublimate within a few seconds but heavier snowfall or large chunks of snow which can fall on to the membrane will take much longer.

B.3 Classifying LFB IR camera images

For BICEP1, the LFB IR camera images were displayed chronologically on a rudimentary website where users could mark images with snow contamination. This became something of a game as members of the collaboration would compare how many images they could scrutinize[2]. Classifying the LFB IR camera images by hand is tedious and time consuming, and although the "who can count the most" game was successful for BICEP1, there was no such excitement over classifying possible snow contaminated images for BICEP2.

[1] Defined as overcast sky or whiteout conditions.

[2] The images were tagged with the user's initials once they had been classified.

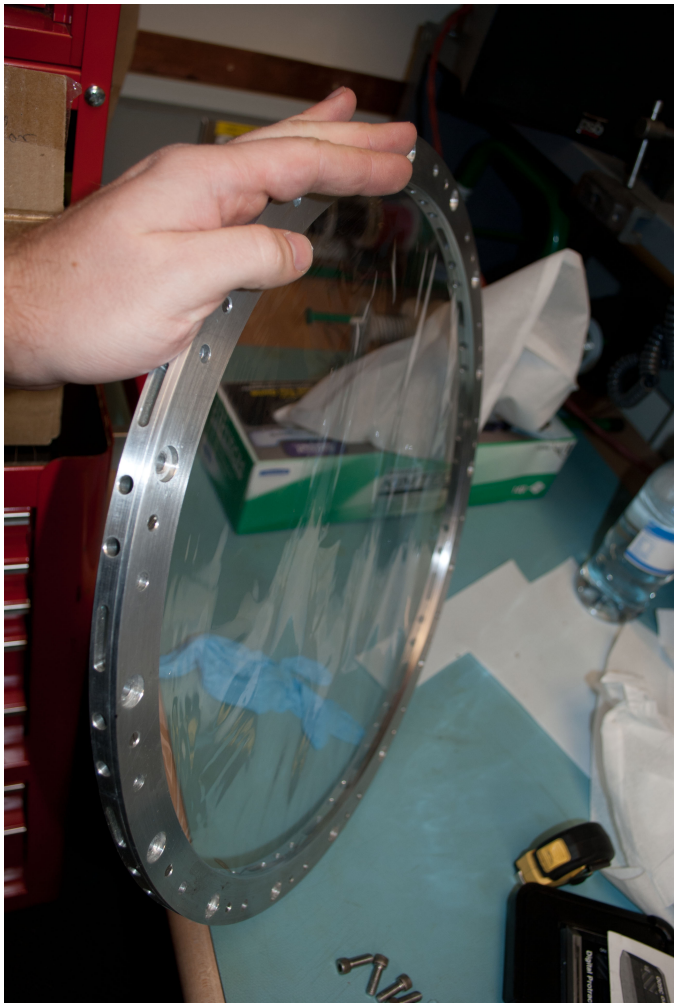

Figure B.1: Picture of the membrane which covers the BICEP2 window. Room-temperature nitrogen gas is pumped through the area under the polypropylene sheet so that any snowfall will sublimate quickly.

B.3.1 Algorithm

I created the function `lfbsnow.m` which resides in the `bicep2_analysis/util/` folder of the standard BICEP2 pipeline. For a given set of consecutive tags[3], the function loads the saved LFB IR camera images within the range of tags and for each image:

- crops the area outside of the window

[3]Usually this function is called per schedule: the full coverage of the BICEP2 patch which takes three days.

- removes the black "crosshairs"
- applies a 2-D fast Fourier transform
- takes the mean value of the area 60×110 pixels around the center of the 2-D FFT.

The function returns a structure which contains a time-ordered vector of outputs from the snow finding algorithm in arbitrary snow units (ASU), the time axis in appropriate units, and the LFB IR camera images within the tag range. Classification and visualization are done when generating the webpage described in Section B.4.

Figure B.2 shows a representative image from the LFB IR camera, without snow contamination. There are three features which stand out immediately: 1) the cross-hairs from the camera, 2) the bright reflection off of the aluminum membrane housing, and 3) the faint reflection off of the membrane itself. This image registers as 1400 ASU from the snow-finding algorithm. When snow is present, the output of the algorithm will increase dramatically, jumping to 2500 and 6900 for the examples of light and heavy snow contamination, respectively, as shown in Figure B.3.

B.3.2 Limitations

Although the snow-finding algorithm is fairly robust during nominal operating conditions, there are a few failure modes. First, if the camera is malfunctioning, the resultant images can be classified as light snow even though they are clear. This is due to a striping pattern that leads to excess power in Fourier-space in the region where the snow-finding algorithm is most sensitive. An example of this is shown in Figure B.4, where a light snow image has the same ASU value as the low-quality image. Occasionally the camera returns extremely low quality images who's ASU values oscillate wildly. These low-quality images would be relatively easy to ignore by looking at the snow-finding algorithm output as a function of time. As the snow-finding algorithm was implemented as a tool to help classify odd behavior in the data and not to automatically apply cuts, this functionality was not implemented.

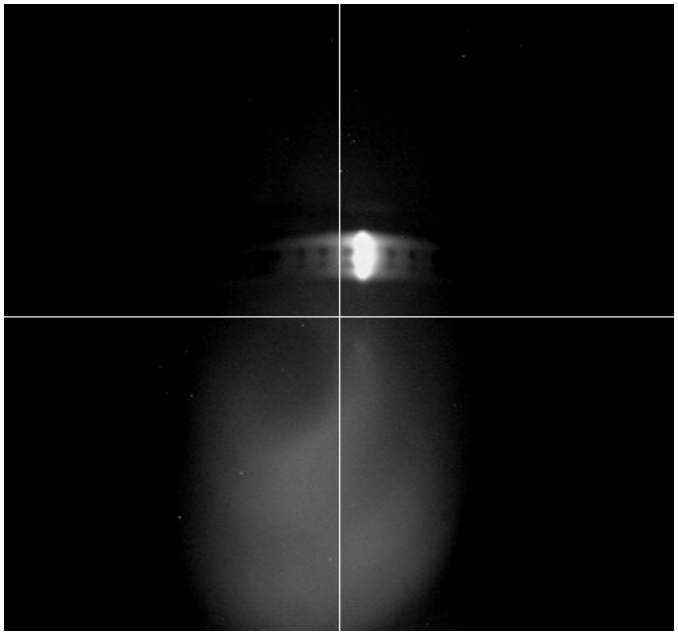

Figure B.2: Lower Forebaffle (LFB) IR camera picture showing no snow contamination. The structure just to the right and above the center is the edge of the aluminum window housing. The gray wisp in the center is the glare off of the membrane. This image registers as 1400 ASU from the snow finding algorithm.

Another failure mode is from contamination due to the sun during summer months. Although the algorithm can still spot snow successfully, baseline has moved significantly so any future automation will need to adjust the threshold depending on the time of year.

B.4 HTML browser

During BICEP2's operation, the graduate students and postdocs took turns as "reduc-czar[4]," where you were tasked with running that week's data through the initial processing pipeline, generating data quality plots, reviewing these plots, and producing a summary report to send to the collaboration. The collaboration would then collectively review the report at the next meeting.

[4]Though the name certainly implies a position intended to prevent the spread of something, i.e., "drug-czar," we used it in more of a "buck-stops-here" role. A position that I held frequently throughout my research.

The plots were displayed on the "scanset browser" webpage, where statistics were tracked per scanset, phase, and schedule[5]. I modified the reduc-czar code to automatically run the snow finding algorithm on that week's data and append the plots to the HTML browser. An example of the output plot which would appear on the scanset browser webpage can be found in Figure B.5. The output plot has two primary sections. In the top panel is a plot of the output of the snow finding algorithm for each image in the three-day schedule with respect to time. The red line is the threshold for which anything above is likely snow. Each black point represents one LFB IR camera image. The red squares highlight the five most egregious offenders for each snow event (if found). In the bottom panel, the LFB IR camera images corresponding to these five worst-offenders are shown. In Figure B.5, we can see a few phenomenologies. In the first LFB IR camera image, we see a relatively light scattering of snow – most likely blown in from the wind. From the output of the algorithm, we can see that the snow accumulates slowly and is replenished by the wind since the snow finder plateaus at around 3000 ASU[6] for the next several hours. In the second LFB IR camera image, we see a large amount of snow, corresponding to an off-the-scale peak in the output plot. Most likely, this is due to snow accumulation from the upper and lower forebaffles falling onto the window. The rest of the LFB IR camera images are likely some combination of blowing snow and falling forebaffle snow.

B.5 Intersection with machine learning

This algorithm can be extended to machine learning quite naturally. It would be easy to manually create a training set including images with light and heavy snow contamination, low quality images, sun-up images, and snow-free images. The algorithm could be extended to make comparisons being new images and these training images for classification. At the time of developing the algo-

[5]Scansets consists of 106 azimuth slews at a given elevation step, taking approximately one hour. A phase is a set of eight to ten scansets, covering the elevation range of the patch. A schedule consists of the ten phases, covering the full survey.

[6]ASU – arbitrary snow units.

rithm, I had not heard the term “machine learning” but future incarnations of the snow-finding code will employ aspects of it.

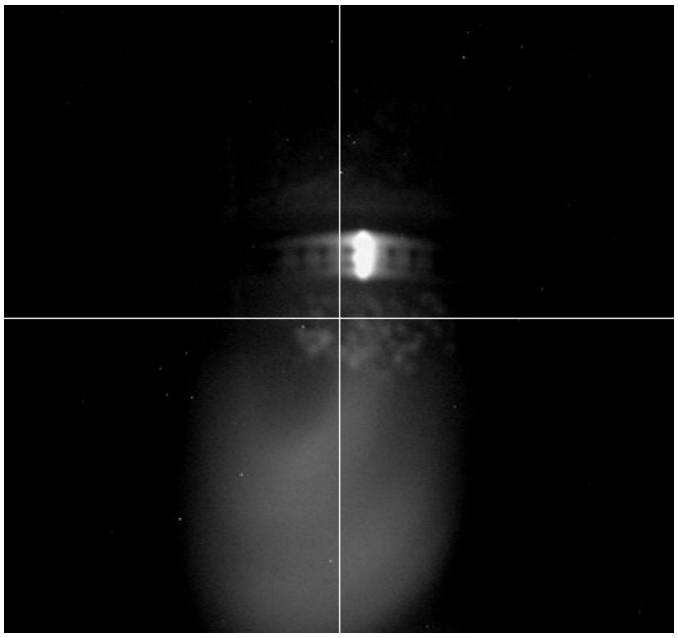

(a) Light snow

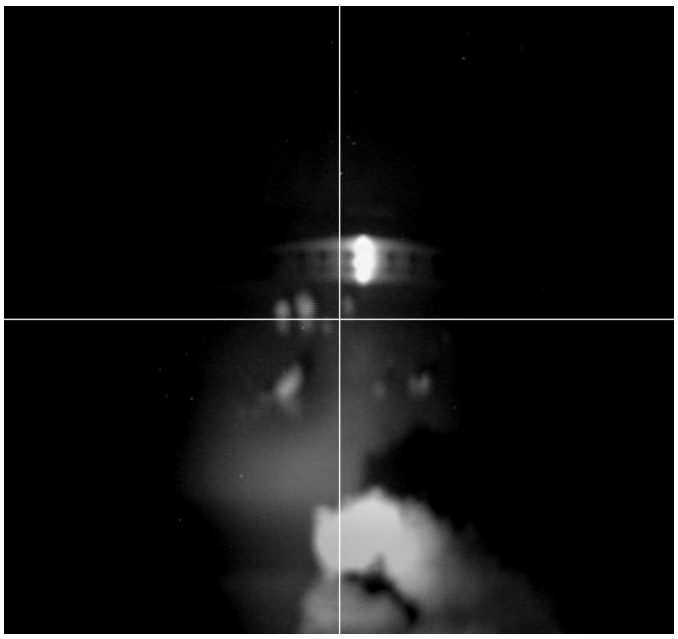

(b) Heavy snow

Figure B.3: Lower Forebaffle (LFB) IR camera pictures showing a light dusting of snow (top) and larger clumps of snow (bottom). These images register as 2500 ASU and 6900 ASU, respectively, from the snow finding algorithm.

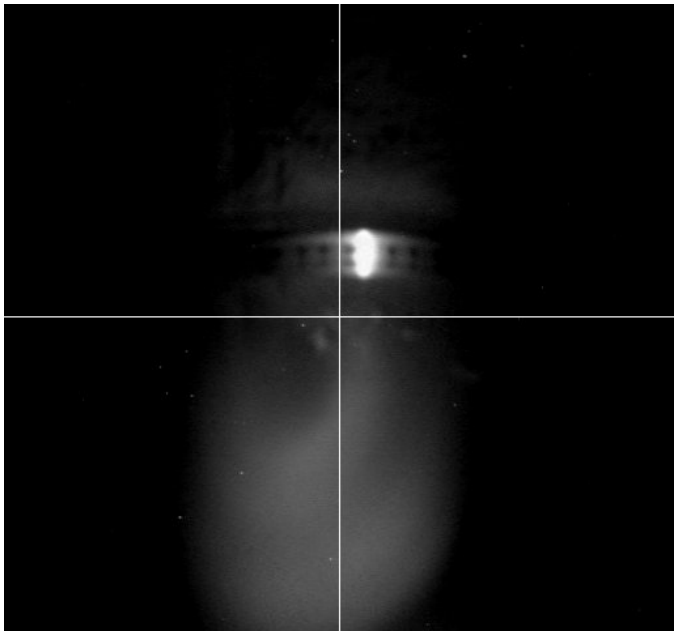

(a) Light snow

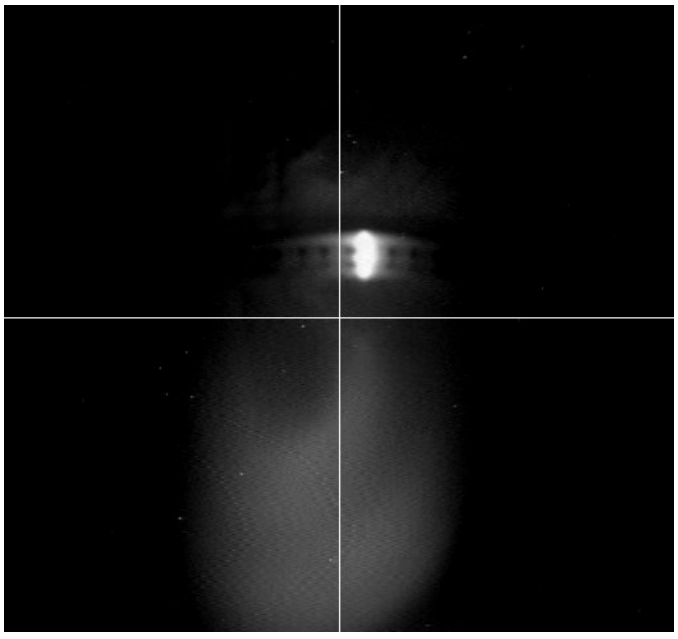

(b) Low quality

Figure B.4: Lower Forebaffle (LFB) IR camera pictures demonstrating the limitations of the snow finding algorithm. Both images register as snow and have similar magnitudes in ASU, however it is clear that there is no snow in the top image. This false positive is due to intermittent image quality issues with the camera and has a very different phenomenology than real snow over time.

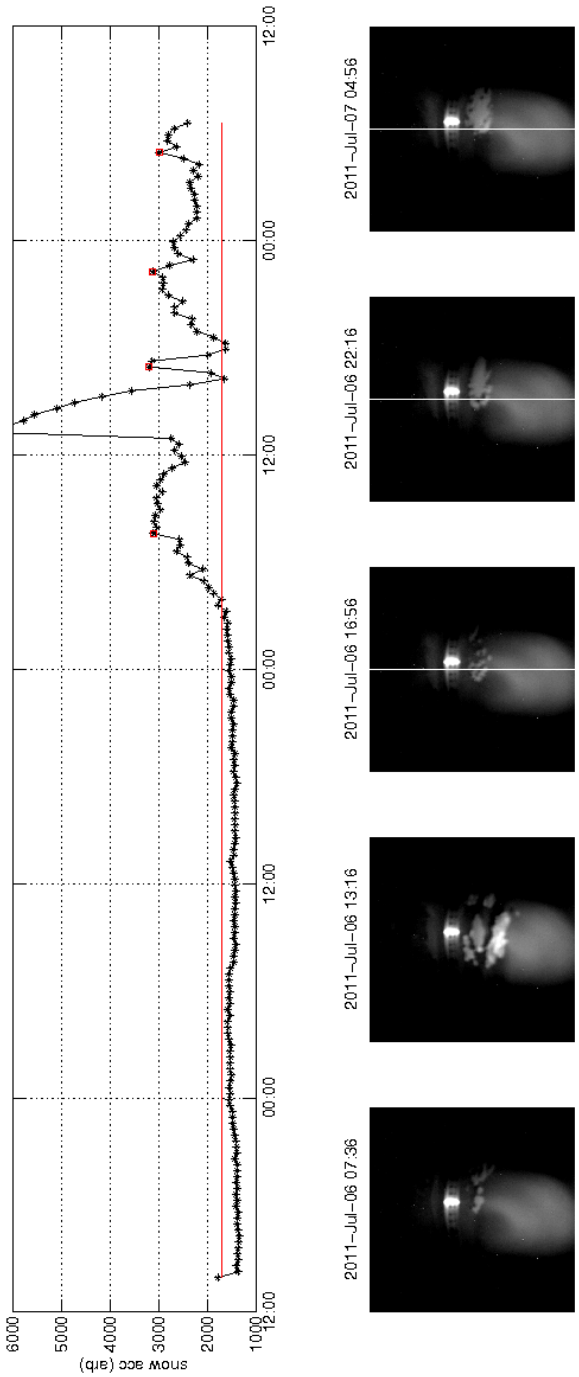

Figure B.5: A sample algorithm HTML display page.

Bibliography

[1] P. A. R. Ade, N. Aghanim, C. Armitage-Caplan, M. Arnaud, M. Ashdown, F. Atrio-Barandela, J. Aumont, C. Baccigalupi, A. J. Banday, R. B. Barreiro, J. G. Bartlett, E. Battaner, K. Benabed, A. Benot, A. Benoit-Lvy, J. Bernard, M. Bersanelli, P. Bielewicz, J. Bobin, J. J. Bock, A. Bonaldi, J. R. Bond, J. Borrill, F. R. Bouchet, M. Bridges, M. Bucher, C. Burigana, R. C. Butler, E. Calabrese, B. Cappellini, J. Cardoso, A. Catalano, A. Challinor, A. Chamballu, R. Chary, X. Chen, L. Chiang, H. C. Chiang, P. R. Christensen, S. Church, D. L. Clements, S. Colombi, L. P. L. Colombo, F. Couchot, A. Coulais, B. P. Crill, A. Curto, F. Cuttaia, L. Danese, R. D. Davies, R. J. Davis, P. de Bernardis, A. de Rosa, G. de Zotti, J. Delabrouille, J. Delouis, F. Dsert, C. Dickinson, J. M. Diego, K. Dolag, H. Dole, S. Donzelli, O. Dor, M. Douspis, J. Dunkley, X. Dupac, G. Efstathiou, F. Elsner, T. A. Enlin, H. K. Eriksen, F. Finelli, O. Forni, M. Frailis, A. A. Fraisse, E. Franceschi, T. C. Gaier, S. Galeotta, S. Galli, K. Ganga, M. Giard, G. Giardino, Y. Giraud-Hraud, E. Gjerlw, J. Gonzlez-Nuevo, K. M. Grski, S. Gratton, A. Gregorio, A. Gruppuso, J. E. Gudmundsson, J. Haissinski, J. Hamann, F. K. Hansen, D. Hanson, D. Harrison, S. Henrot-Versill, C. Hernndez-Monteagudo, D. Herranz, S. R. Hildebrandt, E. Hivon, M. Hobson, W. A. Holmes, A. Hornstrup, Z. Hou, W. Hovest, K. M. Huffenberger, T. R. Jaffe, A. H. Jaffe, J. Jewell, W. C. Jones, M. Juvela, E. Keihnen, R. Keskitalo, T. S. Kisner, R. Kneissl, J. Knoche, L. Knox, M. Kunz, H. Kurki-Suonio, G. Lagache, A. Lhteenmki, J. Lamarre, A. Lasenby, M. Lattanzi, R. J. Laureijs, C. R. Lawrence, S. Leach, J. P. Leahy, R. Leonardi, J. Len-Tavares, J. Lesgourgues, A. Lewis, M. Liguori, P. B. Lilje, M. Linden-Vrnle, M. Lpez-Caniego, P. M. Lubin, J. F. Macas-Prez, B. Maffei, D. Maino, N. Mandolesi, M. Maris, D. J. Marshall, P. G. Martin, E. Martnez-Gonzlez, S. Masi, S. Matarrese, F. Matthai, P. Mazzotta, P. R. Meinhold, A. Melchiorri, J. Melin, L. Mendes, E. Menegoni, A. Mennella, M. Migliaccio, M. Millea, S. Mitra, M. Miville-Deschnes, A. Moneti, L. Montier, G. Morgante, D. Mortlock, A. Moss, D. Munshi, P. Naselsky, F. Nati, P. Natoli, C. B. Netterfield, H. U. Nrgaard-Nielsen, F. Noviello, D. Novikov, I. Novikov, I. J. O'Dwyer, S. Osborne, C. A. Oxborrow, F. Paci, L. Pagano, F. Pajot, D. Paoletti, B. Partridge, F. Pasian, G. Patanchon, D. Pearson, T. J. Pearson, H. V. Peiris, O. Perdereau, L. Perotto, F. Perrotta, V. Pettorino,

F. Piacentini, M. Piat, E. Pierpaoli, D. Pietrobon, S. Plaszczynski, P. Platania, E. Pointecouteau, G. Polenta, N. Ponthieu, L. Popa, T. Poutanen, G. W. Pratt, G. Przeau, S. Prunet, J. Puget, J. P. Rachen, W. T. Reach, R. Rebolo, M. Reinecke, M. Remazeilles, C. Renault, S. Ricciardi, T. Riller, I. Ristorcelli, G. Rocha, C. Rosset, G. Roudier, M. Rowan-Robinson, J. A. Rubio-Martn, B. Rusholme, M. Sandri, D. Santos, M. Savelainen, G. Savini, D. Scott, M. D. Seiffert, E. P. S. Shellard, L. D. Spencer, J. Starck, V. Stolyarov, R. Stompor, R. Sudiwala, R. Sunyaev, F. Sureau, D. Sutton, A. Suur-Uski, J. Sygnet, J. A. Tauber, D. Tavagnacco, L. Terenzi, L. Toffolatti, M. Tomasi, M. Tristram, M. Tucci, J. Tuovinen, M. Trler, G. Umana, L. Valenziano, J. Valiviita, B. V. Tent, P. Vielva, F. Villa, N. Vittorio, L. A. Wade, B. D. Wandelt, I. K. Wehus, M. White, S. D. M. White, A. Wilkinson, D. Yvon, A. Zacchei, and A. Zonca. Planck 2013 results. XVI. Cosmological parameters. 2013.

[2] R. W. Aikin. *Testing Inflationary Cosmology with the Bicep1 and Bicep2 Experiments*. PhD thesis, California Institute of Technology, 2013.

[3] S. Alexander and J. Martin. Birefringent gravitational waves and the consistency check of inflation. Phys. Rev. D, 71(6):063526–+, Mar. 2005.

[4] S. H. Alexander, M. E. Peskin, and M. M. Sheikh-Jabbari. Leptogenesis from Gravity Waves in Models of Inflation. *Physical Review Letters*, 96(8):081301–+, Feb. 2006.

[5] J. Aumont, L. Conversi, C. Thum, H. Wiesemeyer, E. Falgarone, J. F. Macias-Perez, F. Piacentini, E. Pointecouteau, N. Ponthieu, J. L. Puget, C. Rosset, J. A. Tauber, and M. Tristram. Measurement of the Crab nebula polarization at 90 GHz as a calibrator for CMB experiments. *ArXiv e-prints*, Dec. 2009.

[6] D. Barkats, R. Aikin, C. Bischoff, I. Buder, J. M. Kovac, M. Su, P. A. R. Ade, J. O. Battle, E. M. Bierman, J. J. Bock, H. C. Chiang, C. D. Dowell, L. Duband, J. Filippini, E. F. Hivon, W. L. Holzapfel, V. V. Hristov, W. C. Jones, J. P. Kaufman, B. G. Keating, C. L. Kuo, E. M. Leitch, P. V. Mason, T. Matsumura, H. T. Nguyen, N. Ponthieu, C. Pryke, S. Richter, C. Sheehy, S. S. Kernasovskiy, Y. D. Takahashi, J. E. Tolan, and K. W. Yoon. Degree-Scale CMB Polarization Measurements from Three Years of BICEP1 Data. Oct. 2013.

[7] D. Baumann. TASI Lectures on Inflation. *ArXiv e-prints*, July 2009.

[8] C. L. Bennett, D. Larson, J. L. Weiland, N. Jarosik, G. Hinshaw, N. Odegard, K. M. Smith, R. S. Hill, B. Gold, M. Halpern, E. Komatsu, M. R. Nolta, L. Page, D. N. Spergel, E. Wollack, J. Dunkley, A. Kogut, M. Limon, S. S. Meyer, G. S. Tucker, and E. L. Wright. Nine-year Wilkinson Microwave Anisotropy Probe (WMAP) Observations: Final Maps and Results. ApJS, 208:20, Oct. 2013.

[9] BICEP2 Collaboration, P. A. R. Ade, R. W. Aikin, M. Amiri, D. Barkats, S. J. Benton, C. A. Bischoff, J. J. Bock, J. A. Brevik, I. Buder, E. Bullock, G. Davis, C. D. Dowell, L. Duband, J. P. Filippini, S. Fliescher, S. R. Golwala, M. Halpern, M. Hasselfield, S. R. Hildebrandt, G. C. Hilton, V. V. Hristov, K. D. Irwin, K. S. Karkare, J. P. Kaufman, B. G. Keating, S. A. Kernasovskiy, J. M. Kovac, C. L. Kuo, E. M. Leitch, N. Llombart, M. Lueker, C. B. Netterfield, H. T. Nguyen, R. O'Brient, R. W. Ogburn, IV, A. Orlando, C. Pryke, C. D. Reintsema, S. Richter, R. Schwarz, C. D. Sheehy, Z. K. Staniszewski, K. Story, R. V. Sudiwala, G. P. Teply, J. E. Tolan, A. D. Turner, A. G. Vieregg, P. Wilson, C. L. Wong, and K. W. Yoon. BICEP2 II: Experiment and Three-Year Data Set. *ArXiv e-prints*, Mar. 2014.

[10] BICEP2 Collaboration, P. A. R. Ade, R. W. Aikin, D. Barkats, S. J. Benton, C. A. Bischoff, J. J. Bock, J. A. Brevik, I. Buder, E. Bullock, C. D. Dowell, L. Duband, J. P. Filippini, S. Fliescher, S. R. Golwala, M. Halpern, M. Hasselfield, S. R. Hildebrandt, G. C. Hilton, V. V. Hristov, K. D. Irwin, K. S. Karkare, J. P. Kaufman, B. G. Keating, S. A. Kernasovskiy, J. M. Kovac, C. L. Kuo, E. M. Leitch, M. Lueker, P. Mason, C. B. Netterfield, H. T. Nguyen, R. O'Brient, R. W. Ogburn, IV, A. Orlando, C. Pryke, C. D. Reintsema, S. Richter, R. Schwarz, C. D. Sheehy, Z. K. Staniszewski, R. V. Sudiwala, G. P. Teply, J. E. Tolan, A. D. Turner, A. G. Vieregg, C. L. Wong, and K. W. Yoon. BICEP2 I: Detection Of B-mode Polarization at Degree Angular Scales. *ArXiv e-prints*, Mar. 2014.

[11] Bicep2 Collaboration III. Bicep2 systematics paper. *In prep.*, 2014.

[12] E. M. Bierman, T. Matsumura, C. D. Dowell, B. G. Keating, P. Ade, D. Barkats, D. Barron, J. O. Battle, J. J. Bock, H. C. Chiang, T. L. Culverhouse, L. Duband, E. F. Hivon, W. L. Holzapfel, V. V. Hristov, J. P. Kaufman, J. M. Kovac, C. L. Kuo, A. E. Lange, E. M. Leitch, P. V. Mason, N. J. Miller, H. T. Nguyen, C. Pryke, S. Richter, G. M. Rocha, C. Sheehy, Y. D. Takahashi, and K. W. Yoon. A Millimeter-wave Galactic Plane Survey with the BICEP Polarimeter. ApJ, 741:81, Nov. 2011.

[13] C. Bischoff, A. Brizius, I. Buder, Y. Chinone, K. Cleary, R. N. Dumoulin, A. Kusaka, R. Monsalve, S. K. Næss, L. B. Newburgh, G. Nixon, R. Reeves, K. M. Smith, K. Vanderlinde, I. K. Wehus, M. Bogdan, R. Bustos, S. E. Church, R. Davis, C. Dickinson, H. K. Eriksen, T. Gaier, J. O. Gundersen, M. Hasegawa, M. Hazumi, C. Holler, K. M. Huffenberger, W. A. Imbriale, K. Ishidoshiro, M. E. Jones, P. Kangaslahti, D. J. Kapner, C. R. Lawrence, E. M. Leitch, M. Limon, J. J. McMahon, A. D. Miller, M. Nagai, H. Nguyen, T. J. Pearson, L. Piccirillo, S. J. E. Radford, A. C. S. Readhead, J. L. Richards, D. Samtleben, M. Seiffert, M. C. Shepherd, S. T. Staggs, O. Tajima, K. L. Thompson, R. Williamson, B. Winstein, E. J. Wollack, and J. T. L. Zwart. The Q/U Imaging ExperimenT Instrument. ApJ, 768:9, May 2013.

[14] S. M. Carroll. Quintessence and the Rest of the World: Suppressing Long-Range Interactions. *Physical Review Letters*, 81:3067–3070, Oct. 1998.

[15] S. M. Carroll and G. B. Field. Is There Evidence for Cosmic Anisotropy in the Polarization of Distant Radio Sources? *Physical Review Letters*, 79:2394–2397, Sept. 1997.

[16] S. M. Carroll, G. B. Field, and R. Jackiw. Limits on a Lorentz- and parity-violating modification of electrodynamics. Phys. Rev. D, 41:1231–1240, Feb. 1990.

[17] R. A. Chamberlin, A. P. Lane, and A. A. Stark. The 492 ghz atmospheric opacity at the geographic south pole. *The Astrophysical Journal*, 476(1):428, 1997.

[18] H. C. Chiang, P. A. R. Ade, D. Barkats, J. O. Battle, E. M. Bierman, J. J. Bock, C. D. Dowell, L. Duband, E. F. Hivon, W. L. Holzapfel, V. V. Hristov, W. C. Jones, B. G. Keating, J. M. Kovac, C. L. Kuo, A. E. Lange, E. M. Leitch, P. V. Mason, T. Matsumura, H. T. Nguyen, N. Ponthieu, C. Pryke, S. Richter, G. Rocha, C. Sheehy, Y. D. Takahashi, J. E. Tolan, and K. W. Yoon. Measurement of Cosmic Microwave Background Polarization Power Spectra from Two Years of BICEP Data. ApJ, 711:1123–1140, Mar. 2010.

[19] C. R. Contaldi, F. Dowker, and L. Philpott. FAST TRACK COMMUNICATION: Polarization diffusion from spacetime uncertainty. *Classical and Quantum Gravity*, 27(17):172001–+, Sept. 2010.

[20] E. J. Copeland, E. W. Kolb, A. R. Liddle, and J. E. Lidsey. Observing the inflation potential. *Physical Review Letters*, 71:219–222, July 1993.

[21] S. De, L. Pogosian, and T. Vachaspati. CMB Faraday rotation as seen through the Milky Way. Phys. Rev. D, 88(6):063527, May 2013.

[22] P. A. J. de Korte, J. Beyer, S. Deiker, G. C. Hilton, K. D. Irwin, M. Macintosh, S. W. Nam, C. D. Reintsema, L. R. Vale, and M. E. Huber. Time-division superconducting quantum interference device multiplexer for transition-edge sensors. *Review of Scientific Instruments*, 74:3807–3815, Aug. 2003.

[23] J. Delabrouille, M. Betoule, J.-B. Melin, M.-A. Miville-Deschênes, J. Gonzalez-Nuevo, M. Le Jeune, G. Castex, G. de Zotti, S. Basak, M. Ashdown, J. Aumont, C. Baccigalupi, A. J. Banday, J.-P. Bernard, F. R. Bouchet, D. L. Clements, A. da Silva, C. Dickinson, F. Dodu, K. Dolag, F. Elsner, L. Fauvet, G. Faÿ, G. Giardino, S. Leach, J. Lesgourgues, M. Liguori, J. F. Macías-Pérez, M. Massardi, S. Matarrese, P. Mazzotta, L. Montier, S. Mottet, R. Paladini, B. Partridge, R. Piffaretti, G. Prezeau, S. Prunet, S. Ricciardi, M. Roman, B. Schaefer, and L. Toffolatti. The pre-launch Planck Sky Model:

a model of sky emission at submillimetre to centimetre wavelengths. A&A, 553:A96, May 2013.

[24] S. di Serego Alighieri. Cosmological Birefringence: an Astrophysical test of Fundamental Physics. Joint European and National Astronomy Meeting, Nov. 2010.

[25] S. di Serego Alighieri, F. Finelli, and M. Galaverni. Limits on Cosmological Birefringence from the Ultraviolet Polarization of Distant Radio Galaxies. ApJ, 715:33–38, May 2010.

[26] S. Dodelson. *Modern Cosmology*. Academic Press. Academic Press, 2003.

[27] L. Duband and B. Collaudin. Sorption coolers development at cea-sbt. *Cryogenics*, 39(8):659–663, 1999.

[28] J. R. Eimer, C. L. Bennett, D. T. Chuss, T. Marriage, E. J. Wollack, and L. Zeng. The cosmology large angular scale surveyor (CLASS): 40 GHz optical design. In *Society of Photo-Optical Instrumentation Engineers (SPIE) Conference Series*, volume 8452 of *Society of Photo-Optical Instrumentation Engineers (SPIE) Conference Series*, Sept. 2012.

[29] D. J. Eisenstein and E. F. Bunn. Appropriate Null Hypothesis for Cosmological Birefringence. *Physical Review Letters*, 79:1957, Sept. 1997.

[30] P. C. Farese, G. Dall'Oglio, J. O. Gundersen, B. G. Keating, S. Klawikowski, L. Knox, A. Levy, P. M. Lubin, C. W. O'Dell, A. Peel, L. Piccirillo, J. Ruhl, and P. T. Timbie. COMPASS: An Upper Limit on Cosmic Microwave Background Polarization at an Angular Scale of 20'. ApJ, 610:625–634, Aug. 2004.

[31] D. P. Finkbeiner, M. Davis, and D. J. Schlegel. Extrapolation of Galactic Dust Emission at 100 Microns to Cosmic Microwave Background Radiation Frequencies Using FIRAS. ApJ, 524:867–886, Oct. 1999.

[32] E. M. George, P. Ade, K. A. Aird, J. E. Austermann, J. A. Beall, D. Becker, A. Bender, B. A. Benson, L. E. Bleem, J. Britton, J. E. Carlstrom, C. L. Chang, H. C. Chiang, H.-M. Cho, T. M. Crawford, A. T. Crites, A. Datesman, T. de Haan, M. A. Dobbs, W. Everett, A. Ewall-Wice, N. W. Halverson, N. Harrington, J. W. Henning, G. C. Hilton, W. L. Holzapfel, S. Hoover, N. Huang, J. Hubmayr, K. D. Irwin, M. Karfunkle, R. Keisler, J. Kennedy, A. T. Lee, E. Leitch, D. Li, M. Lueker, D. P. Marrone, J. J. McMahon, J. Mehl, S. S. Meyer, J. Montgomery, T. E. Montroy, J. Nagy, T. Natoli, J. P. Nibarger, M. D. Niemack, V. Novosad, S. Padin, C. Pryke, C. L. Reichardt, J. E. Ruhl, B. R. Saliwanchik, J. T. Sayre, K. K. Schaffer, E. Shirokoff, K. Story, C. Tucker, K. Vanderlinde, J. D. Vieira, G. Wang, R. Williamson,

V. Yefremenko, K. W. Yoon, and E. Young. Performance and on-sky optical characterization of the SPTpol instrument. In *Society of Photo-Optical Instrumentation Engineers (SPIE) Conference Series*, volume 8452 of *Society of Photo-Optical Instrumentation Engineers (SPIE) Conference Series*, Sept. 2012.

[33] V. Gluscevic and M. Kamionkowski. Testing parity-violating mechanisms with cosmic microwave background experiments. Phys. Rev. D, 81(12):123529–+, June 2010.

[34] V. Gluscevic, M. Kamionkowski, and A. Cooray. Derotation of the cosmic microwave background polarization: Full-sky formalism. Phys. Rev. D, 80(2):023510–+, July 2009.

[35] G. Gubitosi and F. Paci. Constraints on cosmological birefringence energy dependence from CMB polarization data. Nov. 2012.

[36] S. Hamimeche and A. Lewis. Likelihood analysis of CMB temperature and polarization power spectra. Phys. Rev. D, 77(10):103013, May 2008.

[37] J. J. Hester. The crab nebula: An astrophysical chimera. *Annual Review of Astronomy and Astrophysics*, 46(1):127–155, 2008.

[38] A. Heurtel and M. Piat. 0.1 K cooler / Ho_xY_{1-x} FPU struts: Product assurance specifications. Planck HFI internal note, Apr. 2000.

[39] W. C. Jones, T. E. Montroy, B. P. Crill, C. R. Contaldi, T. S. Kisner, A. E. Lange, C. J. MacTavish, C. B. Netterfield, and J. E. Ruhl. Instrumental and analytic methods for bolometric polarimetry. A&A, 470:771–785, Aug. 2007.

[40] M. Kamionkowski. Nonuniform cosmological birefringence and active galactic nuclei. Phys. Rev. D, 82(4):047302, Aug. 2010.

[41] M. Kamionkowski, A. Kosowsky, and A. Stebbins. Statistics of cosmic microwave background polarization. Phys. Rev. D, 55:7368–7388, June 1997.

[42] J. P. Kaufman, N. J. Miller, M. Shimon, D. Barkats, C. Bischoff, I. Buder, B. G. Keating, J. M. Kovac, P. A. R. Ade, R. Aikin, J. O. Battle, E. M. Bierman, J. J. Bock, H. C. Chiang, C. D. Dowell, L. Duband, J. Filippini, E. F. Hivon, W. L. Holzapfel, V. V. Hristov, W. C. Jones, S. S. Kernasovskiy, C. L. Kuo, E. M. Leitch, P. V. Mason, T. Matsumura, H. T. Nguyen, N. Ponthieu, C. Pryke, S. Richter, G. Rocha, C. Sheehy, M. Su, Y. D. Takahashi, J. E. Tolan, and K. W. Yoon. Self-calibration of BICEP1 three-year data and constraints on astrophysical polarization rotation. Phys. Rev. D, 89(6):062006, Mar. 2014.

[43] B. G. Keating, P. A. Ade, J. J. Bock, E. Hivon, W. L. Hozapfel, A. E. Lange, H. Nguyen, and K. W. Yoon. BICEP: A Large Angular Scale CMB Polarimeter. 4843, 2003.

[44] B. G. Keating, M. Shimon, and A. P. S. Yadav. Self-calibration of Cosmic Microwave Background Polarization Experiments. ApJ, 762:L23, Jan. 2013.

[45] W. H. Kinney, E. W. Kolb, A. Melchiorri, and A. Riotto. Latest inflation model constraints from cosmic microwave background measurements: Addendum. Phys. Rev. D, 78(8):087302, Oct. 2008.

[46] L. Knox. Cosmic microwave background anisotropy window functions revisited. Phys. Rev. D, 60(10):103516, Nov. 1999.

[47] E. Komatsu, K. M. Smith, J. Dunkley, C. L. Bennett, B. Gold, G. Hinshaw, N. Jarosik, D. Larson, M. R. Nolta, L. Page, D. N. Spergel, M. Halpern, R. S. Hill, A. Kogut, M. Limon, S. S. Meyer, N. Odegard, G. S. Tucker, J. L. Weiland, E. Wollack, and E. L. Wright. Seven-year Wilkinson Microwave Anisotropy Probe (WMAP) Observations: Cosmological Interpretation. ApJS, 192:18, Feb. 2011.

[48] J. M. Kovac, E. M. Leitch, C. Pryke, J. E. Carlstrom, N. W. Halverson, and W. L. Holzapfel. Detection of polarization in the cosmic microwave background using DASI. Nature, 420:772–787, Dec. 2002.

[49] L. M. Krauss, S. Dodelson, and S. Meyer. Primordial Gravitational Waves and Cosmology. *Science*, 328:989–, May 2010.

[50] A. Lue, L. Wang, and M. Kamionkowski. Cosmological Signature of New Parity-Violating Interactions. *Physical Review Letters*, 83:1506–1509, Aug. 1999.

[51] M. Massardi, R. D. Ekers, T. Murphy, E. Mahony, P. J. Hancock, R. Chhetri, G. de Zotti, E. M. Sadler, S. Burke-Spolaor, M. Calabretta, P. G. Edwards, J. A. Ekers, C. A. Jackson, M. J. Kesteven, K. Newton-McGee, C. Phillips, R. Ricci, P. Roberts, R. J. Sault, L. Staveley-Smith, R. Subrahmanyan, M. A. Walker, and W. E. Wilson. The Australia Telescope 20 GHz (AT20G) Survey: analysis of the extragalactic source sample. MNRAS, 412:318–330, Mar. 2011.

[52] N. J. Miller, M. Shimon, and B. G. Keating. CMB polarization systematics due to beam asymmetry: Impact on cosmological birefringence. Phys. Rev. D, 79(10):103002–+, May 2009.

[53] S. Moyerman, E. Bierman, P. A. R. Ade, R. Aiken, D. Barkats, C. Bischoff, J. J. Bock, H. C. Chiang, C. D. Dowell, L. Duband, E. F. Hivon, W. L. Holzapfel, V. V. Hristov, W. C. Jones, J. Kaufman, B. G. Keating, J. M.

Kovac, C. L. Kuo, E. M. Leitch, P. V. Mason, T. Matsumura, H. T. Nguyen, N. Ponthieu, C. Pryke, S. Richter, G. Rocha, C. Sheehy, Y. D. Takahashi, J. E. Tolan, E. Wollack, and K. W. Yoon. Scientific Verification of Faraday Rotation Modulators: Detection of Diffuse Polarized Galactic Emission. ApJ, 765:64, Mar. 2013.

[54] H. T. Nguyen, J. Kovac, P. Ade, R. Aikin, S. Benton, J. Bock, J. Brevik, J. Carlstrom, D. Dowell, L. Duband, S. Golwala, M. Halpern, M. Hasslefield, K. Irwin, W. Jones, J. Kaufman, B. Keating, C.-L. Kuo, A. Lange, T. Matsumura, B. Netterfield, C. Pryke, J. Ruhl, C. Sheehy, and R. Sudiwala. Bicep2/spud: searching for inflation with degree scale polarimetry from the south pole. *Proc. SPIE*, 7020:70201F–70201F–9, 2008.

[55] M. D. Niemack, P. A. R. Ade, J. Aguirre, F. Barrientos, J. A. Beall, J. R. Bond, J. Britton, H. M. Cho, S. Das, M. J. Devlin, S. Dicker, J. Dunkley, R. Dünner, J. W. Fowler, A. Hajian, M. Halpern, M. Hasselfield, G. C. Hilton, M. Hilton, J. Hubmayr, J. P. Hughes, L. Infante, K. D. Irwin, N. Jarosik, J. Klein, A. Kosowsky, T. A. Marriage, J. McMahon, F. Menanteau, K. Moodley, J. P. Nibarger, M. R. Nolta, L. A. Page, B. Partridge, E. D. Reese, J. Sievers, D. N. Spergel, S. T. Staggs, R. Thornton, C. Tucker, E. Wollack, and K. W. Yoon. ACTPol: a polarization-sensitive receiver for the Atacama Cosmology Telescope. In *Society of Photo-Optical Instrumentation Engineers (SPIE) Conference Series*, volume 7741 of *Society of Photo-Optical Instrumentation Engineers (SPIE) Conference Series*, July 2010.

[56] B. Nodland and J. P. Ralston. Indication of Anisotropy in Electromagnetic Propagation over Cosmological Distances. *Physical Review Letters*, 78:3043–3046, Apr. 1997.

[57] D. T. O'Dea, C. N. Clark, C. R. Contaldi, and C. J. MacTavish. A model for polarized microwave foreground emission from interstellar dust. MNRAS, 419:1795–1803, Jan. 2012.

[58] L. Pagano, P. de Bernardis, G. de Troia, G. Gubitosi, S. Masi, A. Melchiorri, P. Natoli, F. Piacentini, and G. Polenta. CMB polarization systematics, cosmological birefringence, and the gravitational waves background. Phys. Rev. D, 80(4):043522, Aug. 2009.

[59] Planck Collaboration, P. A. R. Ade, N. Aghanim, C. Armitage-Caplan, M. Arnaud, M. Ashdown, F. Atrio-Barandela, J. Aumont, C. Baccigalupi, A. J. Banday, and et al. Planck 2013 results. I. Overview of products and scientific results. *ArXiv e-prints*, Mar. 2013.

[60] Planck Collaboration, P. A. R. Ade, N. Aghanim, C. Armitage-Caplan, M. Arnaud, M. Ashdown, F. Atrio-Barandela, J. Aumont, C. Baccigalupi, A. J.

Banday, and et al. Planck 2013 results. I. Overview of products and scientific results. *ArXiv e-prints*, Mar. 2013.

[61] Planck HFI Core Team, P. A. R. Ade, N. Aghanim, R. Ansari, M. Arnaud, M. Ashdown, J. Aumont, A. J. Banday, M. Bartelmann, J. G. Bartlett, E. Battaner, K. Benabed, A. Benoît, J.-P. Bernard, M. Bersanelli, J. J. Bock, J. R. Bond, J. Borrill, F. R. Bouchet, F. Boulanger, T. Bradshaw, M. Bucher, J.-F. Cardoso, G. Castex, A. Catalano, A. Challinor, A. Chamballu, R.-R. Chary, X. Chen, C. Chiang, S. Church, D. L. Clements, J.-M. Colley, S. Colombi, F. Couchot, A. Coulais, C. Cressiot, B. P. Crill, M. Crook, P. de Bernardis, J. Delabrouille, J.-M. Delouis, F.-X. Désert, K. Dolag, H. Dole, O. Doré, M. Douspis, J. Dunkley, G. Efstathiou, C. Filliard, O. Forni, P. Fosalba, K. Ganga, M. Giard, D. Girard, Y. Giraud-Héraud, R. Gispert, K. M. Górski, S. Gratton, M. Griffin, G. Guyot, J. Haissinski, D. Harrison, G. Helou, S. Henrot-Versillé, C. Hernández-Monteagudo, S. R. Hildebrandt, R. Hills, E. Hivon, M. Hobson, W. A. Holmes, K. M. Huffenberger, A. H. Jaffe, W. C. Jones, J. Kaplan, R. Kneissl, L. Knox, M. Kunz, G. Lagache, J.-M. Lamarre, A. E. Lange, A. Lasenby, A. Lavabre, C. R. Lawrence, M. Le Jeune, C. Leroy, J. Lesgourgues, J. F. Macías-Pérez, C. J. MacTavish, B. Maffei, N. Mandolesi, R. Mann, F. Marleau, D. J. Marshall, S. Masi, T. Matsumura, I. McAuley, P. McGehee, J.-B. Melin, C. Mercier, S. Mitra, M.-A. Miville-Deschênes, A. Moneti, L. Montier, D. Mortlock, A. Murphy, F. Nati, C. B. Netterfield, H. U. Nørgaard-Nielsen, C. North, F. Noviello, D. Novikov, S. Osborne, F. Pajot, G. Patanchon, T. Peacocke, T. J. Pearson, O. Perdereau, L. Perotto, F. Piacentini, M. Piat, S. Plaszczynski, E. Pointecouteau, N. Ponthieu, G. Prézeau, S. Prunet, J.-L. Puget, W. T. Reach, M. Remazeilles, C. Renault, A. Riazuelo, I. Ristorcelli, G. Rocha, C. Rosset, G. Roudier, M. Rowan-Robinson, B. Rusholme, R. Saha, D. Santos, G. Savini, B. M. Schaefer, P. Shellard, L. Spencer, J.-L. Starck, V. Stolyarov, R. Stompor, R. Sudiwala, R. Sunyaev, D. Sutton, J.-F. Sygnet, J. A. Tauber, C. Thum, J.-P. Torre, F. Touze, M. Tristram, F. van Leeuwen, L. Vibert, D. Vibert, L. A. Wade, B. D. Wandelt, S. D. M. White, H. Wiesemeyer, A. Woodcraft, V. Yurchenko, D. Yvon, and A. Zacchei. Planck early results. VI. The High Frequency Instrument data processing. A&A, 536:A6, Dec. 2011.

[62] M. Runyan and W. Jones. Thermal conductivity of thermally-isolating polymeric and composite structural support materials between 0.3 and 4 K. *Cryogenics*, 48(9-10):448 – 454, 2008.

[63] U. Seljak. Measuring Polarization In Cosmic Microwave Background. ApJ, 482(1), June 1997.

[64] C. D. Sheehy, P. A. R. Ade, R. W. Aikin, M. Amiri, S. Benton, C. Bischoff, J. J. Bock, J. A. Bonetti, J. A. Brevik, B. Burger, C. D. Dowell, L. Duband,

J. P. Filippini, S. R. Golwala, M. Halpern, M. Hasselfield, G. Hilton, V. V. Hristov, K. Irwin, J. P. Kaufman, B. G. Keating, J. M. Kovac, C. L. Kuo, A. E. Lange, E. M. Leitch, M. Lueker, C. B. Netterfield, H. T. Nguyen, R. W. Ogburn, IV, A. Orlando, C. L. Pryke, C. Reintsema, S. Richter, J. E. Ruhl, M. C. Runyan, Z. Staniszewski, S. Stokes, R. Sudiwala, G. Teply, K. L. Thompson, J. E. Tolan, A. D. Turner, P. Wilson, and C. L. Wong. The Keck Array: a pulse tube cooled CMB polarimeter. *ArXiv e-prints*, Apr. 2011.

[65] M. Shimon, B. Keating, N. Ponthieu, and E. Hivon. Cmb polarization systematics due to beam asymmetry: Impact on inflationary science. Phys. Rev. D, 77(8):083003–+, Apr. 2008.

[66] K. M. Smith, C. Dvorkin, L. Boyle, N. Turok, M. Halpern, G. Hinshaw, and B. Gold. On quantifying and resolving the BICEP2/Planck tension over gravitational waves. *ArXiv e-prints*, Apr. 2014.

[67] O. Tajima, H. Nguyen, C. Bischoff, A. Brizius, I. Buder, and A. Kusaka. Novel Calibration System with Sparse Wires for CMB Polarization Receivers. *Journal of Low Temperature Physics*, 167:936–942, June 2012.

[68] Y. D. Takahashi, P. A. R. Ade, D. Barkats, J. O. Battle, E. M. Bierman, J. J. Bock, H. C. Chiang, C. D. Dowell, L. Duband, E. F. Hivon, W. L. Holzapfel, V. V. Hristov, W. C. Jones, B. G. Keating, J. M. Kovac, C. L. Kuo, A. E. Lange, E. M. Leitch, P. V. Mason, T. Matsumura, H. T. Nguyen, N. Ponthieu, C. Pryke, S. Richter, G. Rocha, and K. W. Yoon. Characterization of the BICEP Telescope for High-precision Cosmic Microwave Background Polarimetry. ApJ, 711:1141–1156, Mar. 2010.

[69] The POLARBEAR Collaboration, P. A. R. Ade, Y. Akiba, A. E. Anthony, K. Arnold, M. Atlas, D. Barron, D. Boettger, J. Borrill, S. Chapman, Y. Chinone, M. Dobbs, T. Elleflot, J. Errard, G. Fabbian, C. Feng, D. Flanigan, A. Gilbert, W. Grainger, N. W. Halverson, M. Hasegawa, K. Hattori, M. Hazumi, W. L. Holzapfel, Y. Hori, J. Howard, P. Hyland, Y. Inoue, G. C. Jaehnig, A. H. Jaffe, B. Keating, Z. Kermish, R. Keskitalo, T. Kisner, M. Le Jeune, A. T. Lee, E. M. Leitch, E. Linder, M. Lungu, F. Matsuda, T. Matsumura, X. Meng, N. J. Miller, H. Morii, S. Moyerman, M. J. Myers, M. Navaroli, H. Nishino, H. Paar, J. Peloton, D. Poletti, E. Quealy, G. Rebeiz, C. L. Reichardt, P. L. Richards, C. Ross, I. Schanning, D. E. Schenck, B. D. Sherwin, A. Shimizu, C. Shimmin, M. Shimon, P. Siritanasak, G. Smecher, H. Spieler, N. Stebor, B. Steinbach, R. Stompor, A. Suzuki, S. Takakura, T. Tomaru, B. Wilson, A. Yadav, and O. Zahn. A Measurement of the Cosmic Microwave Background B-Mode Polarization Power Spectrum at Sub-Degree Scales with POLARBEAR. *ArXiv e-prints*, Mar. 2014.

[70] T. Tomaru, M. Hazumi, A. T. Lee, P. Ade, K. Arnold, D. Barron, J. Borrill, S. Chapman, Y. Chinone, M. Dobbs, J. Errard, G. Fabbian, A. Ghribi, W. Grainger, N. Halverson, M. Hasegawa, K. Hattori, W. L. Holzapfel, Y. Inoue, S. Ishii, Y. Kaneko, B. Keating, Z. Kermish, N. Kimura, T. Kisner, W. Kranz, F. Matsuda, T. Matsumura, H. Morii, M. J. Myers, H. Nishino, T. Okamura, E. Quealy, C. L. Reichardt, P. L. Richards, D. Rosen, C. Ross, A. Shimizu, M. Sholl, P. Siritanasak, P. Smith, N. Stebor, R. Stompor, A. Suzuki, J.-i. Suzuki, S. Takada, K.-i. Tanaka, and O. Zahn. The polarbear-2 experiment. volume 8452, pages 84521H–84521H–10, 2012.

[71] J. F. C. Wardle, R. A. Perley, and M. H. Cohen. Observational Evidence against Birefringence over Cosmological Distances. *Physical Review Letters*, 79:1801–1804, Sept. 1997.

[72] A. Wootten and A. R. Thompson. The Atacama Large Millimeter/Submillimeter Array. *IEEE Proceedings*, 97:1463–1471, Aug. 2009.

[73] E. Y. S. Wu, P. Ade, J. Bock, M. Bowden, M. L. Brown, G. Cahill, P. G. Castro, S. Church, T. Culverhouse, R. B. Friedman, K. Ganga, W. K. Gear, S. Gupta, J. Hinderks, J. Kovac, A. E. Lange, E. Leitch, S. J. Melhuish, Y. Memari, J. A. Murphy, A. Orlando, L. Piccirillo, C. Pryke, N. Rajguru, B. Rusholme, R. Schwarz, C. O'Sullivan, A. N. Taylor, K. L. Thompson, A. H. Turner, and M. Zemcov. Parity Violation Constraints Using Cosmic Microwave Background Polarization Spectra from 2006 and 2007 Observations by the QUaD Polarimeter. *Physical Review Letters*, 102(16):161302–+, Apr. 2009.

[74] J.-Q. Xia. Cosmological CPT violation and CMB polarization measurements. J. Cosmology Astropart. Phys., 1:46, Jan. 2012.

[75] J.-Q. Xia, H. Li, and X. Zhang. Probing CPT violation with CMB polarization measurements. *Physics Letters B*, 687:129–132, Apr. 2010.

[76] A. P. S. Yadav, R. Biswas, M. Su, and M. Zaldarriaga. Constraining a spatially dependent rotation of the cosmic microwave background polarization. Phys. Rev. D, 79(12):123009, June 2009.

[77] A. P. S. Yadav, M. Shimon, and B. G. Keating. Revealing Cosmic Rotation. Phys. Rev. D, 86(8), July 2012.

[78] K. W. Yoon, P. A. R. Ade, D. Barkats, J. O. Battle, E. M. Bierman, J. J. Bock, J. A. Brevik, H. C. Chiang, A. Crites, C. D. Dowell, L. Duband, G. S. Griffin, E. F. Hivon, W. L. Holzapfel, V. V. Hristov, B. G. Keating, J. M. Kovac, C. L. Kuo, A. E. Lange, E. M. Leitch, P. V. Mason, H. T. Nguyen, N. Ponthieu, Y. D. Takahashi, T. Renbarger, L. C. Weintraub, and D. Woolsey. The

robinson gravitational wave background telescope (bicep): a bolometric large angular scale cmb polarimeter. *Proc. SPIE*, 6275:62751K–62751K–18, 2006.